# DETECTION AND LOCALIZATION OF DRONES IN MIMO CW RADAR

A THESIS SUBMITTED TO
THE GRADUATE SCHOOL OF NATURAL AND APPLIED SCIENCES
OF
MIDDLE EAST TECHNICAL UNIVERSITY

BY

AYHAN YAZICI

IN PARTIAL FULFILLMENT OF THE REQUIREMENTS
FOR
THE DEGREE OF DOCTOR OF PHILOSOPHY
IN
ELECTRICAL AND ELECTRONICS ENGINEERING

JANUARY 2023

Approval of the thesis:

**DETECTION AND LOCALIZATION OF DRONES IN MIMO CW RADAR**

submitted by **AYHAN YAZICI** in partial fulfillment of the requirements for the degree of **Doctor of Philosophy in Electrical and Electronics Engineering Department, Middle East Technical University** by,

Prof. Dr. Halil Kalıpçılar
Dean, Graduate School of **Natural and Applied Sciences** _____

Prof. Dr. İlkay Ulusoy
Head of Department, **Electrical and Electronics Engineering** _____

Prof. Dr. Buyurman Baykal
Supervisor, **Electrical and Electronics Engineering, METU** _____

**Examining Committee Members:**

Prof. Dr. Ali Özgür Yılmaz
Electrical and Electronics Engineering, METU _____

Prof. Dr. Buyurman Baykal
Electrical and Electronics Engineering, METU _____

Prof. Dr. Orhan Arıkan
Electrical and Electronics Engineering, İ.D. Bilkent University _____

Prof. Dr. Çağatay Candan
Electrical and Electronics Engineering, METU _____

Prof. Dr. Tolga Girici
Electrical and Electronics Engineering, TOBB ETÜ _____

Date:18.01.2023

**I hereby declare that all information in this document has been obtained and presented in accordance with academic rules and ethical conduct. I also declare that, as required by these rules and conduct, I have fully cited and referenced all material and results that are not original to this work.**

Name, Surname: AYHAN YAZICI

Signature :

# ABSTRACT

## DETECTION AND LOCALIZATION OF DRONES IN MIMO CW RADAR

YAZICI, AYHAN
Ph.D., Department of Electrical and Electronics Engineering
Supervisor: Prof. Dr. Buyurman Baykal

January 2023, 148 pages

Low radar cross section and capability to fly at low speeds make drones challenging targets for radar detection. In the presence of ground moving targets, the frequency spectrum is also crowded which makes the detection of the drones more difficult. Micro-Doppler effect is the main feature used to discriminate drone from other targets and clutter. Typically, discrimination is performed after the detection of all the targets. Especially in target dense environments, such as cities, typical approach requires high processing power in order detect and classify all of the targets. Coverage is also another problem of the typical monostatic radar based drone detection in cities. Coverage of monostatic radar is easily blocked by buildings. In order to cope with these problems distributed multi-input multi-output (MIMO) continuous wave (CW) radar using MIMO cyclic spectral density (CSD) analysis (MCSD) method is proposed in this thesis. MCSD method separates drones and other targets and clutter in cyclic frequency domain. In order to make system simple and low cost, a network of continuous wave radars is used and the localization is performed based on Doppler only localization approach. The simulations and experimental results show the proof of the concept. Performance and cost analysis of MCSD method is also analyzed in the thesis.

Keywords: Cyclostationary, deinterleaving, Doppler-only localization, drone detection, MIMO radar, radar

# ÖZ

## MIMO(ÇOKLU GİRİŞ ÇOKLU ÇIKIŞ) SÜREKLİ DALGA RADARINDA İNSANSIZ HAVA ARACI (İHA) SEZİMİ VE KONUMLANDIRMASI

YAZICI, AYHAN
Doktora, Elektrik ve Elektronik Mühendisliği Bölümü
Tez Yöneticisi: Prof. Dr. Buyurman Baykal

Ocak 2023 , 148 sayfa

Drone'ların sahip olduğu düşük radar kesit alanları onları radar tespiti açısından zorlayıcı hedefler yapar. Yerde hareket eden hedeflerin varlığında sıklık tayfında oluşan yoğunluk drone'ların tespiti daha da güçleştirir. Micro-Doppler etki drone'ların diğer hedeflerden ayırt edilmesinde kullanılan ana özniteliklerdendir. Tipik olarak drone'ların ayırt edilmesi hedef tespitinden sonra gerçekleştirilir. Şehir gibi hedef yoğun ortamlarda bu yaklaşım yüksek işlem gücü gerektirmektedir. Monostatic radar kapsama alanı şehir ortamlarında yaşanan bir diğer problemdir. Binalar tarafından monostatic radar kapsama alanı kısıtlanabilmektedir. Bu zorluklarla mücadele etmek için dağıtık çok girişli çok çıkışlı sürekli dalgalı radarda çok girişli çok çıkışlı çevrimsel tayf yoğunluk analizi yöntemi (MCSD) bu tezde sunulmuştur. MCSD yöntemi drone'lar ile diğer hedefleri çevrimsel sıklık ekseninde ayrılır. Önerilen sistemin basit ve ucuz olabilmesi için sürekli dalga radarında sadece Doppler bilgisi ile konum bulma yaklaşımı uygulanmıştır. Benzetimler ve deneysel sonuçlar önerilen yöntemin ispatını yapmaktadır. MCSD yönteminin performans ve maliyet analizleri tezde ayrıca sunulmuştur.

Anahtar Kelimeler: Çevrimsel durağan, ayrıştırıcı, sadece Doppler ile konumlandırma, drone tespiti, çok girişli çok çıkışlı radar, radar

to my family

## ACKNOWLEDGMENTS

First of all, I would like to thank my supervisor Prof. Dr. Buyurman Baykal for his guidance, support, advices and innovative ideas throughout my thesis. It is a big chance for me to work with him.

Besides my advisor, I would like to thank to the thesis monitoring committee members Prof. Dr. Orhan Arıkan and Prof. Dr. Ali Özgür Yılmaz for their insightful comments.

I would like to thank to my colleagues in ASELSAN and TÜBİTAK for their contributions.

I would like to thank to my parents for their love and support.

I would like to thank to my wife Aytül and my daughters Nil and Tuğçe for their love, encouragement, inspiration and understanding.

## TABLE OF CONTENTS

## LIST OF TABLES

TABLES

## LIST OF FIGURES

FIGURES

# CHAPTER 1

# INTRODUCTION

This thesis is prepared to propose a drone detection and localization method and system solution. In this chapter, problem definition and the motivation of the study is given. The main idea behind the proposed method and the contributions of this thesis are also covered in this chapter.

## 1.1 Motivation and Problem Definition

Drones are becoming part of our lives as a result of developments in recent years. Beside military purposes, they are being widely used for civilian purposes as well since they can be reached easily in the market and can be controlled without a detailed training. The ease of purchasing drones can lead to the use of drones in criminal cases in military or civilian domains. These facts make drone detection an important research topic.

There have been numerous approaches to drone detection in the literature, some of which are summarized below.

- Video and image drone detection: Examples of image and video detection based drone detection are explored in [14], [15] and [1] with experimental data and various backgrounds. Although promising studies in video drone detection are ongoing, there are some inherent disadvantages of video sensing compared to radio frequency sensing, such as strong dependence of video performance on weather conditions, day/night illumination levels, and sun blindness.

  In [14], [15], and [1] image and video processing is used to detect and classify

UAVs. The convolutional neural network approach is used in these studies. The experiments are performed in various backgrounds for different targets. In Figure 1.1 the training samples are shown, which are used in [1]. Birds are stated as the most confusing clutter when detecting UAVs with image and video processing [1].

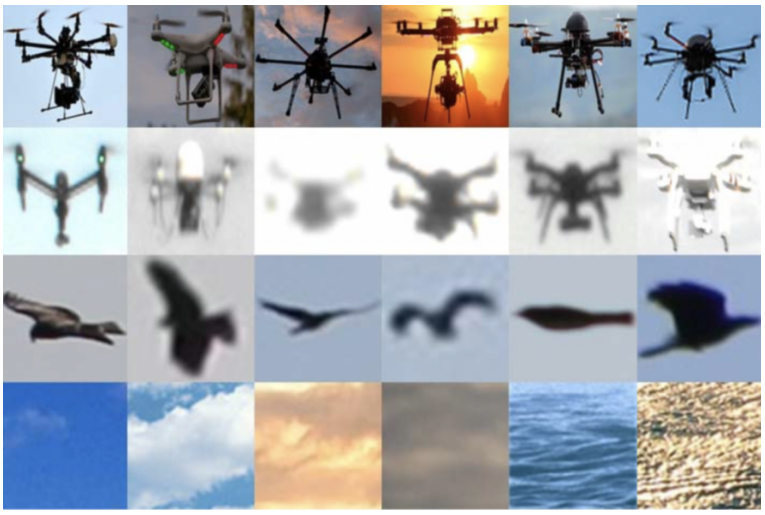

Figure 1.1: Training samples used in [1]

- Remote controller signal drone detection: In [2], communication signals between the UAV and the remote controller are used to detect UAVs. To differentiate the signals coming from the UAV and other sources, micro Doppler effects generated by the UAV on the signals are studied. The short-time Fourier transform and wavelet transform are used in the algorithm. The basic flow chart of the algorithm is shown in Figure 1.2.

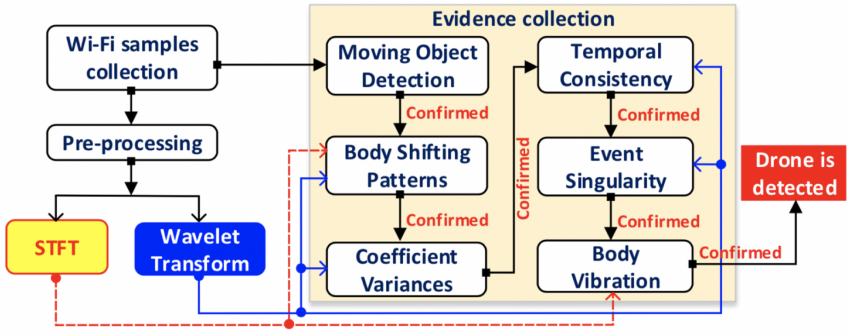


Figure 1.2: Algorithm flow chart of [2]

- Acoustic drone detection: In [16] drone detection is investigated in the acoustic domain. The detection and tracking of a model airplane is performed as a validation activity, which can only determine the direction of the target. So in order to locate a target many subsystems have to be deployed in the coverage region. Taking into account urban scenarios, the system will be subject to serious levels of acoustic noise, which can dramatically affect the performance of the system. A sample for the acoustic UAV detection study is in [16]. In this work, an acoustic array is used to detect and locate UAVs. Both calibration and beamforming is studied. The detection and tracking of a model airplane is performed as the validation activity of the proposed system.

- Radar drone detection: In addition to acoustic and video drone detection, radar drone detection is a method that has attracted a focus of attention in the literature. In addition, radar researchers investigate the extraction of features from radar echo signals for classification of the drones. In [3], a brief introduction to the staring radar concept is presented. The detection performance and minimum detectable velocity of staring radars and scanning radars are compared. Since lower minimum detectable velocity can be obtained with staring radars, UAV detection is presented as an advantageous scenario for staring radars. The ALARM staring radar's (used by British army) data is used in the study. ALARM is operating in the 4-6 GHz band with FMCW signal. It has 120 degree azimuth and 30 degree elevation coverage. This coverage value is obtained with a 6x3 antenna configuration and 18 receivers. In [3], the importance of long dwell time for detecting drones is especially stated.

  In [4], UAV detection and tracking are studied with a multistatic radar system. The radar system is an S-band pulse Doppler system. The experimental scenario is shown in Figure 1.4. The approach in [4] is based on the micro-Doppler components in the radar echo signal. The number of Doppler components is counted and a decision about drone presence is made. Each bistatic radar in [4] calculates the range information. This range information is used to calculate the drone's location.

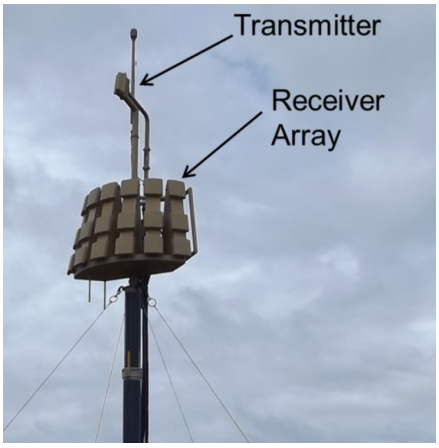


Figure 1.3: Alarm system [3]

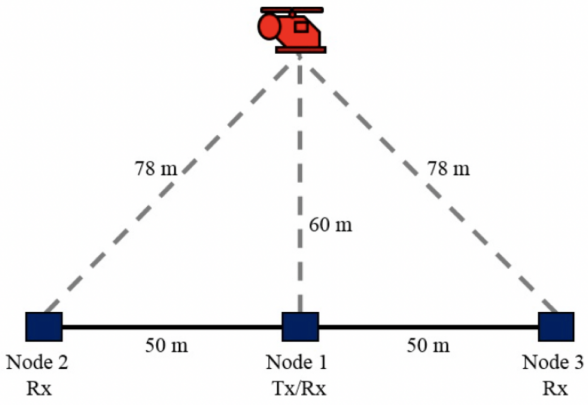


Figure 1.4: Scenario in [4]

Passive radars are very popular among academic research, as passive radars are inexpensive and simple. There are also many studies on UAV detection with passive radars. In [5] and [17] GSM signal based passive radars are used for UAV detection. In [5] the receive antenna is an 8-element circular array antenna. The experiment is carried out in an open field. The experimental scenario is shown in Figure 1.5.

The DAB ( [18] ) and DVB ( [6] ) signals are also used as signal of opportunity in passive radar systems to detect UAVs. In [6], the block diagram of the UAV detection system is shown in Figure 1.6.

Micro-Doppler characteristics of the radar echo signal from drones are features

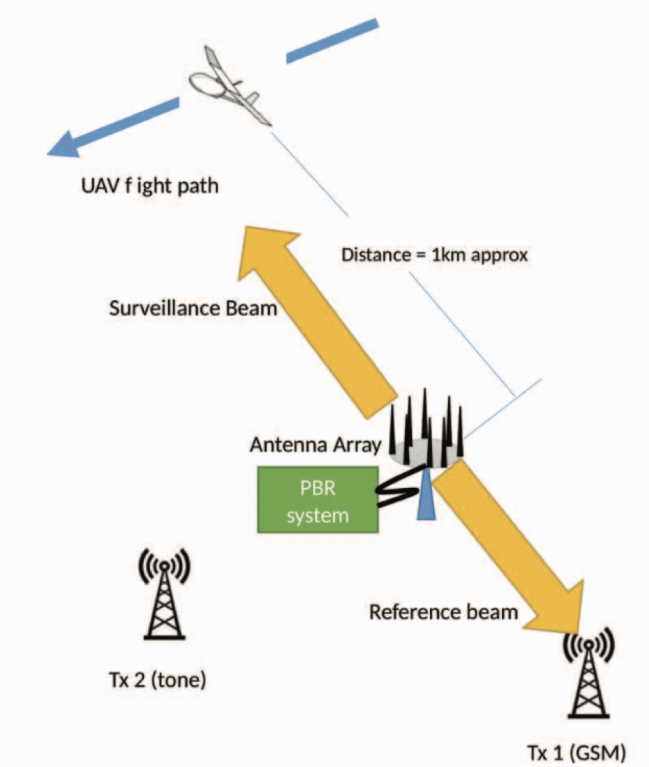


Figure 1.5: Experimental scenario in [5]

that are frequently used in classification. In [4], classification in short-time Fourier transform domain using micro-Doppler characteristics is proposed to classify drones in a multistatic radar system. In [7] and [19] the micro-Doppler parameters are estimated using cyclostationary analysis, in particular, computing the cyclic spectral density and then extracting the related parameters.

The typical approach of the above mentioned studies is classifying detected targets as drone or not. Classification is performed after detection for all detected targets. Target dense environments, such as cities, challenge this approach. Another problem facing drone sensing systems is the limitation of coverage caused by buildings. Keeping in mind these difficulties, in RF drone detection, the following items are considered to be the target requirements of this study.

- The system shall be cheap compared to conventional radar system alternatives,
- The system shall suppress clutter, especially urban area clutter,

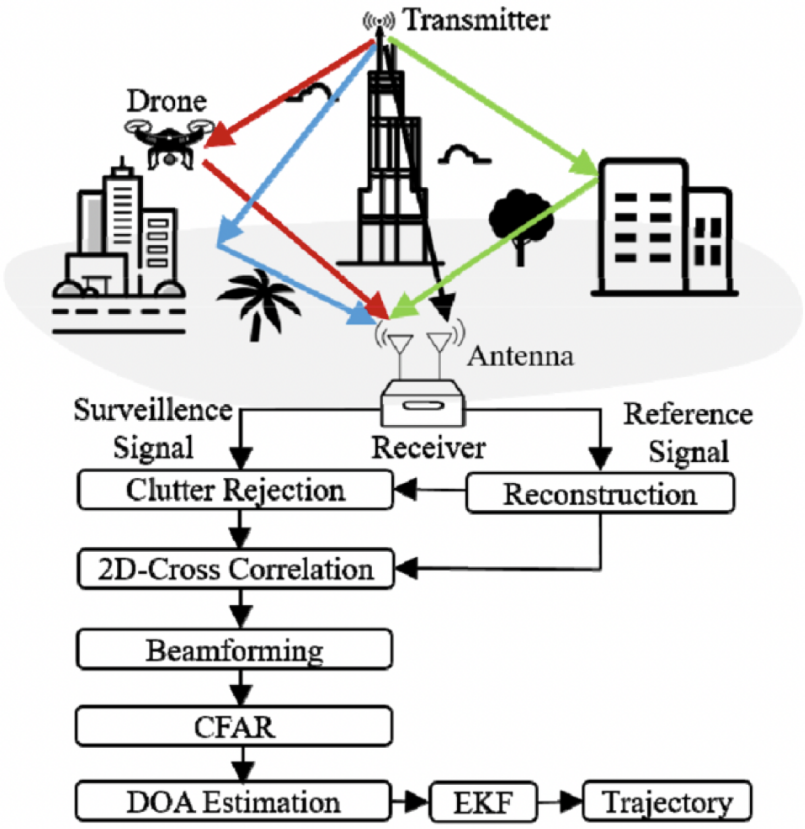


Figure 1.6: System block diagram for DVB drone detection in [6]

- The system shall be scalable and easily deployable,
- The system shall have graceful degradation capability,
- The system shall have performance comparable to conventional radar system alternatives.

## 1.2 Proposed Methods and Models

To satisfy the above mentioned requirements, we develop the MIMO cyclic spectral density analysis (MCSD) drone detection and localization method which uses novel techniques to perform detection and classification of drones jointly. Continuous wave (CW) radar signal is used which makes the radar system as simple as possible. The system basically relies on the cyclostationary analysis of drone radar echo signals

using the CSD transform.

In [19] the effectiveness of CSD in discriminating radar drone echo signals from the bird echo signals and noise is presented. The drone echo signal is typically placed in the $150 - 300$ Hz region in the cyclic frequency domain, the bird echo has a typical cyclic frequency of $2 - 20$ Hz according to the results in [19]. In [20] it is shown that the rotary motion of the radar targets induces a micro-Doppler effect on the radar echo signals. In [19] micro-Doppler effect is shown to have periodic structure in cyclic frequency. The main frequency on the cyclic frequency domain is the rotation frequency of the target, and the periodicity is due to the harmonics of the main frequency. As an example, the rotation frequency of automobile wheels is typically in the $0 - 25$ Hz region. So, the main cyclic frequency of the radar echo signal from the automobile wheel is between $0 - 25$ Hz. Also in [19] it is stated that stationary signals will have $0$ cyclic frequency. This fact limits the stationary clutter signals around $0$ Hz cyclic frequency. In [21] helicopter rotation frequency is given in the $4.3 - 8.18$ Hz interval. Respiration and heart beat effects on cyclic frequency are analyzed in [22].

If one tries to put this information into a graphical representation, Figure 1.7 will be achieved. It can be seen that the cyclic frequency is a good discriminator for radar return signals from drone propellers. The drone radar echo signal has periodic peaks in the CSD plane. In order to detect periodicity in the CSD plane and extract the contained information, a deinterleaving algorithm is used, which is an idea adopted from electronic support systems. After determining basic micro-Doppler parameters, the radial velocity related Doppler frequency is estimated using the information in the CSD plane. Localization of the micro-Doppler source is performed using knowledge of the Doppler frequencies.

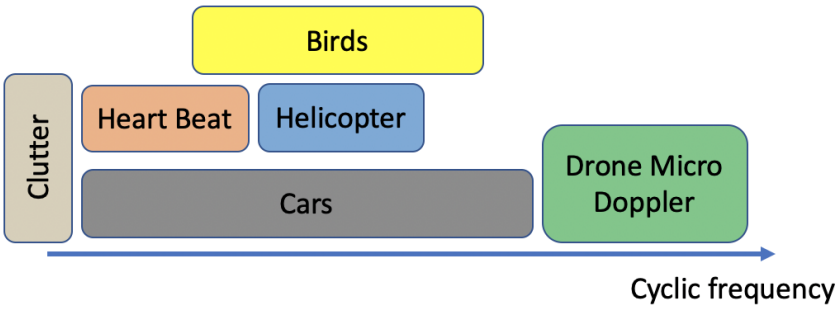


Figure 1.7: Some signals in the cyclic frequency plane

## 1.3 Contributions and Novelties

To the best of our knowledge the following features of the MCSD method are novel:

- Cost effective drone detection solutions for coverage limited regions is a popular topic in recent years as discussed in [23], [24], and [25]. In this thesis a solution to this problem, namely detecting drones in urban area is proposed. The architecture of the proposed system is MIMO radar with CW waveform which is stated in [23] as a cost effective solution.
- Deinterleaving algorithms are typically used in electronic warfare systems. In this thesis, the deinterleaving algorithm is used for the first time in radar drone detection.
- Cramer Rao Lower Bound (CRLB) for localization accuracy comparison between monostatic radar and MIMO radar is performed. General approach in the literature when discussing CRLB for localization accuracy of MIMO radars is comparing different configurations of MIMO radar, such as different numbers of transmitters and receivers. Differently from this approach, in this thesis, direct comparison of localization accuracy CRLB values of MIMO and monostatic radar systems is performed.
- In addition to proposing a MIMO drone detection radar system, deployment cost limits of using this MIMO radar system are derived. Cost limits are compared with monostatic radar costs. This comparison is important in evaluating

the economic effect of using a MIMO radar system.

- Cyclic spectral analysis based drone sensing studies in the literature are performed using a single drone. In this thesis multiple drone cases and multiple moving target cases are also covered and the effects of these targets are discussed.

## 1.4 The Outline of the Thesis

The organization of the thesis is as follows: The detailed signal model and the MCSD method are discussed in Chapter 2 and 3 respectively. In Chapter 4 the performance analysis of the MCSD method is shown. Chapter 5 develops a framework for the cost composition of our method and the conventional radar solution. The simulation and experimental results are shown in Chapter 6 and Chapter 7 concludes the thesis.

# CHAPTER 2

# SIGNAL MODEL

In this chapter the mathematical signal model of a radar echo signal from a drone is presented. This signal model is used in the simulations. The basic tool which is used in this thesis is CSD. The formulation of CSD and the output of the CSD for radar echo signal from a drone is also given. The RCS characteristics of drone body and propellers are presented in the last section of this chapter.

## 2.1 Propeller Return Signal Model

Since drone detection by radar has been studied in the literature, the radar return signals from drones is also covered in various studies. These signal models are mainly concentrated on radar return signal from drone's propellers. Apart from the return from propellers, the radar signal also returns from the drone's fuselage. Most of the studies in the literature on drone detection and classification are based on the propeller return signal since it has the main feature for classification, the micro-Doppler. In this thesis, drone detection and estimation is also based on micro-Doppler components. Therefore, the return signal from the propellers will be considered as the radar return signal from a drone, for simplicity. In [26] a detailed propeller signal model is derived, which is presented in equation (2.1).

$$s(t) = \sum_{n=0}^{N-1} A_r L \operatorname{sinc}(\frac{4\pi}{\lambda}\frac{L}{2}\cos(\theta)\sin(2\pi f_r t + \frac{2\pi n}{N}))\exp(j(2\pi f_c t - \frac{4\pi}{\lambda}(R + vt + \frac{L}{2}\cos(\theta)\sin(2\pi f_r t + \frac{2\pi n}{N})))) \tag{2.1}$$

In equation (2.1), following symbols are used:

- $L$: Length of the blade (meters)
- $N$: Number of blades
- $R$: Range from center of the rotation to the radar (meters)
- $t$: Time (seconds)
- $v$: Radial velocity of the center of rotation with respect to the radar (meters/seconds)
- $\lambda$ : Wavelength of the transmitted signal (meters)
- $\theta$ : Angle between the plane of rotation and the line of sight from the radar to the center of rotation (radians)
- $f_c$: Frequency of the transmitted signal (Hz)
- $f_r$: Frequency of rotation (Hz)
- $A_r$: Amplitude of the return signal

A similar signal model is also discussed in [21] and [27] for helicopter propeller echo signals and in [7], [19] and [28] for drone echo signals. It can be readily seen that the echo signal from the propeller has both amplitude modulation and phase modulation. Both amplitude and phase modulations are functions of the propeller rotation frequency. The phase term in equation (2.1) also includes the radial velocity term, $v$, which creates the Doppler effect on the signal. The phase term including the propeller rotation frequency creates the micro-Doppler effect.

Equation (2.1) is the radar return signal model from a single propeller. Drones have multiple rotors with propellers. Each rotor distance from the radar in [29] is found to be as in equation (2.2).

$$R = \sqrt{R_0^2 + d_k^2 - 2R_0 d_k \cos\theta_k} \tag{2.2}$$

In equation (2.2) $R_0$ is the range between the radar and the drone, $d_k$ is the distance between the rotor and the drone center, $\theta_k$ is the drone's $k^{th}$ arm angle relative to

the body plane of the drone. $\theta_k$ is given by the equation $\theta_k = \frac{\pi}{K}(2k-1)$, where $K$ is the number of propellers. Putting equation (2.2) in equation (2.1) and adding all propellers, one can obtain the radar return signal from the drone propellers as in equation (2.3).

$$s_d(t) = \sum_{n=0}^{N-1}\sum_{k=0}^{K-1} A_r L \,\mathrm{sinc}\Big(\frac{4\pi}{\lambda}\frac{L}{2}\cos(\theta)\sin(2\pi f_r t + \frac{2\pi n}{N})\Big)\exp\Big(j\big(2\pi f_c t - \frac{4\pi}{\lambda}\big(\sqrt{R_0^2 + d_k^2 - 2R_0 d_k \cos\theta_k} + vt + \frac{L}{2}\cos(\theta)\sin(2\pi f_r t + \frac{2\pi n}{N})\big)\big)\Big) \tag{2.3}$$

In Figures 2.1 and 2.2 amplitude and phase of a simulated propeller return signal are presented, respectively. The propeller is assumed to have one blade rotating at 10000 rpm and moving with a velocity of -1 m/s with respect to radar which operates at 24 GHz. The Doppler and micro-Doppler components on phase term are readily present in the phase figure. The amplitude has peaks twice the rotation frequency since blade faces radar twice a turn. The micro-Doppler on phase term has frequency equal to the rotation frequency of the propeller.

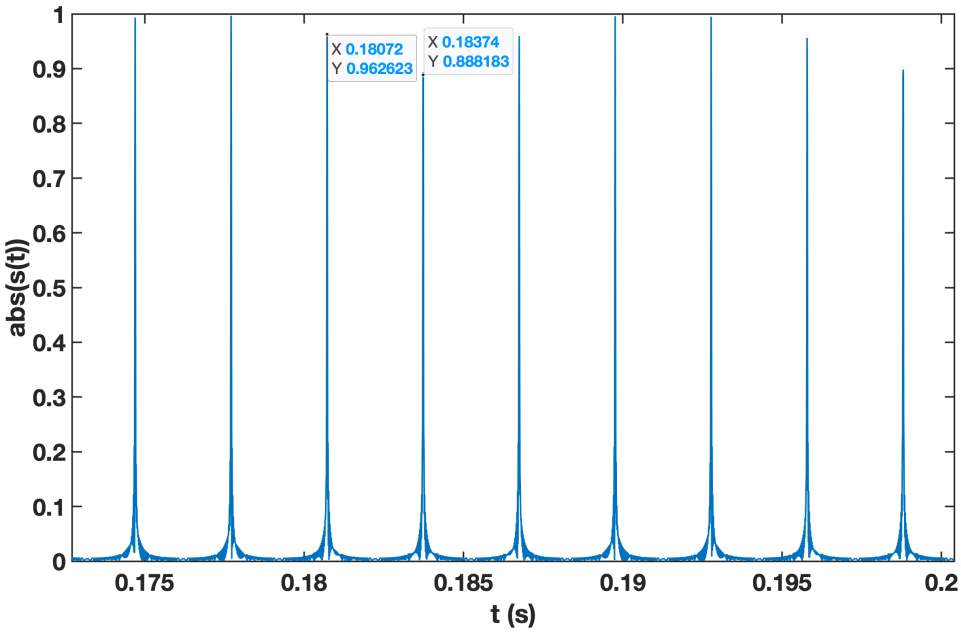


Figure 2.1: Amplitude of the simulated propeller signal

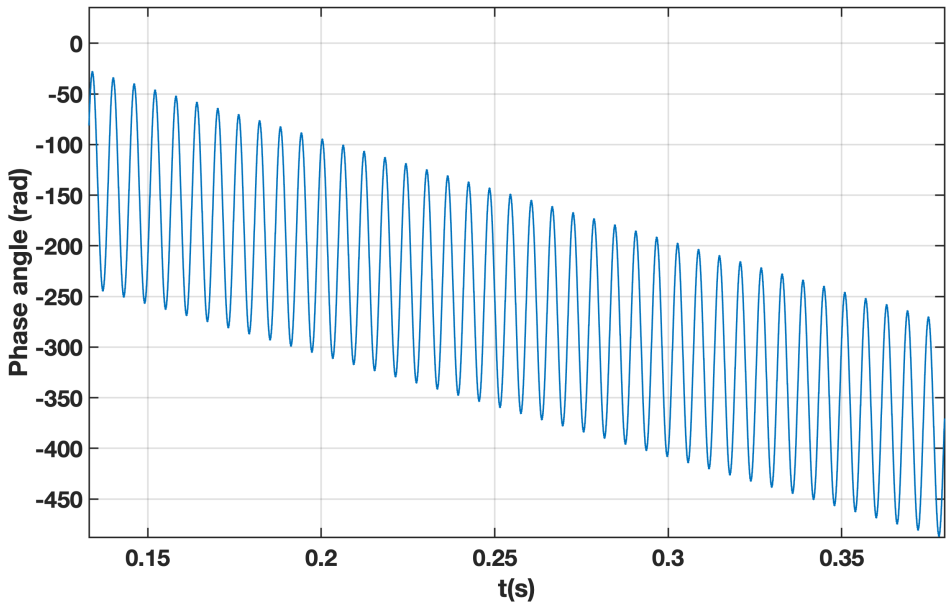


Figure 2.2: Phase of the simulated propeller signal

## 2.2 Propeller Return Signal in Frequency Domain

In order to find the Fourier transform of the signal model in equation (2.1) let us divide the propeller signal model into two parts as

$$s(t) = s_1(t)s_2(t) \tag{2.4}$$

where

$$s_1(t) = \exp\left(j(2\pi f_c t - \frac{4\pi}{\lambda}(R + vt))\right) \tag{2.5}$$

$$\begin{aligned} s_2(t) = \sum_{n=0}^{N-1} & A_r L \,\mathrm{sinc}(\frac{4\pi}{\lambda}\frac{L}{2}\cos(\theta)\sin(2\pi f_r t + \frac{2\pi n}{N})) \\ & \exp\left(j(\frac{4\pi}{\lambda}\frac{L}{2}\cos(\theta)\sin(2\pi f_r t + \frac{2\pi n}{N})\right) \end{aligned} \tag{2.6}$$

$s_1(t)$ includes the frequency, phase, and Doppler shift terms. $s_2(t)$ includes the amplitude and phase modulation caused by the propeller rotation motion. It is readily

seen that $s_2(t)$ is a periodic function with a period of $T_r = 1/f_r$. This fact leads us to the fact that $s_2(t)$ can be written in the form of Fourier series as in equation 2.7.

$$s_2(t) = \sum_{k=-\infty}^{\infty} c_k \exp\left(j2\pi k f_r t\right) \tag{2.7}$$

The Fourier series coefficients $c_k$ can be calculated using the well known equation in 2.8.

$$c_k = \frac{1}{T_r} \int_{T_r} s_2(t) \exp\left(-j2\pi k f_r t\right) dt \tag{2.8}$$

The Fourier transform of $s_2(t)$ can be written using the Fourier series coefficients as in equation 2.9.

$$S_2(f) = \sum_{k=-\infty}^{\infty} c_k \delta(f - k f_r) \tag{2.9}$$

Then the Fourier transform of $s(t)$ can be written using the frequency shifting property of the Fourier transform considering $s_1(t)$ as in equation 2.10. The term $f_d$ refers to the Doppler shift frequency and is equal to $2v/\lambda$.

$$S(f) = \sum_{k=-\infty}^{\infty} c_k \exp\left(-j\frac{4\pi}{\lambda}R\right) \delta(f - f_c - f_d - k f_r) \tag{2.10}$$

The calculation of the Fourier coefficients is studied in [30] and it was proved that the Fourier coefficients $c_k$ values are non-zero only when the values of $k$ are integer multiples of $N$. Considering the equation (2.10), where where $d_k = c_{Nk} \exp\left(-j\frac{4\pi}{\lambda}(R)\right)$ ([26], [30]), equation (2.10) can be rewritten as in equation 2.11.

$$S(f) = \sum_{k=-\infty}^{\infty} d_k \delta(f - f_c - f_d - kN f_r) \tag{2.11}$$

$d_k$ values are given in equation (2.12) ([26], [30]). The derivation of equation (2.12)

is presented in Appendix-A.

$$d_k = \sum_{l=0}^{\infty} \frac{2(-1)^{Nk} ArN}{\frac{4\pi}{\lambda}\cos(\theta)} \left( J_{N|k|+2l+1} \left( \frac{4\pi}{\lambda} L\cos(\theta) \right) \right) exp\left( -j\frac{4\pi}{\lambda} R \right) \tag{2.12}$$

where $J_k(x)$ is the $k^{th}$ order Bessel function of the first kind.

Using equation 2.11, the signal $s(t)$ can also be written as in equation 2.13.

$$s(t) = \exp(j2\pi f_c t) \exp(j2\pi f_d t) \sum_{k=-\infty}^{\infty} d_k \exp(j2\pi N k f_r t) \tag{2.13}$$

Equation (2.11) is derived for a single propeller signal presented in equation (2.1). Since equation (2.3) is the summation of equations (2.1), the same form of the Fourier transform in equation (2.11) will also be valid for equation (2.3). Fourier transform of the signals in Figures 2.1 and 2.2 is shown in Figure 2.3. This figure shows the expected behaviours presented in equation (2.11). Delta functions are periodically separated by frequency with the rotation period of the propeller. Also, the peaks are shifted to the left according to the Doppler frequency of the signal, which is equal to 160 Hz. If the propeller has two blades, due to the symmetry, the Delta functions are separated in frequency periodically with the two times the rotation period of the propeller. This fact is shown in Figure 2.4. This fact is also discussed in [26].

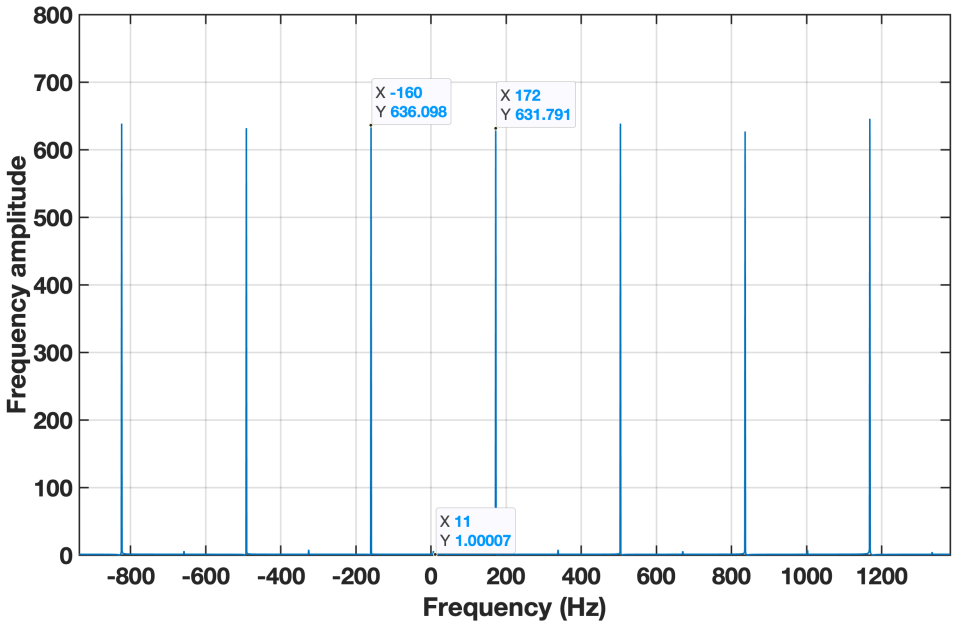


Figure 2.3: Amplitude of the Fourier transform of the simulated propeller signal with one blade

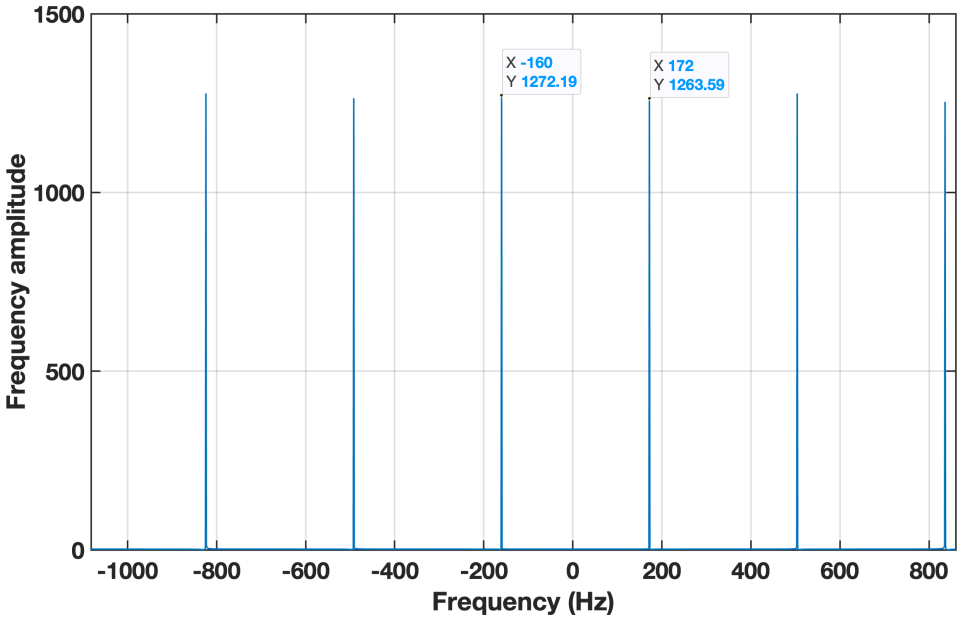


Figure 2.4: Amplitude of the Fourier transform of the simulated propeller signal with 2 blades

## 2.3 Cyclostationary Signal Analysis

The autocorrelation function of a complex signal $x(t)$ is defined in [31] and [32] as in equation (2.14).

$$R_x(t,\tau) = E[x(t+\tau/2)x^*(t-\tau/2)] \tag{2.14}$$

In equation (2.14) $E$ stands for the expectation operator, and $*$ is for the conjugate operator. If a signal is second order wide sense stationary then $R_x(t,\tau)$ does not depend on absolute time $t$, it only depends on $\tau$. For this case, the autocorrelation function can be represented as $R_x(t,\tau) = R_x(\tau)$.

Cyclostationary signals have autocorrelation functions depending on absolute time, and also the autocorrelation function exploits periodicity as a function of absolute time. According to [28] a signal is cyclostationarity if its autocorrelation function satisfies equation (2.15) for $T_0 \neq 0$.

$$R_x(t,\tau) = R_x(t+T_0,\tau) \tag{2.15}$$

Equation (2.15) defines a periodic function which means that it has a Fourier series representation. According to [28], the Fourier series representation of $R_x(t,\tau)$ can be written as in equation (2.16).

$$R_x(t,\tau) = \sum_{k=-\infty}^{\infty} R_x^{\alpha_k}(\tau) e^{j2\pi k\alpha_0 kt} \tag{2.16}$$

In equation (2.16) $R_x^{\alpha_k}$ are the Fourier series coefficients of $R_x(t,\tau)$, $\alpha_0 = 1/T_0$, $\alpha_k = k\alpha_0$. The Fourier series coefficients $R_x^{\alpha_k}$ are given in equation (2.17) ([28]).

$$R_x^{\alpha_k}(\tau) = \frac{1}{T_0}\int_{-T_0/2}^{T_0/2} R_x(t,\tau) e^{-j2\pi k\alpha_0 t} dt \tag{2.17}$$

As stated in [33], for a finite energy autocorrelation function, the cyclic autocorrelation function is described as in equation (2.18) for continuous values of $\alpha$. This

concept is very similar to the Fourier Series and Fourier Transform discussed in [34]. In equation (2.18) $\alpha$ is called as the cyclic frequency. Although signals exhibiting periodicity as a function of $t$ do not have finite energy, equation (2.18) can also be used as stated in [34].

$$R_x^{\alpha}(\tau) = \int_{-\infty}^{\infty} R_x(t,\tau) e^{-j2\pi\alpha t} dt \tag{2.18}$$

If one wants to represent equation (2.16) in the spectral frequency (f) domain, the cyclic spectral density (CSD) is obtained. In [7] CSD is formulated as in equation (2.19).

$$S_x^{\alpha}(f) = \int_{-\infty}^{\infty} R_x^{\alpha}(\tau) e^{-j2\pi f\tau} d\tau. \tag{2.19}$$

CSD is basically the transformation that shows the spectral density among different cyclic frequencies. For stationary signals, the spectral density is at $\alpha = 0$, but for cyclostationary signals, the spectral density is distributed over different cyclic frequencies. As a representation, the CSD has two frequency axes, one is the cyclic frequency $\alpha$ and the other is the spectral frequency $f$. A sample CSD from the literature is presented in Figure 2.5.

According to [35], many man made signals such as communication, telemetry, radar, and sonar signals exploit cyclostationarity. The cyclostationarity property of the signals is used to discriminate them from other signals. In equation (2.11) the Fourier transform of the signal is composed of weighted dirac delta functions. In [19] it is stated that since equation (2.11) consists of a series of lines with a frequency interval $Nf_r$, $s(t)$ is cyclostationary. If we turn our attention to the drone signal $s(t)$ considering it in the base band, then the instantaneous auto-correlation function of $s(t)$ can be written as in equation (2.20) ([19]).

$$\begin{aligned} y_\tau(t) =& s(t+\frac{\tau}{2}) s^*(t-\frac{\tau}{2}) = \\ & \sum_m \sum_n d_m d_n \exp\left( j2\pi(f_d + nf_r)(t+\frac{\tau}{2}) - j2\pi(f_d+nf_r)(t-\frac{\tau}{2}) \right) \end{aligned} \tag{2.20}$$

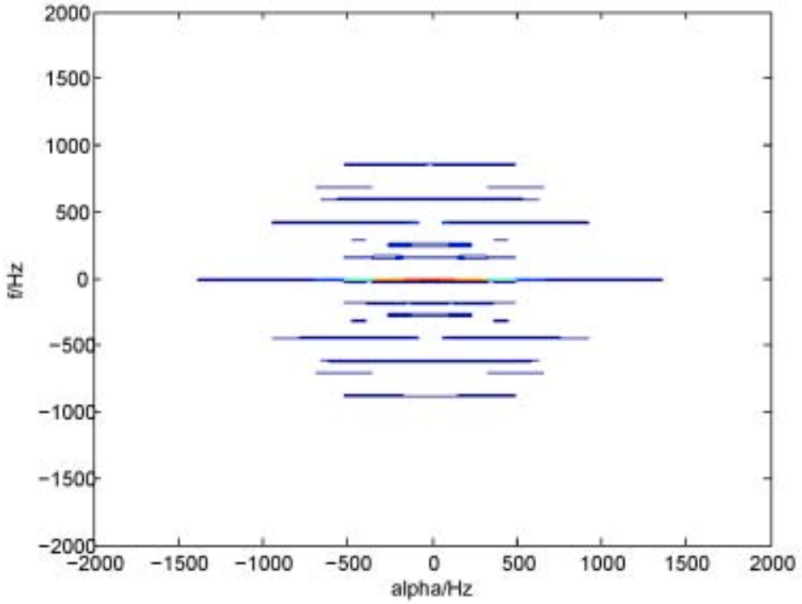


Figure 2.5: Sample CSD from literature ([7])

Under the assumption that the observation is within the interval $[-T/2, T/2]$, the cyclic autocorrelation function of $s(t)$ is given in [19] which is repeated here for convenience in equation (2.21). The cyclic spectrum density of $s(t)$ is found to be as in (2.22) ([19]). As stated in [19], for large values of $T$, $S_s^\alpha(f)$ will be non-zero for the values of $f$ and $\alpha$ in equation (2.23).

$$R_s^\alpha(\tau) = \int_{-T/2}^{T/2} y_\tau(t) \exp(-j2\pi\alpha t)\, dt = \sum_m \sum_n d_m d_n \exp(j2\pi f_d \tau) \exp(j\pi(m+n) f_r \tau) \operatorname{sinc}(\pi(f_r(m-n) - \alpha)T) \tag{2.21}$$

$$S_s^\alpha(f) \triangleq \int_{-\infty}^{\infty} R_x^\alpha(\tau) \exp(-j2\pi f\tau)\, d\tau = \sum_m \sum_n d_m d_n \delta[2\pi(f - f_d - \frac{m+n}{2} f_r] \operatorname{sinc}[\pi(f_r(m-n) - \alpha)T] \tag{2.22}$$

$$\begin{aligned} f &= f_d + \frac{m+n}{2} f_r \\ \alpha &= (m-n) f_r \end{aligned} \quad m, n \in Z \tag{2.23}$$

Equation (2.23) states that for micro-Doppler signals generated by a propeller, the CSD will be periodic in both cyclic and spectral frequencies. There will be peaks in the cyclic frequency at integer multiples of $f_r$. In the spectral frequency domain, there will be peaks at the integer multiples of $f_r$. The spectral frequency is shifted in relation to the radial motion of the propeller compared to that of the radar. In Figure 2.6, a sample CSD is presented for a propeller rotating at approximately 3400 rpm with two blades. The periodicity in the cyclic and spectral frequencies is obvious.

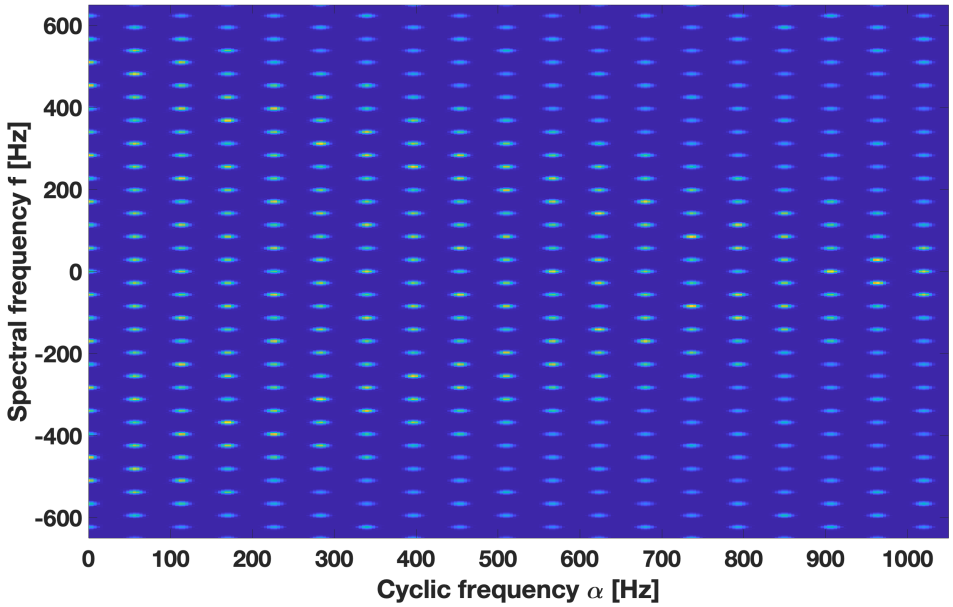


Figure 2.6: Sample CSD of a propeller

In this thesis, CSD estimation with the averaged cyclic periodogram is used which is given in [36] and [37] is used. The cyclic frequency resolution ($\Delta_\alpha$) and the spectral frequency resolution ($\Delta_f$) of CSD are given in [37] as in equations (2.24) and (2.25), respectively.

$$\Delta_\alpha \sim \frac{F_s}{L} \tag{2.24}$$

$$\Delta_f \sim \frac{F_s}{N_w} \tag{2.25}$$

In equations (2.24) and (2.25) $L$ stands for the total number of samples of the signal,

$F_s$ is the sampling frequency, and $N_w$ is the number of samples in the window. The window is a shifting window, like in the Welch's spectral density estimation. A portion of the signal, which is the signal in the window, is used in CSD calculation. This process is repeated, and the results are averaged. The details are given in [36].

The equation (2.24) states that the cyclic frequency resolution depends on the signal length and the sampling frequency. Desired cyclic frequency resolution values can be obtained by adjusting these parameters. The simulations in this thesis are performed for a 250 ms signal duration at a sampling rate of 44.1 KHz. Therefore, the cyclic frequency resolution becomes approximately 4 Hz for our results. By changing the signal length, the cyclic frequency resolution can be easily adjusted. The Hanning window with a window length of 8192 is used as the smoothing window.

In equation (2.25) the spectral frequency resolution is presented. The spectral frequency resolution similar to the cyclic frequency resolution and depends on the sampling frequency. Since a windowing function is used, the length of the window affects the spectral frequency resolution. In this thesis the Hanning window with a length of 8192 is used. So the approximate spectral frequency is 5.4 Hz. The resolution can be adjusted with the sampling frequency, signal duration, and the windowing function.

CSD is very similar to the well known time-frequency analysis method Wigner Ville Distribution (WVD). The WVD is defined as in equation (2.26) ([36]), where $W_x(t, f)$ is the WVD of signal $x(t)$.

$$W_x(t, f) = \int_{-\infty}^{\infty} R_x(t, \tau) exp(-j2\pi f\tau) d\tau \tag{2.26}$$

Then CSD can be represented as the Fourier transform of $W_x(t, f)$ with respect to absolute time, $t$ as given in equation (2.27) ([36]).

$$S_s^{\alpha}(f) = \int_{-\infty}^{\infty} W_x(t, f) exp(-j2\pi\alpha t) dt \tag{2.27}$$

## 2.4 Propeller RCS

RCS of drones is an important parameter which challenges radar systems to detect drones. There are numerous publications about drone RCS in the literature in which both theoretical and experimental results are studied. Both the size and the materials used in drones lead to low RCS characteristics. In [8] the material percentage of the DJI Phantom 2 Vision drone is shown as in Figure 2.7. Plastic is the most used component in drones, leading to lower RCS values.

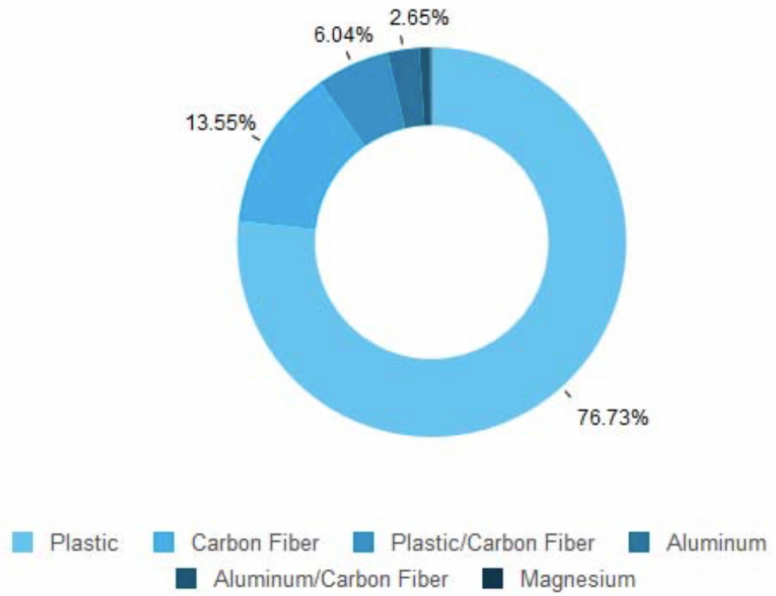


Figure 2.7: Drone material percentage ([8])

The RCS measurement results for the DJI Phantom 2 Vision drone are given in [8]. Measurements are made in both the anechoic chamber and the open field. The results of the anechoic chamber and the open field are shown in Figure 2.8 and Figure 2.9, respectively. According to these results in the anechoic chamber, RCS varies between -7 dBsm and -25 dBsm. In open field, RCS variation is between -10 dBsm and -17 dBsm.

In this thesis, the magnitudes of the micro-Doppler components are of our interest, since the MCSD method works directly on these components. In [38] - [39] propeller RCS, in other words, the magnitudes of the micro-Doppler components are studied. Also in [40] a survey of drone RCS publications is covered. According to

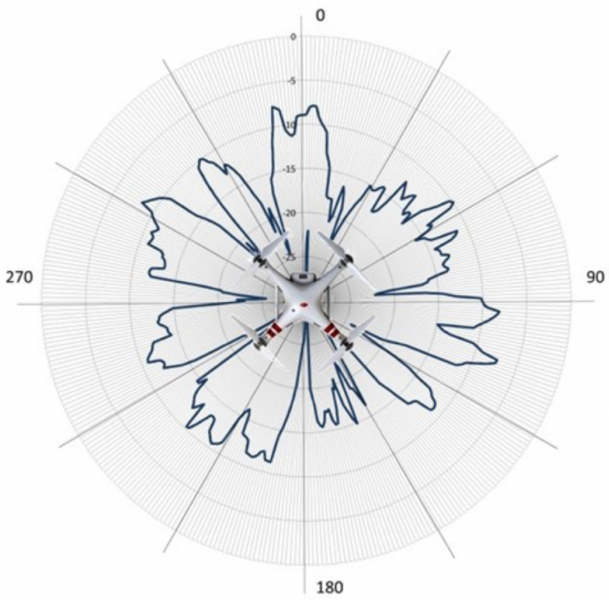


Figure 2.8: DJI Phantom Vision RCS in anechoic chamber ([8])

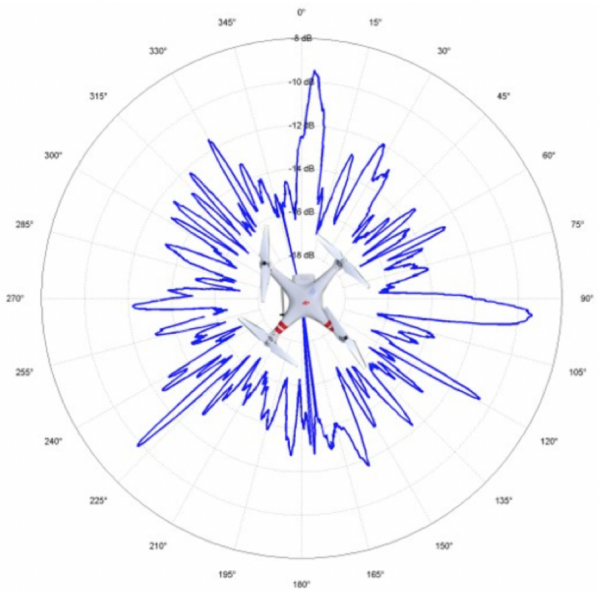

Figure 2.9: DJI Phantom Vision RCS in open field ([8])

these papers, the micro-Doppler magnitude is highly dependent on the frequency and polarization of the radar signals. According to [40] a relative amplitude disparity of approximately -20 dB between the drone body and the micro-Doppler components is a reasonable assumption. Conventional radar systems experience this RCS difference

challenge in classification whereas the MBCD method in detection. The effects of this fact are considered in Chapters 4 and 5.

# CHAPTER 3

# MIMO MCSD METHOD

In this chapter, algorithmic flow of the MCSD method is presented. Before algorithmic details, an introduction to basic radar concept is covered. After the first section, all steps of the MCSD method are defined in detail in the following sections.

## 3.1 Introduction

As a basic radar concept, electromagnetic energy is generated by a transmitter and radiated by the transmitting antenna in the direction of the target. Some of the energy reflected by the target is collected by the receiving antenna and processed in the receiver to produce information about the target ([41]). Information about a target includes ([41]):

- The target presence, indicated by a signal return larger than the background.
- Target range found from the round-trip propagation time, t. For monostatic radars, the range R is calculated by the equation (3.1).

$$R = \frac{ct}{2} \tag{3.1}$$

  In equation (3.1), $R$ is the range between the radar and the target, $c$ is the speed of light and $t$ is the time difference between the electromagnetic wave leaves the radar and returns back to the radar.

- Target radial velocity, which is the target's velocity vector component on the line of sight vector between the radar and the target. In equation (3.2) the

equation for the calculation of the radial velocity is presented where $v$ is the radial velocity, $f_d$ is the Doppler frequency shift on radar return waveform and $\lambda$ is the wavelength of the radar waveform.

$$v = \frac{f_d \lambda}{2} \tag{3.2}$$

- Target direction, found from the antenna beam orientation for maximum signal return. There are different direction finding methods for radar in the literature such as monopulse direction finding, sequential scan direction finding, and conical scan direction finding methods.

- Target characteristics, found from the magnitude and features of the signal return, such as fluctuations characteristics, duration, and spectrum features.

Radars are generally classified as monostatic and bistatic radars according to their transmitter and receiver positions. Monostatic radar has its transmitter and receiver colocated compared to the target range. Generally, a single antenna is used for both transmit and receive purposes. Most of the radars are in monostatic configuration.

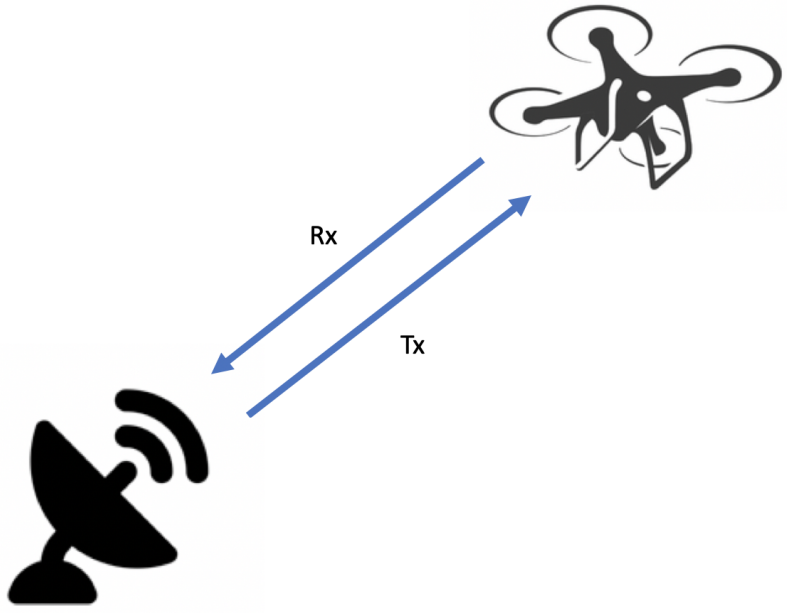


Figure 3.1: Basic monostatic radar configuration

Different from monostatic radars, bistatic radars have its transmitter and receiver separated so that transmitter and receiver see different aspects of target.

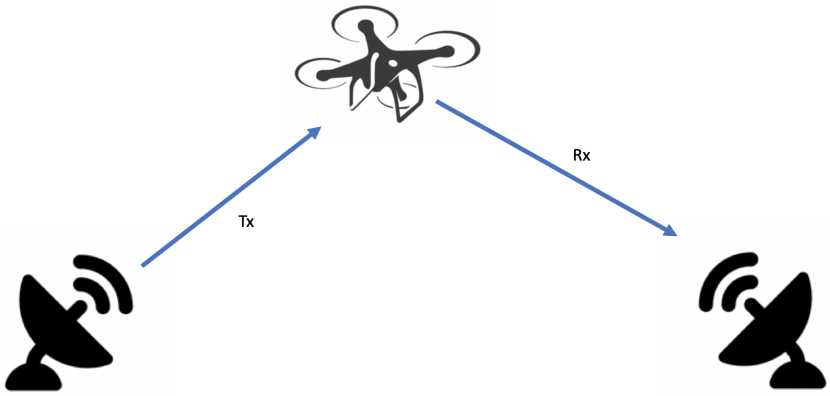


Figure 3.2: Basic bistatic radar configuration

In addition to monostatic and bistatic radars, in recent years MIMO radars have received attention. A MIMO radar has multiple transmitters and receivers in its structure. According to the placement of these transmitters and receiver MIMO radars are classified as widely separated (distributed) MIMO radars and co-located MIMO radars.

In this thesis, the distributed MIMO radar term is preferred for widely separated MIMO radar. The basic structure of the distributed MIMO radar is shown in Figure 3.3. Transmitters and receivers can be in monostatic or bistatic configuration.

The main motivation of the distributed MIMO radar is to see different aspects of the target and, as a result, see different RCS values of the target. If one pair of transmitter/receiver sees low RCS, another transmitter/receiver pair sees probably high RCS due to rapid change in RCS with aspect angle (Figure). This fact is discussed in [42]. In [42] it has been shown that this configuration leads to better detection and localization performance compared to monostatic radars.

In [9] co-located MIMO radar is proposed. Structurally co-located MIMO radar is similar to a phased array radar. Unlike the phased array radar, the co-located MIMO radar transmits different waveforms from antenna elements of an array antenna. In [9] it was stated that the waveform diversity in co-located MIMO radar has the following

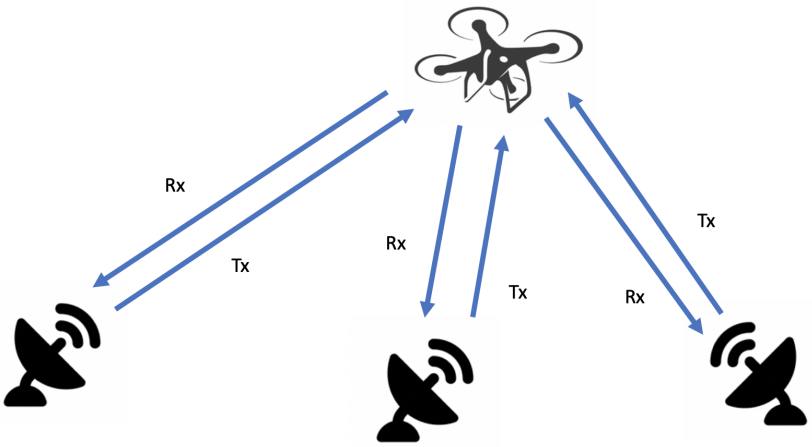


Figure 3.3: Basic MIMO radar configuration

benefits:

- Significantly improved parameter identifiability,
- Direct applicability of adaptive arrays for target detection and parameter estimation,
- Much enhanced flexibility for transmit beampattern design.

According to the waveform used, radars are grouped into two, CW radars and pulsed radars.

- CW radars: CW radars transmit a continuous wave signal to detect targets. With a CW signal, a radar can detect a target and measure the Doppler frequency shift, in other words, the radial velocity of the target. Range information is missing if no modulation is applied to the CW waveform. In order to get range information, frequency modulation is used in CW radars and these types of radars are called Frequency Modulated Continuous Wave (FMCW) radars. A typical time-frequency figure for an FMCW radar is presented in Figure 3.6. The range information is extracted from the time difference between the transmitted and received frequencies, which is shown in Figure 3.6 as $\Delta t$. The Doppler frequency information is also shown in Figure 3.6 as $f_d$.

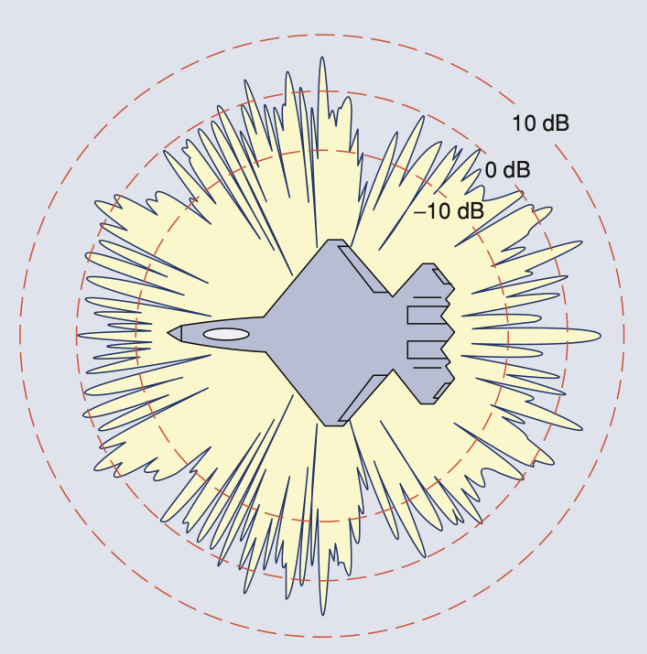


Figure 3.4: RCS as a function of aspect angle

- Pulsed radars: Pulsed radars use pulse type waveforms. During transmission, a pulsed waveform is transmitted. After this period, receiving is performed by the radar. Radar measures the time difference between pulse transmit and receive in order to extract the target range information. The pulsed radar waveform is generally characterized by pulse width and pulse repetition. A typical pulsed radar waveform envelope is shown in Figure 3.7.

Drone detection by radar has been a popular research topic in recent years due to the availability of commercial drones. Some of the challenges of drone detection by radar can be listed as follows:

- The radar cross section (RCS) of drones is typically very small compared to other targets. In [8], RCS measurement results are presented for different types of drones. Also in [43] RCS values of different drones for different frequency bands are presented. It is seen that the RCS values of drones can be as low as -20 dBsm.
- Drones can move very slowly, and they can be buried in ground clutter, especially when they are flying at low altitudes. Doppler shift is an important

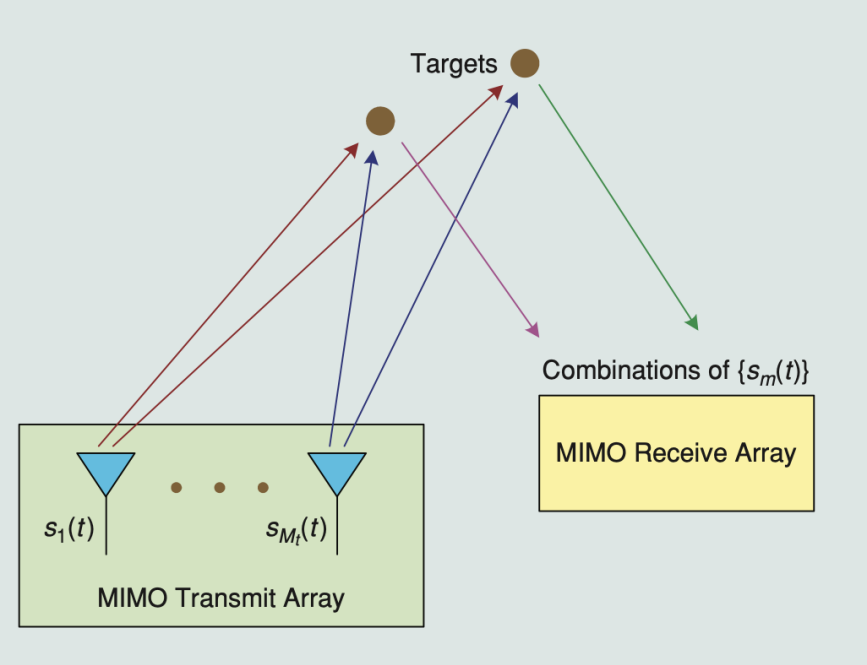


Figure 3.5: Co-located MIMO radar structure ([9])

feature that helps radars distinguish moving targets from clutter.

- For urban areas, radar coverage is very limited due to the presence of buildings.

The main motivation of this work is to design a drone detection and localization system with minimal cost for urban areas. In order to accomplish this task, the simplest form of radar, namely the continuous wave (CW) radar, is used. A single radar will be responsible for the detection of a drone and the determination of the Doppler frequency shift. In order to localize a moving drone, multiple CW radars will be used and Doppler-only target localization will be performed. This structure belongs to the distributed MIMO radar structure.

The main flow of the MCSD method is shown in Figure 3.8. This flow is implemented in a single radar. At the output of the flow the Doppler frequency of the drone is calculated. In order to construct a system solution, multiple radar nodes have to be used with the same MCSD method. In Figure 3.9 the overall system solution is presented. Although monostatic, bistatic, and multistatic radar configurations can be used in the MCSD method, monostatic operation of each CW radar is developed in this thesis for the sake of simplicity.

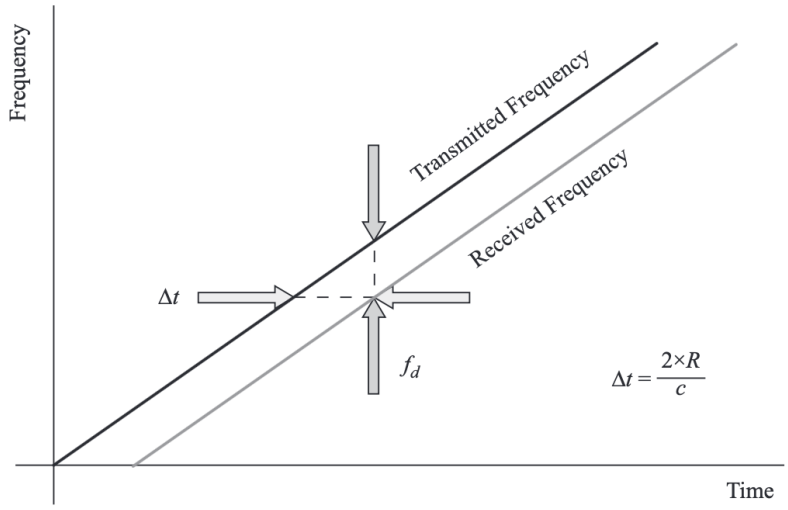


Figure 3.6: FMCW waveform time frequency relation ([10])

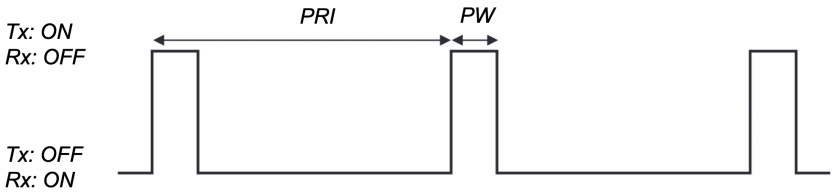


Figure 3.7: Pulsed radar waveform envelope ([11])

Each step of the MCSD method will be described in the following subsections.

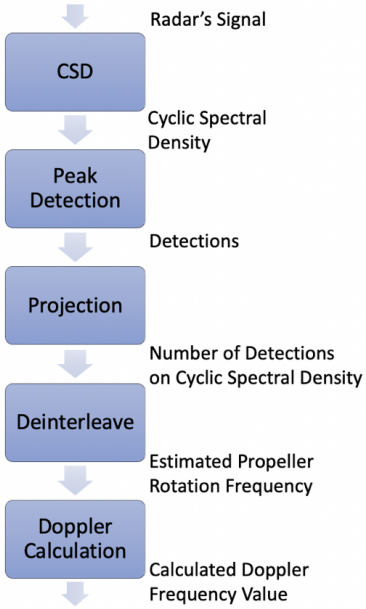


Figure 3.8: MCSD method in a single radar system

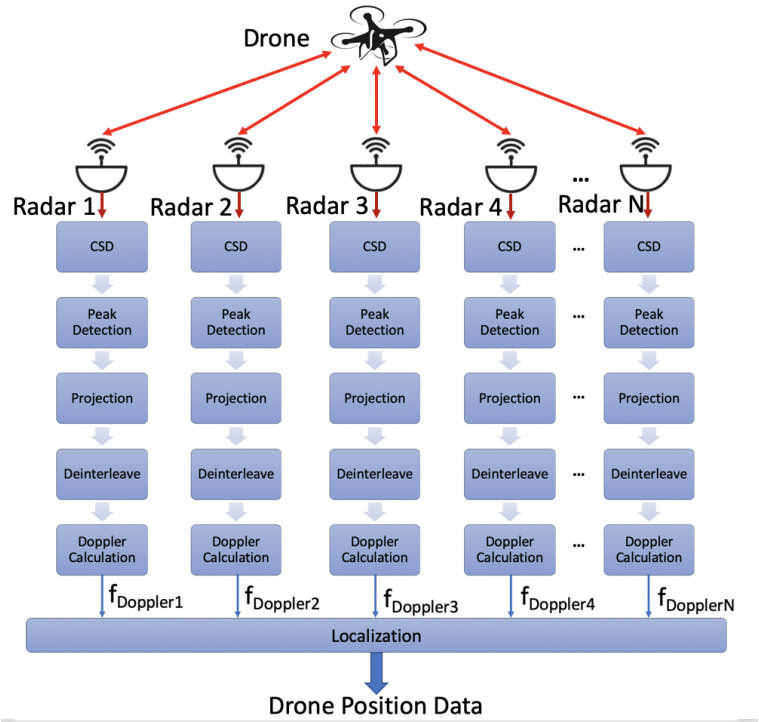


Figure 3.9: MCSD method as a system solution

## 3.2 CSD

The periodic motion of propellers creates micro-Doppler effect, and as presented in Section 2.3, radar return from propellers creates a periodic structure in the CSD plane. The equation for the periodic structure is given in equation (2.23).

In Figure 3.10 the peaks in the CSD along cyclic frequency axis are shown schematically where the peaks are placed periodically with a frequency of $f_r$. Along the spectral frequency axis, the peaks of CSD also have a period of $f_r$. This structure in CSD represents a cyclostationary signal.

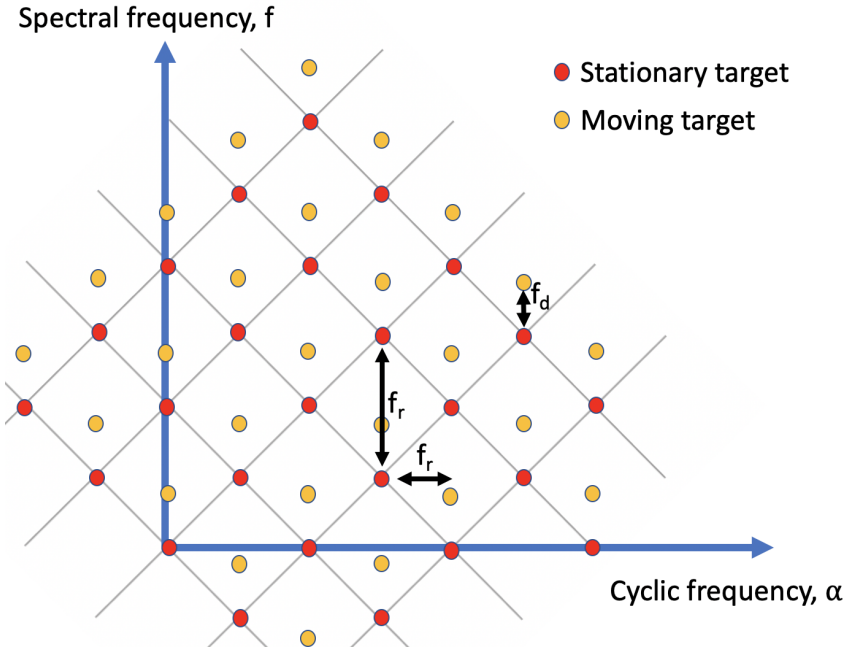


Figure 3.10: Representation of drone propeller signal in the CSD

To show this effect with simulation, a propeller signal is generated for a 5 GHz radar. In Figure 3.11 CSD of a stationary propeller with one blade is shown. The propeller rotates at a frequency of 100 Hz. The periodic structure along both the cyclic and spectral frequencies with the main frequency of 100 Hz is readily seen. The structure coincides with the schematic drawing in Figure 3.10.

The number of blades in the propeller affects the main frequency structure in the CSD. To show this effect, the configuration in Figure 3.11 is used with a 2 blade propeller. The propeller is rotating at 100 Hz. As in Figure 3.12 since the propeller has 2 blades,

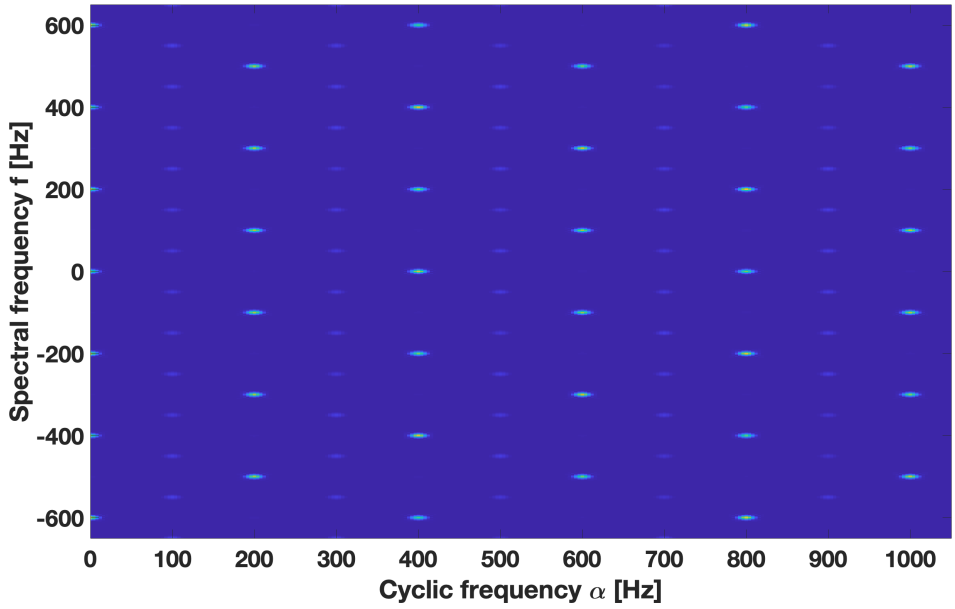


Figure 3.11: Radar signal from a drone stationary propeller with 1 blade in the CSD

the main frequency along both cyclic and spectral frequencies is 200 Hz. The main structure in the CSD is not affected but the main frequency is changed as a multiple of the number of blades.

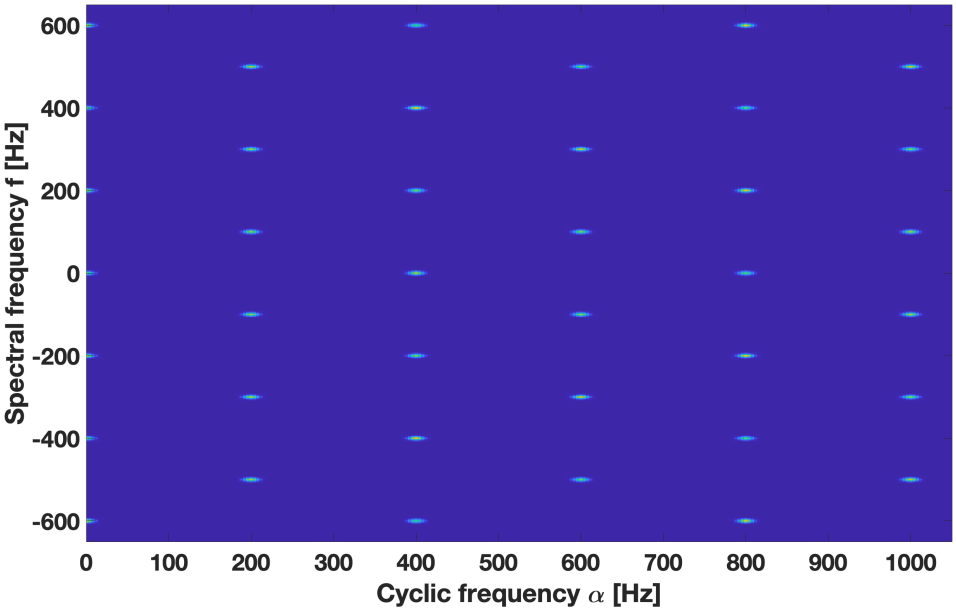


Figure 3.12: Radar signal from a stationary drone propeller with 2 blades in the CSD

The periodic structure in the CSD moves along the spectral axis in relation to the

Doppler frequency caused by the motion of the drone. The cyclostationarity, propeller rotation frequency and the Doppler frequency are present in the CSD. To see this effect, the radar and propeller in Figures 3.11 and 3.12 are used. This time, the propeller is moving with a radial velocity of 1 m/s. In Figure 3.13 the 33 Hz Doppler shift along the spectral axis can be observed compared to Figure 3.11.

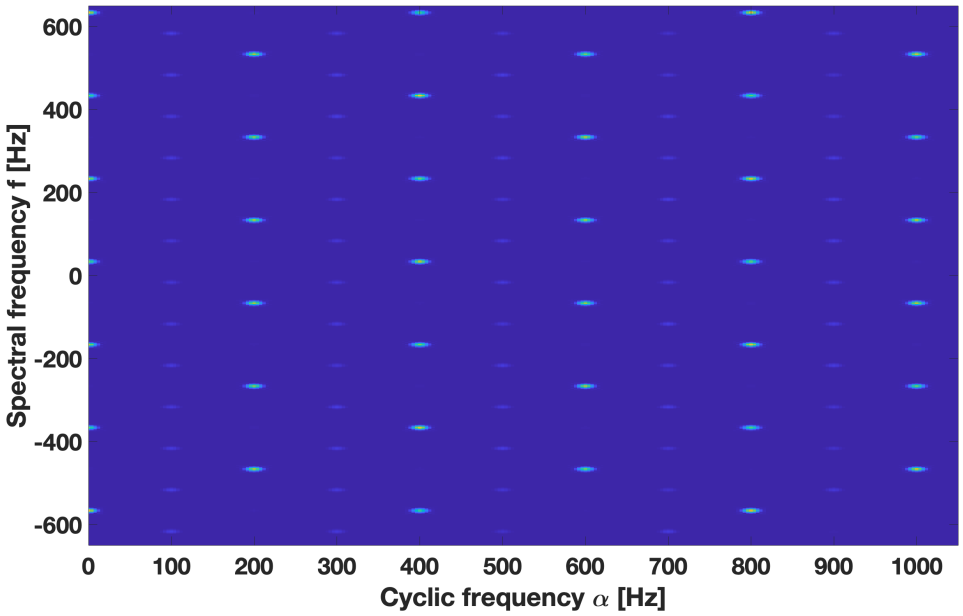


Figure 3.13: Radar signal from a moving drone propeller with 1 blade in the CSD

The same Doppler shift effect is still present when the number of blades is 2. The CSD for moving propeller with 2 blades is shown in Figure 3.14.

With proper processing, the presence of a rotary wing drone, the frequency of rotation and the Doppler frequency shift caused by the radial motion of the propeller can be gathered from CSD. Therefore, as a first step of the MCSD method, the signals obtained from each CW radar are transformed into the CSD domain.

As discussed in Section 1.2, cyclostationarity cannot be seen for typical ground moving targets and clutter. As an example, the CSD of a target with no propellers is shown in Figure 3.15. Unlike Figures 3.11 - 3.14 there is no periodicity neither on the cyclic frequency axis nor on the spectral frequency axis. The peak of CSD is placed at 0 Hz cyclic and spectral frequency. The effect of radial motion of a target in the CSD is shown in Figure 3.16. Differently from the Figure 3.15 the peak is shifted along

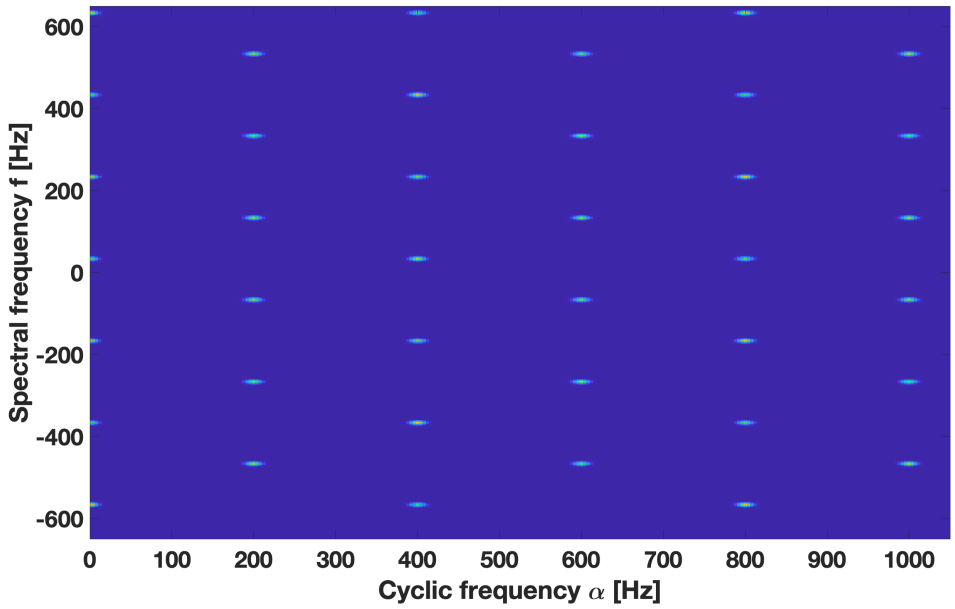


Figure 3.14: Radar signal from a moving drone propeller with 2 blade in the CSD

the spectral axis according to the radial speed of the target, which is 1 m/s. Also in Figure 3.16 there is no periodicity.

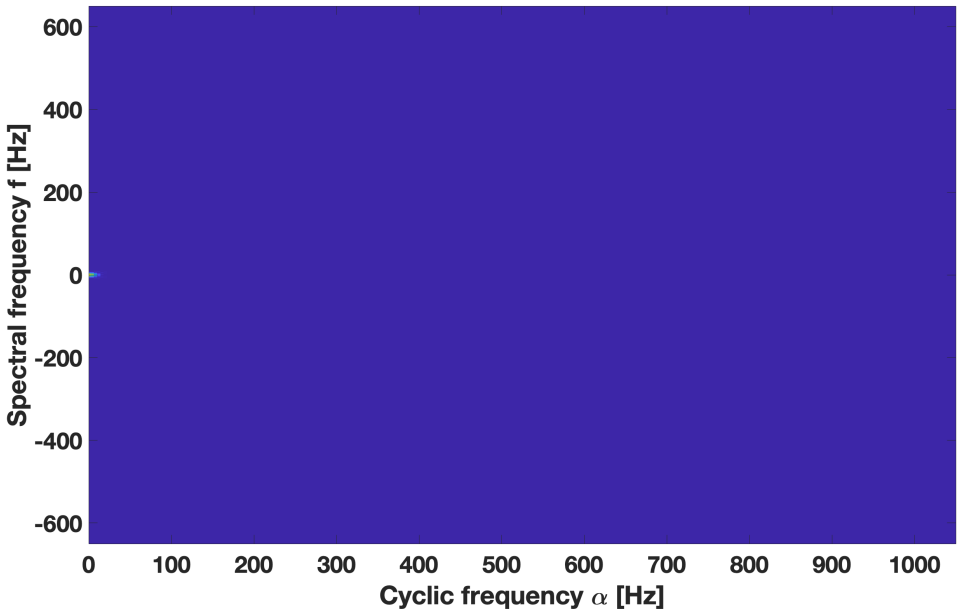


Figure 3.15: Radar signal from a stationary target in the CSD

Since drones have small RCS values and can fly at very low speeds, radar return signals from the propellers of the drones can be distinguished from non-drone targets

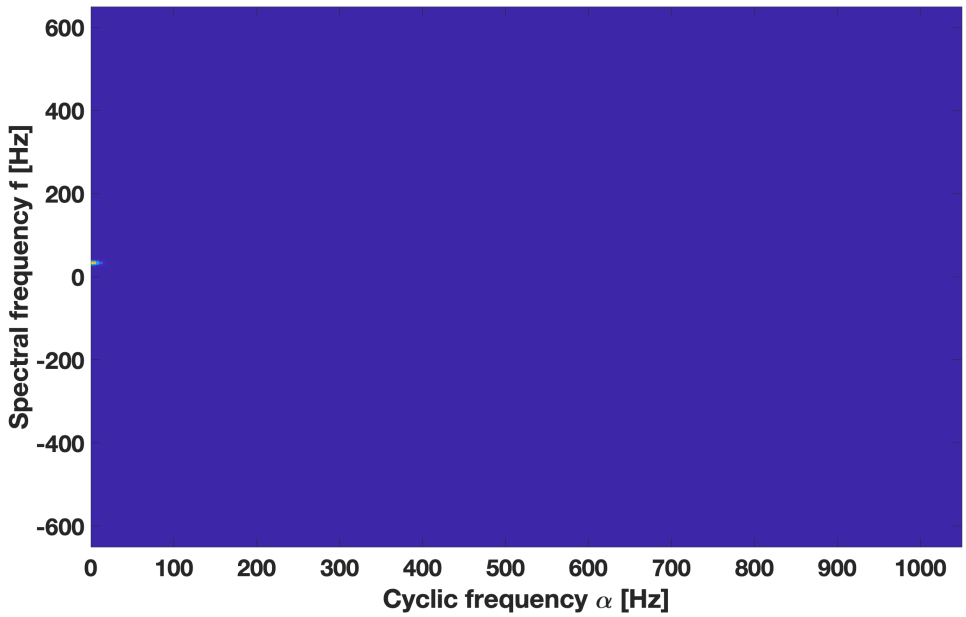


Figure 3.16: Radar signal from a moving target in the CSD

in the CSD plane. Radar return from car wheels also exhibits periodicity in the CSD plane. The typical rotation per minute (rpm) value of a drone propeller is 10,000 rpm. The typical rpm of a car wheel at 160 kph is around 1,400 rpm. So, the drone propeller and the car wheel can be distinguished from each other effortlessly.

### 3.2.1 Peak Detection

As presented in the previous sections, propeller signal genenarates peaks in the CSD plane. In order to perform drone detection and Doppler shift frequency calculation, the peaks in the CSD plane have to be detected. One way to detect these peaks is to use the constrant false alarm rate (CFAR) in CSD. In addition, CFAR image processing algorithms can also be used to detect peaks in the CSD plane. As a general approach in this thesis, CFAR is preferred as the peak detection method. But also in the simulations a simulation is also performed to show the applicability of the image peak detection methods.

CFAR is a well known technique in detection, especially in radar community. In [12] both one dimensional and two dimensional cell averaging CFAR are discussed in detail. The basic structure of one dimensional CFAR is shown in Figure 3.17. The

detection is made for cell under test (CUT). In order to obtain constant false alarm rate, the interference signal around the CUT is measured using the samples in the lagging and leading training cells. G stands for the guard cells that are not included in the interference measurement. $f_{lag}$ is the sum of the signal magnitudes in the lagging window, $f_{lead}$ is the sum of the signals in the leading window, $g$ is the arithmetic logic function. The threshold value T is calculated by multiplying the CFAR constant and the output of the function $g$. The detection decision is made according to this comparison.

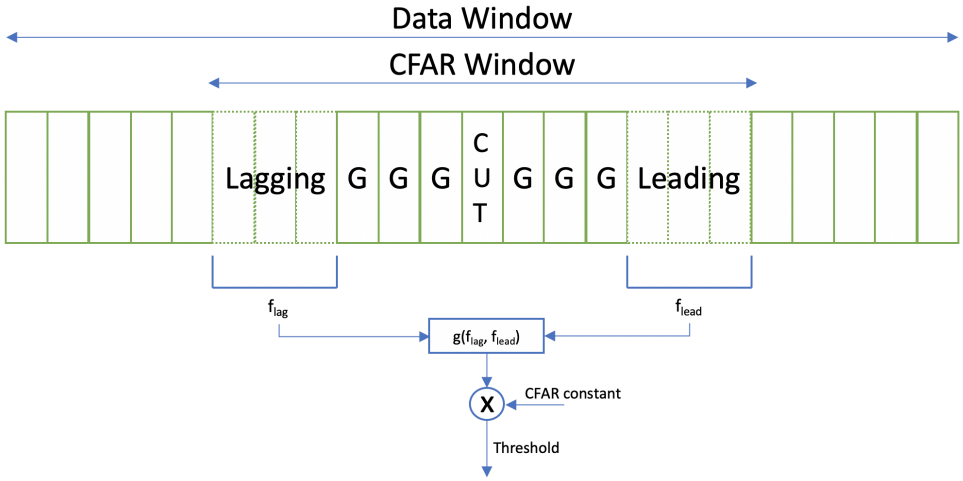


Figure 3.17: One dimensional CFAR

The concept behind two dimensional CFAR is also very similar to one dimensional CFAR. Training cells and guard cells are defined in two dimensions around the CUT. The decision about CUT is made using the signals in the training cells.

The MCSD method uses the peaks in the CSD plane to determine the cyclic frequency $\alpha$ and the spectral frequency $f$. In order to locate the peaks in the CSD plane, we use peak detection algorithm, such as CFAR algorithm, in the CSD plane. Since CSD is a two dimensional data, CFAR algorithm for two dimensional data has to be used. The CFAR algorithm presented in [12] operates on two dimensional data. In Figure 3.19 the CFAR window is shown in the CSD.

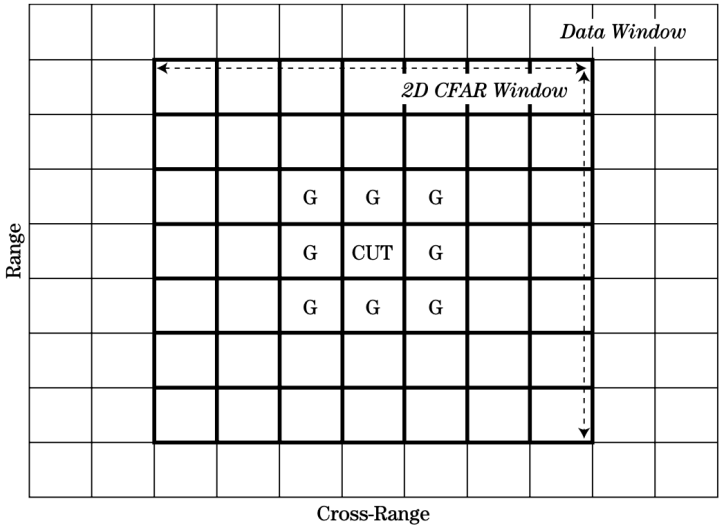


Figure 3.18: Two dimensional CFAR ([12])

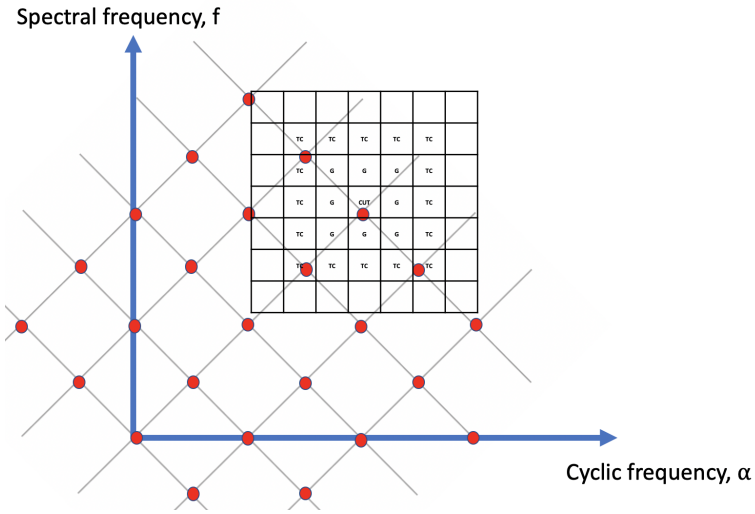


Figure 3.19: Two dimensional CFAR in the CSD

## 3.3 Projection

The output of the peak detection produces the detection results in the CSD plane, in other words, peak detection produces 0's and 1's in the CSD plane. The micro-Doppler signal produces periodic structures in the CSD plane, both on the cyclic frequency and the spectral frequency. In order to use the deinterleaving algorithm, the two dimensional periodic pattern in the CSD plane has to be transformed into one

dimension with the period information. We call this process projection.

In this method, the detections on the spectral frequency axis over the cyclic frequency axes are performed using summation. For each cyclic frequency value, $\alpha$, number of detections over the spectral frequency is determined. After performing this operation for all $\alpha$ values, a one dimensional CFAR is performed over these data. The peaks determined at the output of the CFAR are the $\alpha$ values, which have considerable periodicity over the spectral frequency. The periodicity along the cyclic frequency is determined over these data using the deinterleaving algorithm. The mathematical representation of the projection is presented in equation (3.3), where $F_c$ is the output of the peak detection and $F_p$ is the output of the projection function. A sample sum projection is shown in Figure 3.20. In this figure, red boxes represent the micro-Doppler signal components in the CSD plane, and the black components represent the noise components. The number of detections are summed along the spectral frequency to produce the number of detections for a cyclic frequency $\alpha$.

$$F_p(\alpha) = \sum_k F_c(\alpha, k) \tag{3.3}$$

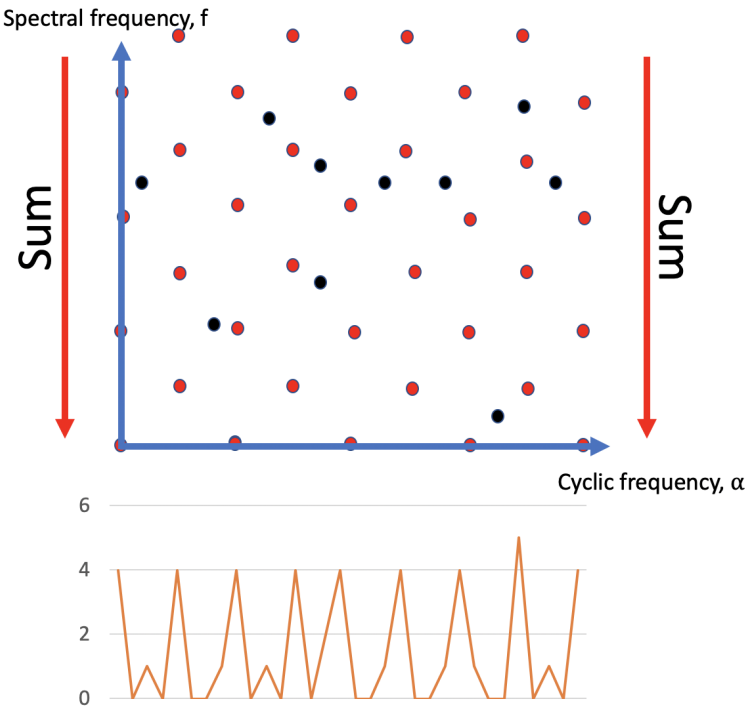


Figure 3.20: Sum projection

## 3.4 Deinterleaving

Electronic Support Measure (ESM) is a main division of electronic warfare (EW). ESM systems are responsible for observing the electromagnetic spectrum for emitter detection and parameter estimation. ESM systems use different types of receivers with instantaneous bandwidth reaching several gigahertz. The receivers catch the signals on air, which are in their instantaneous operating bandwidths. The signals received by the ESM receivers have to be grouped according to their emitters. This grouping process is called deinterleaving. The main motivation for the deinterleaving algorithm is shown in Figure 3.21. Multiple radars transmit multiple pulses into the environment. The pulse repetition period can differ among different radar systems. The ESM system receives all the signals in the environment and groups them according to the source radar system. In Figure 3.21, 3 radar systems transmit pulses into the environment. The pulses are mixed in the environment, and the ESM receiver receives this mixture of pulses. At the end of the deinterleaving process, as seen in the left side of the Figure 3.21 the pulse groups are separated from this mixture.

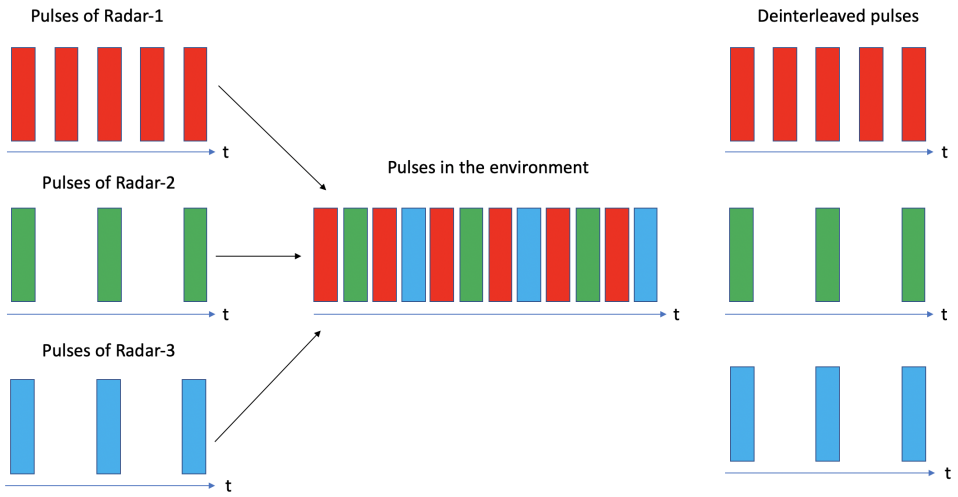


Figure 3.21: Deinterleaving algorithm process

There are multiple parametres of signals that can be used in the deinterleaving process. These are frequency, directional of arrival, pulse repetition interval (PRI), etc. In the literature, there are different algorithms for PRI deinterleaving of pulses ranging from basic histogram techniques to machine learning techniques.

The deinterleaving algorithm in this work is used to determine the main frequency of the periodicity along the cyclic frequency axis of the CSD plane. The projection output is the number of detections with different cyclic frequency values. At integer multiples of the propeller rotation frequency there are peaks along the cyclic frequency. The deinterleaving algorithm is used to detect this periodicity and determine the main frequency. The existence of periodicity on cyclic frequency is used as the propeller present decision. In this work, we opt for histogram based deinterleaving and PRI transform.

### 3.4.1 Histogram Based Deinterleaing

The histogram techniques search for a periodic structure in pulses' time-of-arrival (TOA) values. TOAs of a constant PRI radar form a periodic impulse train in the TOA axis. The presence and main period of this impulse train are determined by the deinterleaving algorithm. The CSD plane in the presence of a propeller echo signal contains periodic impulses along both the spectral and cyclic frequency axes. Dein-

terleaving algorithms can be used in micro-Doppler signal detection in the CSD plane since Micro-Doppler signals cause periodicity in the CSD plane. In [44] Cumulative Difference Histogram (CDIF) deinterleaving method is explained. In this method, $N$ pulses are collected within a specific time interval. The TOA difference between adjacent pulses is calculated and the histogram of difference values is calculated. This is called the first order histogram. Then the TOA difference between each pulse and the next one is calculated. This is called the second order histogram. Then this procedure is repeated for higher order histograms. In Figure 3.22 time difference for first, second and third order histogram generation is shown.

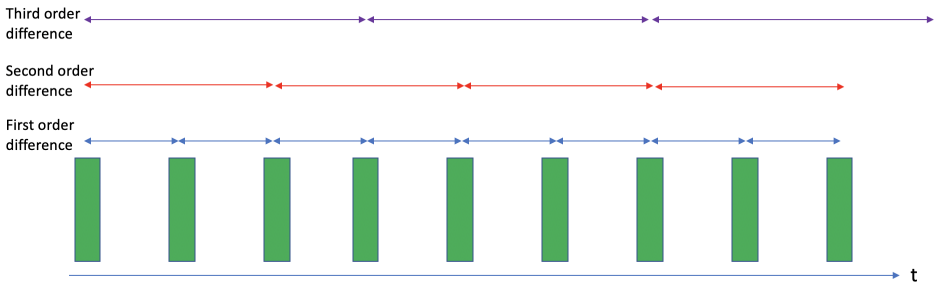


Figure 3.22: Deinterleaving time difference histogram generation

The histogram is compared with a threshold to determine whether there is a periodic sequence related to that order of the histogram or not. The threshold value is given in [44] as

$$T(h_\tau) = h_x(h_E - h_c)\exp\left(\frac{-h_\tau}{h_k h_N}\right) \tag{3.4}$$

where $h_\tau$ is the histogram bin number, $h_E$ is the number of observed pulses, $h_c$ is the histogram order, $h_x$ is a constant less than 1, $h_N$ is the total number of bins in the histogram, $h_k$ is a constant depending on observations.

The aim of deinterleaving in ESM is to find a periodic structure due to radar signal based TOAs. However, in our work we are searching for a periodic structure in the CSD plane, since micro-Doppler signals cause periodicity on the CSD plane. After projecting the CSD plane to one dimension, deinterleaving is used to determine whether there is periodicity in the cyclic spectrum or not. The existence of periodicity means the existence of a micro-Doppler signal source. Also, deinterleaving finds the

period value, which is the rotation period of the propeller.

### 3.4.2 PRI Transform

As seen in the previous subsections, the deinterleaving is the key part to detect the periodicity in the CSD domain. This periodicity implies the presence of rotary wing air platform in the coverage area of the radar systems. Within our scope, the rotary wing air platform refers to a drone system. In order to present an alternative for drone detection in the CSD domain, PRI transform is also used within this study. PRI transform is a new deinterleaving technique compared to histogram based deinterleaving. The main purpose of the PRI transform is to detect periodicity and estimate the period. In [45] PRI transform is discussed in detail. The main interest of PRI transform is to estimate the main frequency of impulse train function. Let us assume this function to be $g(t)$,

$$g(t) = \sum_{n=0}^{N-1} \delta(t - t_n) \tag{3.5}$$

where $t_n$ is the signal present positions. Then, the PRI transform can be written as

$$D(\tau) = \int_{-\infty}^{\infty} g(t)g(t+\tau)e^{j2\pi t\tau}dt \tag{3.6}$$

The Fourier transform of an impulse train is also an impulse train. Therefore, to detect impulse trains and estimate the frequency of the impulse train, Fourier transform cannot be considered as a useful tool. On the other hand, the PRI transform takes in to account harmonic structure of impulse train outputs the presence of the signal and frequency estimate of the signal. Equation (3.6) defines the PRI transform for continuous time. In [45] the discrete PRI transform algorithm is also defined. According to this algorithm, $[\tau_{min}, \tau_{max}]$ is defined as the probable PRI values. This interval is divided into $K_{int}$ intervals. The width of each PRI bin is given in [45] as $b = (\tau_{max} - \tau_{min})/K$. The center of PRI bin is given in equation

$$\tau_k = (k - 1/2)b + tau_{min}, \quad k = 1, 2, ..., K_{int}. \tag{3.7}$$

The PRI bins are as shown in Figure 3.23.

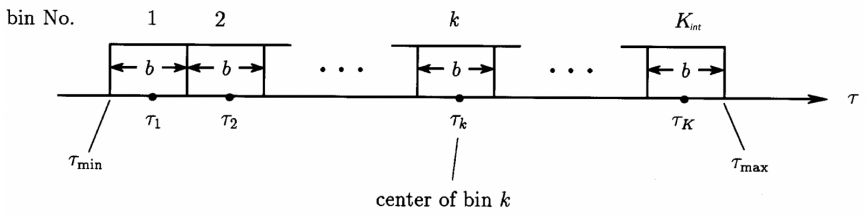


Figure 3.23: PRI bins

Then the discrete PRI transform is given as in equation 3.8.

$$D_k = \sum_{\tau_k - b/2 < t_n - t_m \leq \tau_k + b/2} exp\left[\frac{j2\pi t_n}{t_n - t_m}\right] \tag{3.8}$$

## 3.5 Doppler Calculation

According to equation (2.23), the peaks in the CSD plane are placed as a function of both $f_r$ and $f_d$. The peaks move according to the Doppler frequency, $f_d$, along the spectral frequency axis. $f_d$ can be calculated from the shift of the peak value in the CSD from the nearest $\frac{m+n}{2} f_r$. This fact can be seen in Figure 3.24.

The detection in the CSD of a moving target is shifted along the spectral axis. In order to calculate the Doppler shift, the shifts for all detection in the CSD are averaged. The Doppler shift is calculated in an unambiguous Doppler interval of $[-f_r/2, f_r/2]$. A Doppler calculation window with a width of $f_r$ is used around peaks in the CSD plane. This approach is presented in Figure 3.25.

The mathematical formulation of this method is presented in equation (3.9). $f_p$ is the spectral frequency position of the detections of the peak detection results and $P$ is the total number of detections, $\mathrm{round}$ is the rounding to the nearest integer function. The importance of the parameter $f_p$ in the Doppler calculation is obvious. The reference

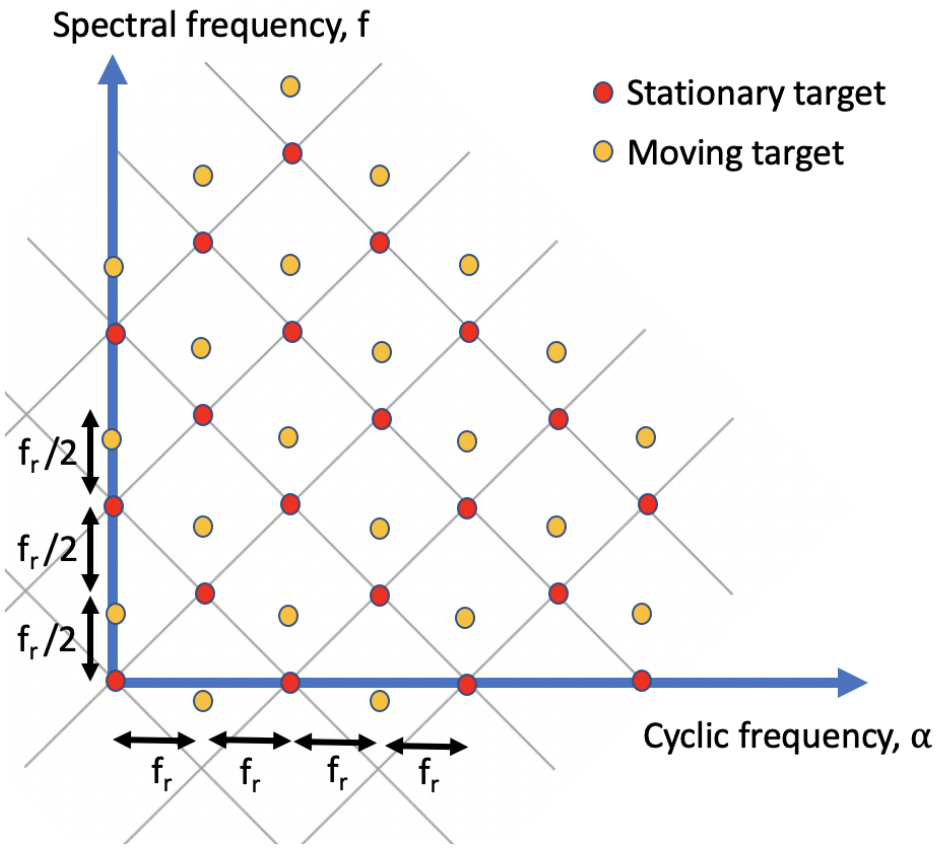


Figure 3.24: Doppler calculation in the CSD plane

point for the Doppler shift calculation is the $f_p$ value.

$$f_d = \frac{1}{P}\sum_{p=1}^{P} f_p - \text{round}(f_p/(f_r/2))(f_r/2) \tag{3.9}$$

An unambiguous Doppler interval of $[-f_r/2, f_r/2]$ has to be investigated with a practical point of view. The assumption about $f_r$ can be based on the 12000 rpm drone propeller rotation frequency, which is equal to 200 Hz. Also, assume that the propellers have 2 blades, so $f_r$ can be assumed to be 400 Hz. For 400 Hz $f_r$ the unambiguous Doppler interval is $[-200, 200]$ Hz. In order to calculate the radial velocity which is in the unambiguous Doppler interval, an assumption for the radar frequency has to be made. In order to obtain high RCS from propellers, 24 GHz of radar operating frequency is assumed. Therefore, the unambiguous radial speed is $[-1.25, 1.25]$ m/s. Although this interval may be useful for many slow moving drones, a method

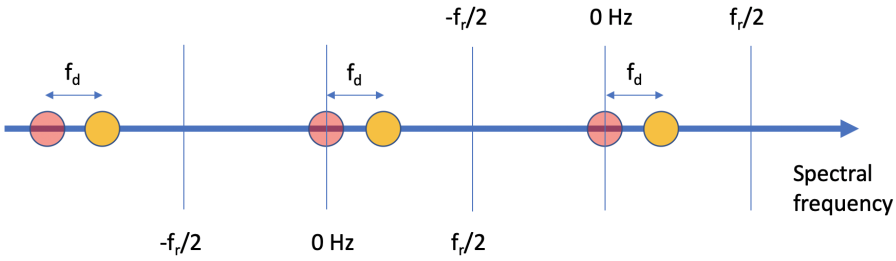


Figure 3.25: Doppler calculation on spectral frequency

for high speed drones is also proposed here.

To solve the Doppler ambiguity drone's body return signal in the spectral frequency domain is used. The real Doppler generated by the drone can be represented as in equation (3.10).

$$f_{doppler} = f_d + mf_r/2 \tag{3.10}$$

In equation (3.10) $f_{doppler}$ is the unambiguous Doppler frequency and $m$ is an integer value. Assume a target closing towards the 24 GHz radar with a radial speed of 3 m/s. This speed will cause 480 Hz Doppler shift. If the propeller rotates at 100 Hz and has two blades, the main cyclic frequency will be 200 Hz. The CSD of this signal is shown in Figure 3.26. The drone body is also present in this simulation result. It is assumed that the drone body has 20 dBsm higher RCS compared to the propeller.

The calculated Doppler frequency using equation (3.9) resulted in 79.2 Hz. Using the equation (3.10) the unambiguous Doppler frequency can be determined in the spectral frequency domain. The signal in the spectral frequency domain is shown in Figure 3.27. There are many peaks in spectral frequency which is caused by the propeller generated micro-Doppler effect. The maximum of the peaks is at 480 Hz which gives the true Doppler shift value.

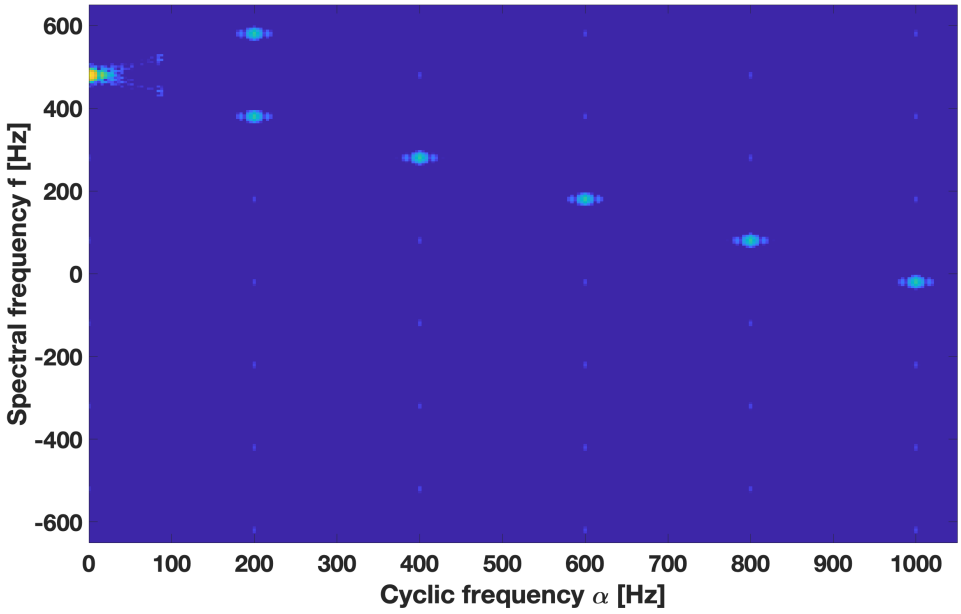


Figure 3.26: Doppler ambigious target CSD

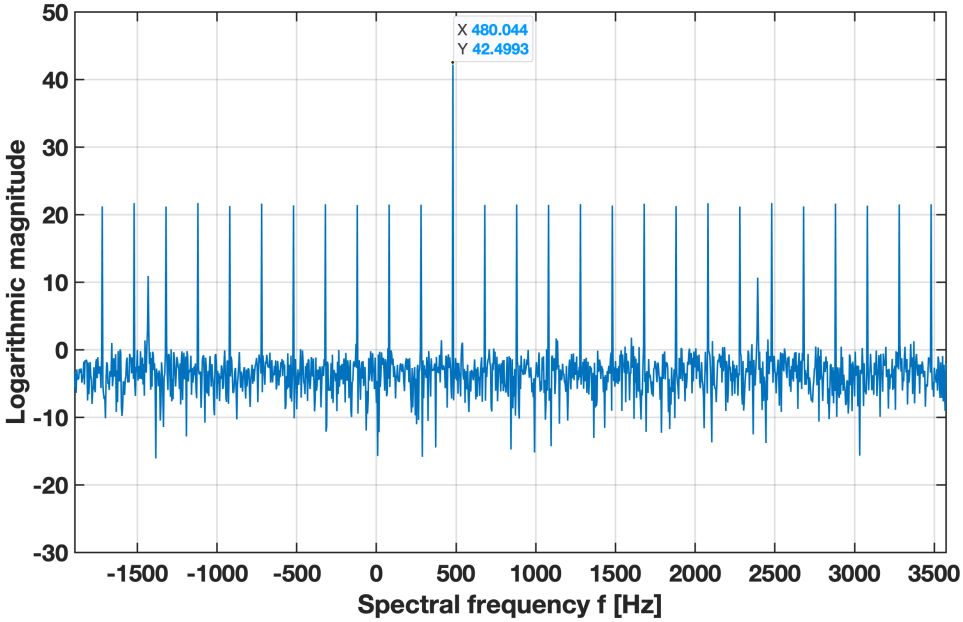


Figure 3.27: Doppler ambigious in the spectral frequency

## 3.6 Localization

Localization using only Doppler frequency information is a well studied field finding applications in the acoustic and radar domains. In [46] the basic approach to target

localization using Doppler frequency is presented. According to this approach, the position and velocity are the values that minimize the cost function in equation (3.11).

$$J(\boldsymbol{p}, \boldsymbol{v}) = \sum_{i=1}^{n} (c f_{di}/f_c - \boldsymbol{v}^T(\boldsymbol{p} - \boldsymbol{s_i})/\|\boldsymbol{p} - \boldsymbol{s_i}\|)^2 \tag{3.11}$$

In equation (3.11) $\boldsymbol{p}$ is the target position vector, $\boldsymbol{v}$ is the target velocity vector, $n$ is the number of sensors, $\boldsymbol{s_i}$ is the position vector of $i^{th}$ sensor, $f_{di}$ is the Doppler frequency measured by $i^{th}$ sensor. This optimization problem can be solved with the grid search for $\boldsymbol{p}$ since in [46] the velocity vector, $\boldsymbol{v}$, is formulated as

$$\boldsymbol{v} = A^{\dagger}\boldsymbol{b} \tag{3.12}$$

where $\boldsymbol{b} = c/f_c[f_{d1}, \ldots, f_{dn}]^T$ and $A = [\psi_1, \ldots, \psi_n]$. The $\psi$'s in $A$ can be written as $\psi_i = \boldsymbol{p} - \boldsymbol{s_i}$.

The method presented in [46] is studied for 2-dimensions and can be extended to 3-dimensions. In [47] Doppler localization is studied in detail in 3-dimensional space. In the presence of multiple targets, Doppler frequency measurements must be associated with true targets. In [48] a data association method for the multiple target case is developed. A similar approach can also be used for the MCSD method herein.

# CHAPTER 4

# PERFORMANCE ANALYSIS

CRLB of positioning accuracy is considered to be one of the performance metric for the MCSD method in this thesis. CRLB of positioning accuracy is studied for both the MCSD method MIMO radar and the monostatic radar. The comparison of these two radar types are presented in the first section. In the second section, MCSD method MIMO radar positioning performance vulnerability to Doppler frequency errors is analyzed.

## 4.1 CRLB Performance Analysis

In this section, the CRLB analysis of the MCSD method is presented to show the effectiveness of the proposed approach and compared to conventional radar. The exact derivation of the CRLB of the MCSD method is shown in Appendix-B.

To make a comparison with a conventional radar system, let us look at the CRLB positioning accuracy of the conventional radar system. In [49] the CRLB for angle measurement is given for a radar system with linear array antenna as in equation (4.1)

$$\sigma_{\text{CRLB}}^{\text{angle}} = \frac{\lambda}{2\pi} \frac{\sqrt{P_a}}{\sqrt{\sum_{p=1}^{P_a} d_p^2}} \frac{1}{\sqrt{2MP_a\text{SNR}}} \tag{4.1}$$

where $\lambda$ is the wavelength, $P_a$ is the number of antenna elements in the array, $d_p$ is the position of the $p^{th}$ antenna, $M$ is the number of samples used, SNR is the signal to noise ratio level at each antenna element output. In [50], the CRLB of range

estimation is calculated for the linear frequency modulation (LFM) waveform as

$$\sigma_{\text{CRLB}}^{\text{angle}} = \sqrt{\frac{3c^2}{8\pi^2 B^2 M P_a \text{SNR}}} \tag{4.2}$$

Monostatic radar outputs range and angle information in polar coordinates. Since the MCSD method is typically applicable in MIMO radar systems, the MCSD method generates position information in cartesian coordinates. To compare the monostatic radar and the MCSD method CRLB, monostatic range and angle information must be converted to cartesian coordinates. Let us define the polar to cartesian coordinate conversion function $f(r, \theta_p)$ as in equation (4.3). The Jacobien of $f(r, \theta_p)$ is in equation (4.4). The covariance matrix in cartesian coordinates, $C_{xy}$, can be written as in equation (4.5) ([51]), where $C_{r\theta_p}$ is the covariance matrix in polar coordinates.

$$f(r, \theta_p) = \begin{bmatrix} x \\ y \end{bmatrix} = \begin{bmatrix} r\sin(\theta_p) \\ r\cos(\theta_p) \end{bmatrix} \tag{4.3}$$

$$G = \begin{bmatrix} \sin(\theta_p), & r\cos(\theta_p) \\ \cos(\theta_p), & -r\sin(\theta_p) \end{bmatrix} \tag{4.4}$$

$$C_{xy} = G C_{r\theta_p} G^T \tag{4.5}$$

In order to compare the performance of the monostatic radar and the MCSD based MIMO radar, let us devise a typical scenario in which there is a linear array monostatic radar with 5 elements. The radar waveform is assumed to be linear frequency modulated with a bandwidth of 5 MHz. The monostatic radar's observation time is 30 ms. The MIMO radar with the MCSD method also uses 30 ms observation duration and a sampling frequency of 44.100 Hz. Although the MCSD method works on micro-Doppler components, in order to constitute a common reference point for performance comparison, the return signal energy from the drone body is considered to be the reference signal.

SNR is defined as the ratio of the signal power to the noise power. Define the received signal energy as $E_s$ and the duration of the signal as $T_s$. Then the signal power is

defined as in equation (4.6).

$$P_s = \frac{E_s}{T_s} \tag{4.6}$$

White noise is distributed throughout the frequency band with a power spectral density of $N_0/2$ Watts/Hz. Assume that the radar system has a bandwidth of $B$ Hz. Then the noise power in a radar system with a bandwidth of $B$ is $N_0 B$, due to the symmetry in negative and positive frequencies. Then, the SNR can be written as in equation (4.7).

$$SNR = \frac{E_s}{T_s N_0 B} \tag{4.7}$$

The SNR defined in equation (4.7) depends on the system bandwidth. Within this study, received signal energy at each antenna element is used for both MIMO and monostatic radars. The monostatic radar is assumed to have a bandwidth of 5 MHz. The MIMO radar bandwidth is assumed to be 20 KHz. Taking into account this difference, the MIMO radar will have a 23.97 dB lower noise level compared to the monostatic radar. So, for equal signal energies and durations, the MIMO radar will have 23.97 dB better SNR value. To make a fair comparison of the monostatic and MIMO radars, $E_s/N_0$ is used instead of SNR in this thesis.

As derived in Appendix-B, CRLB performance of the MCSD method depends on both radars' and drone's positions and velocities. In order to show the CRLB performance of the MCSD method, the scenario in Figure 4.1 is used. Since the CRLB performance of the MCSD based MIMO radar depends on drone's position, different drone positions have to be taken into account in order to obtain a fair performance comparison. CRLB performance for both the MCSD based MIMO radar and the monostatic radar are calculated over the dotted region in Figure 4.1 and the average of the obtained CRLB values is used as the performance results. Although there are six radars in the scenario, it is assumed that the dotted region is in the coverage of five radars. In the comparisons, the drone is assumed to be hypothetical and has only one propeller with two blades. The propeller is assumed to rotate at a rate of 12000 rpm, which is 100 Hz. The length of each blade is assumed to be 10 cm.

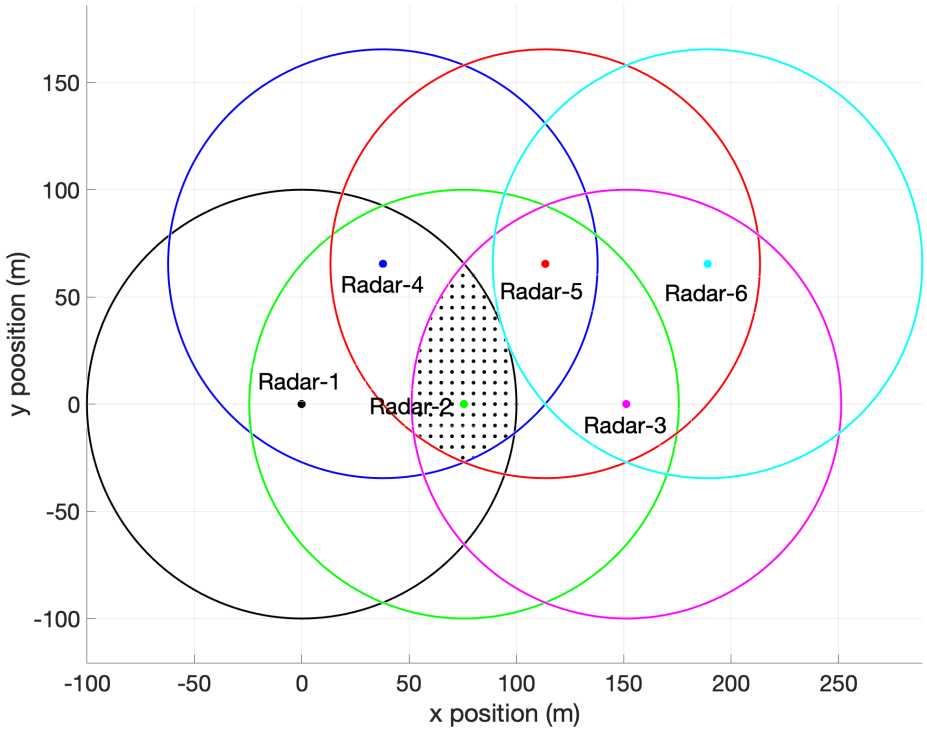


Figure 4.1: Scenario for the simulations

Monostatic radar detects objects based on fuselage and propeller RCS but the MCSD based MIMO radar detects micro-Doppler components generated by drone propellers. However, if the MIMO radar works using fuselage return only it can detect objects but cannot discriminate drones. A monostatic radar can be made to work using micro-Doppler components, in which case it can discriminate drones. Taking into account this fact, the effect of the RCS difference explained in Section 2.4 is taken into account assuming a 20 dB RCS difference.

The CRLB comparison results are shown in Figure 4.2. For these results the time on target durations for both MIMO radar and the monostatic radar is assumed to be 30 ms. This time on target value can be considered as a typical value for a monostatic radar. But the proposed MIMO radar illuminates the target all the time since it is not scanning space. Assume that the MIMO radar collects 250 ms data and processes it. So for MIMO radar, the time on target is 250 ms. The time on target value difference makes significant difference between the MIMO radar and the monostatic radar in terms of CRLB. Although the total energy level is same as the 30 ms case, the observation duration affects the localization performance considerably. The results are

presented in Figure 4.3.

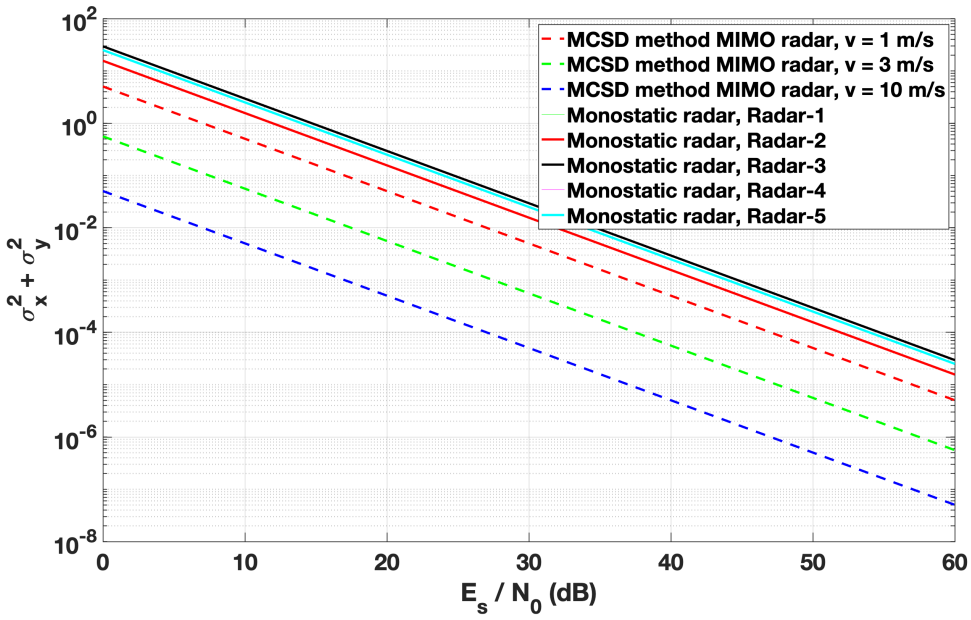


Figure 4.2: CRLB comparison of the prosed system solution and conventional monostatic radar for the same energy

One of the important parameters to be estimated using the MCSD method is $f_r$. The CRLB for $f_r$ is shown in Figure 4.4. The performance is calculated for MIMO radar considering the in band SNR values.

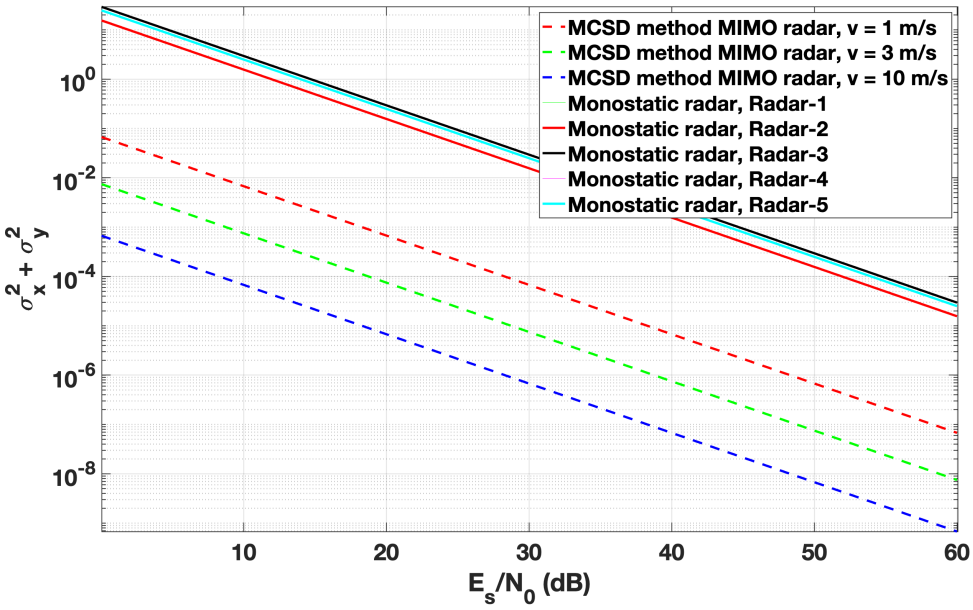


Figure 4.3: CRLB comparison of the prosed system solution and conventional monostatic radar for same energy, different time on target

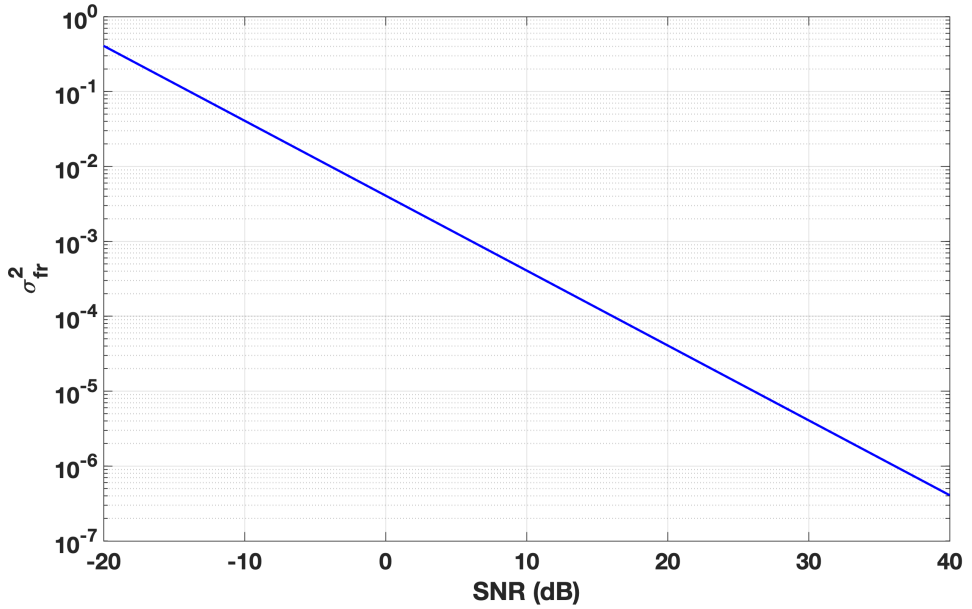


Figure 4.4: CRLB of $f_r$

## 4.2 Frequency Noise Effect on Localization Performance

The MCSD method relies on Doppler frequency measurements in the localization step. The effect of Doppler frequency accuracy on the localization performance of the Doppler-only localization method is discussed in [46]. Although the results presented in [46] show that the position error can be considered as acceptable, the scenario is different from the scenario used in this thesis. To evaluate the Doppler frequency noise effect on the MCSD method, the scenario shown in Figure 4.1 is used. The sensors are assumed to operate at 24 GHz. The simulations are performed for the drone position which is assumed to be on the dotted positions in the scenario. The results are shown in Figure 4.5. The results show that the localization error can be considered to be within acceptable limits. The error increases as the speed of the drone decreases. Since the frequency measurement process basically measures frequencies at discrete values, the localization error caused by this discretization is evaluated as acceptable according to the results shown in Figure 4.5.

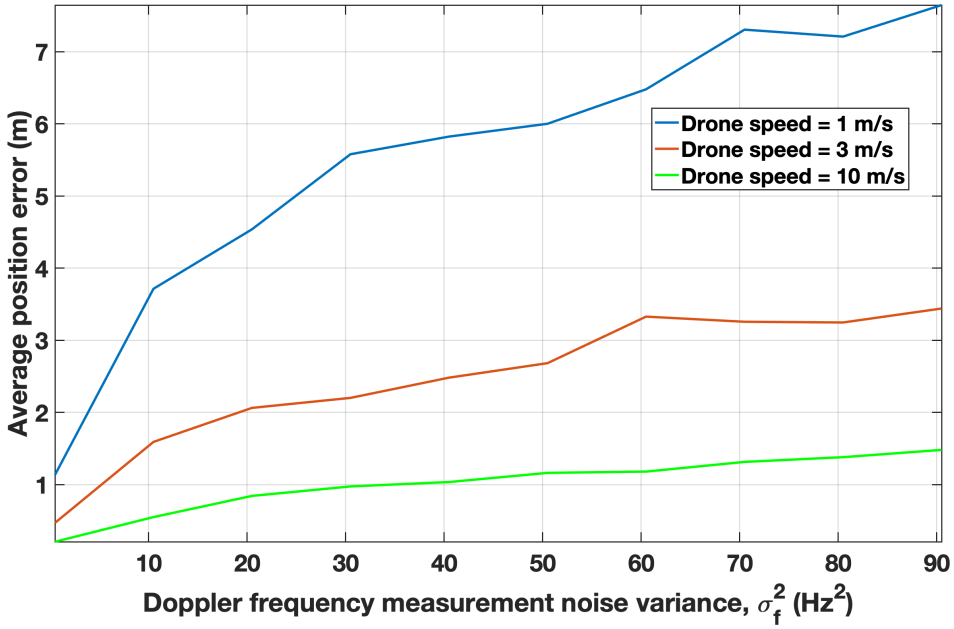


Figure 4.5: The effect of Doppler frequency noise on the localization performance

# CHAPTER 5

# COST ANALYSIS

One of the motivations of this thesis is to propose a drone sensing system which is simple and low cost. The analysis of the MCSD method MIMO radar system is defined in this chapter. In the first section the cost upper limit for each sensor is derived. In the second section, in addition to coverage area, time is also considered as a factor affecting the cost, and the cost upper limits are determined using the time information.

## 5.1 Cost

Drone detection systems used in urban environments face a serious coverage problem. For example, in the presence of tall buildings, the coverage of a conventional radar system is severely reduced. This fact is stated in [25] and a solution with small radar sensors is advised but a clear system solution is not proposed. Besides coverage, a distributed radar system with low power sensors can also be cost effective compared to a traditional high power monostatic radar system. Cost is considered to be a limiting factor for radars for drone detection in [52]. In order to compare the cost of monostatic radar and MCSD based MIMO radar system, the number of small MCSD based MIMO radar sensors to cover an area covered by a monostatic radar has to be found. Since the localization in this thesis is based on Doppler-Only localization, Doppler frequencies from at least 5 different transmit-receive pairs must be measured. Finding the required number of transmitters and receivers turns into a k-Coverage problem. k-Coverage problem is concerned with placing sensors in a sensor network such that any point in the area of interest is covered by k sensors.

Table 5.1: Optimal deployment pattern of sensors for k-coverage (the optimal patterns are shown by boldface font)

| k | Square | Triangle | Hexagonal |
|---|---|---|---|
| 1 | $\sqrt{2}r$ | $\mathbf{\sqrt{3}r}$ | $r$ |
| 2 | $r$ | $r$ | $\mathbf{r}$ |
| 3 | $\frac{2}{\sqrt{5}}r$ | $\mathbf{r}$ | $\frac{2}{\sqrt{7}}r$ |
| 4 | $\mathbf{\frac{3\sqrt{2}}{5}r}$ | $\frac{\sqrt{3}}{2}r$ | $\frac{5}{7}r$ |
| 5 | $\sqrt{\frac{2}{5}}r$ | $\mathbf{\frac{2}{\sqrt{7}}r}$ | $\frac{1}{\sqrt{3}}r$ |
| 6 | $\sqrt{\frac{2}{5}}r$ | $\mathbf{\frac{5}{7}r}$ | $\frac{1}{\sqrt{3}}r$ |
| 7 | $\mathbf{\sqrt{\frac{2}{5}}r}$ | $\frac{2}{3}r$ | $\frac{1}{2}r$ |
| 8 | $\mathbf{\frac{3}{5}r}$ | $\frac{1}{\sqrt{3}}r$ | $\frac{1}{2}r$ |
| 9 | $\frac{2}{\sqrt{17}}r$ | $\frac{1}{\sqrt{3}}r$ | $\mathbf{\sqrt{\frac{3}{13}}r}$ |

In [13] the optimal sensor deployment patterns and the distance between each sensor for k-coverage problem are developed for different $k$ values, which are shown in Table 5.1 where the optimal placement for $k$ values is written in bold font. The parameter $r$ in Table 5.1 represents the range of individual sensors. According to the study in [13] there are three deployment types. These are square, triangle, and hexagonal and are shown in Figure 5.1-5.3. $d^*$ is the distance to the closest neighbors of a sensor.

In order to reduce system complexity, let us assume that each sensor receives its own signal. Since Doppler-Only localization needs 5 different transmit and receive pairs, the K-coverage is considered for $k = 5$ for this case. According to Table 5.1, triangle deployment shall be used for $k = 5$. The distance between each sensor is $\frac{2}{\sqrt{7}}r$.

The sensor densities for triangular, square, and hexagonal deployments have been calculated in [53]. This sensor density for triangular deployment is found to be

$$\lambda_{tri} = \frac{2}{\sqrt{3}X_c^2} \tag{5.1}$$

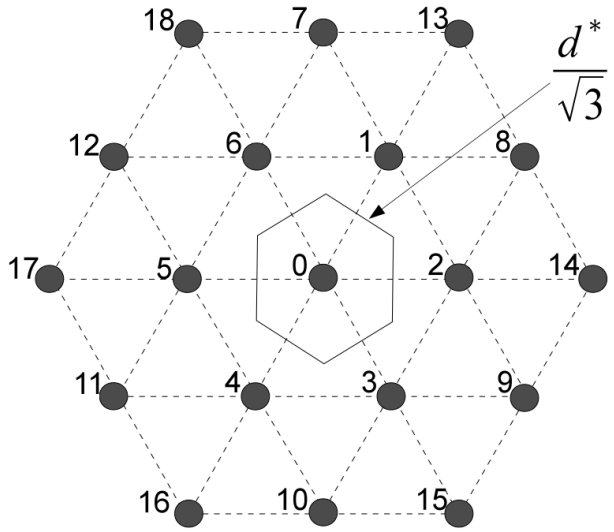


Figure 5.1: Triangular deployment ([13])

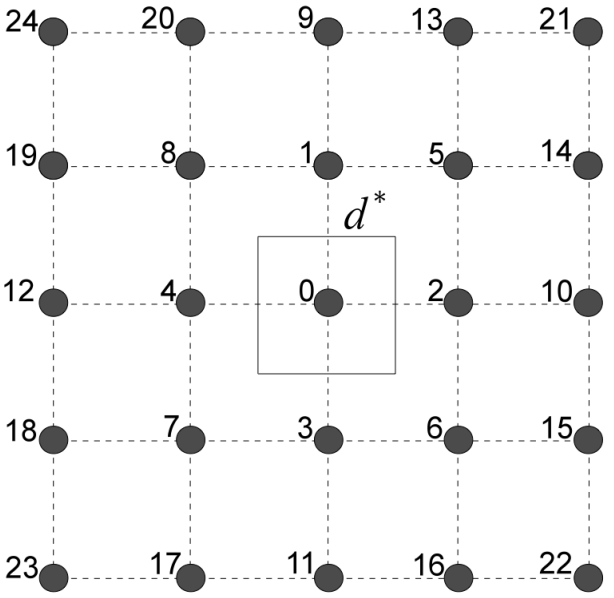


Figure 5.2: Rectangular deployment ([13])

where $X_c$ is the distance between each sensor.

The cost per unit area can be calculated by multiplying equation (5.1) by the unit sensor cost, $C_{\text{unit}}$. Using Table 5.1, cost per unit area can be written as in equation

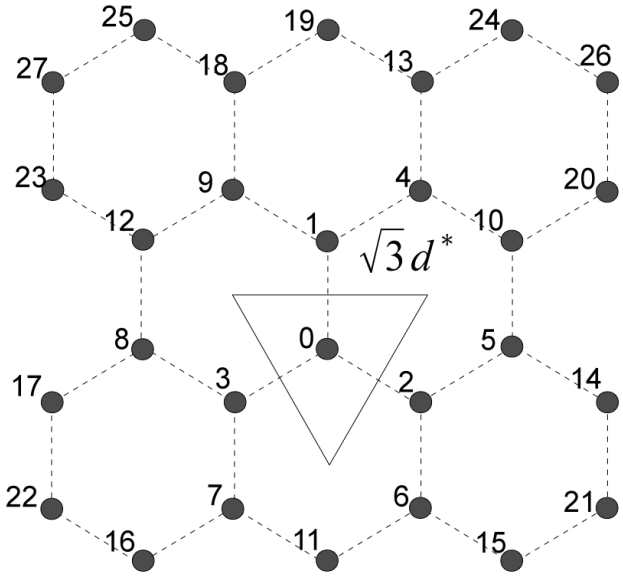


Figure 5.3: Hexagonal deployment ([13])

(5.2) for $K = 5$.

$$C_{\text{area}_5} = C_{\text{unit}} \frac{7}{2\sqrt{3}r^2} \tag{5.2}$$

Equation (5.2) is given so that each sensor works in a monostatic fashion. To count the effect of the bistatic working principle, the sensors must be placed for $K = 3$. This $K$ value guarantees 6 transmit-receive pairs. Therefore, for this case, the cost per unit area can be written as in equation (5.3).

$$C_{\text{area}_3} = C_{\text{unit}} \frac{2}{\sqrt{3}r^2} \tag{5.3}$$

A cost upper limit for a unit sensor can be calculated using the cost of a monostatic radar system as a reference. In equation (5.4) and equation (5.5), the unit sensor cost for $K = 3$ and $K = 5$ is shown, respectively. In these equations $C_{\text{m}}$ is the cost of the monostatic radar, $r$ is the unit sensor range, $R_{\text{m}}$ is the maximum range of the monostatic radar, $\sigma_{\text{diff}}$ is the RCS difference between the drone and the rotor blades,

$\theta_r$ is the azimuth coverage angle in radians.

$$C_{\text{unit}} \leq C_{\text{m}} \frac{\sqrt{3} r^2}{\sqrt{\sigma_{\text{diff}}} R_m^2 \theta_r} \tag{5.4}$$

$$C_{\text{unit}} \leq C_{\text{m}} \frac{4\sqrt{3} r^2}{7\sqrt{\sigma_{\text{diff}}} R_m^2 \theta_r} \tag{5.5}$$

To make a numerical comparison, the cost of a commercially available drone radar system, SIMRAD 4G, is used as a reference since its price information is publicly available. SIMRAD 4G radar system is used to detect drones in [54] and a maximum detection range of 400 meters is obtained for a multirotor drone. SIMRAD 4G is available at a price of 2000 dollars.


Figure 5.4: Simrad radar system

In Figure 5.5 the upper cost limit for a unit sensor of the MCSD based MIMO radar is presented for monostatic ($K = 5$) operation and bistatic ($K = 3$) operation and for all cases $\sigma_{\text{diff}}$ value is assumed to be 20 dB. If the cost of a unit sensor is below the lines presented in the figure, the cost of the MIMO radar system is lower than that of the reference monostatic radar system. For example, the point marked with a red X in the figure shows a 150 m range sensor with a \$125 price tag. This means that if this sensor is used for the MCSD method, it will be cheaper than the reference monostatic

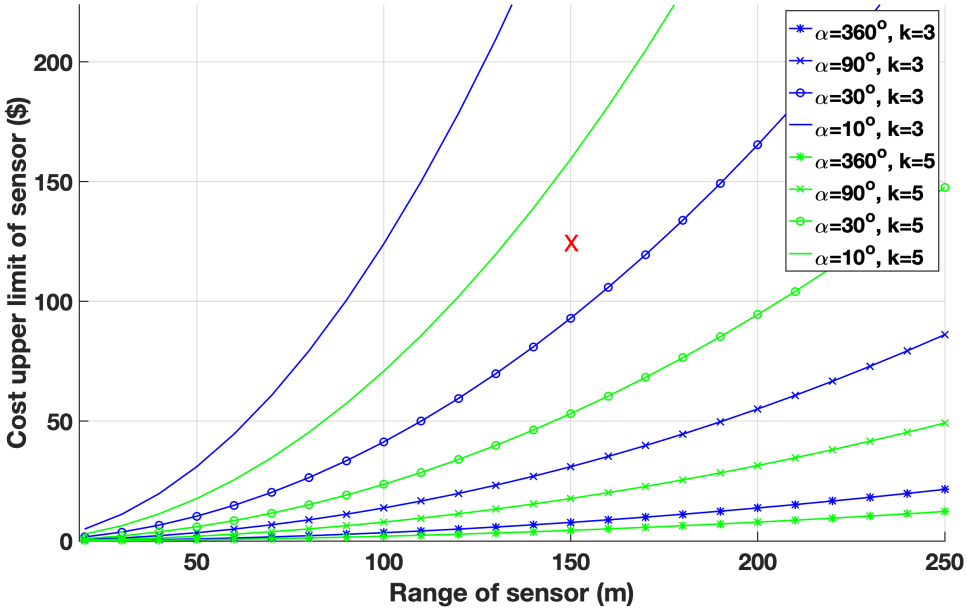


Figure 5.5: Cost upper limit for sensor

radar system for the 5-sensor $10^o$ configuration and 3-sensor $10^o$ configuration; but it will be more expensive than the reference monostatic radar system for the other configurations. The graphs are presented for different coverage angles. As can be seen in the figure, as the coverage angle decreases, the cost upper limit increases. A wide coverage area limits the cost to a tighter region. This fact shows that especially for coverage limited regions, the MCSD based system solution outperforms typical single monostatic radar in terms of cost. Since bi-static radars need synchronization of local oscillators of transmitters and receivers, it is better to use monostatic configuration , $k = 5$, for simplicity of the system.

## 5.2 Effect of Time on Target on Cost

In the previous section, the cost upper limit for a MIMO sensor is formulated considering the total coverage area of MIMO radar and monostatic radar. Besides total coverage area, instantaneous coverage area can also be considered as an important factor on cost upper limit. In a general sense, monostatic radars have narrow antenna beamwidths compared to their total coverage angle. In order to cover the total cov-

erage area, monostatic radars scan the total coverage area in time with steering their antennas. So a monostatic radar sees a target in a limited time, which is called time on target (ToT). Unlike monostatic radar, the MIMO radar system proposed in this thesis uses omnidirectional antennas, so the total coverage area is observed all the time while operating. Since our cost upper limit calculation is based on coverage area, the instantaneous coverage effect can be taken into account.

ToT value for the monostatic radar can be defined as in equation (5.6). In this equation $ToT$ is ToT, $Bw$ is the antenna 3 dB beamwidth of the monostatic radar in degrees, $ASP$ is the antenna scan period of the monostatic radar. The monostatic radar's total azimuth coverage is assumed to be $360^o$.

$$ToT = \frac{Bw}{360} ASP \tag{5.6}$$

Let us define $R_{ill}$ to be the ratio of the illumination time of target to the total time. So $R_{ill}$ can be written as in equation (5.7).

$$R_{ill} = \frac{ToT}{ASP} = \frac{Bw}{360} \tag{5.7}$$

$R_{ill}$ is 1 for the MIMO radar as it does not scan the coverage area due to the omnidirectional antennas. Therefore, we can rewrite equation (5.4) and equation (5.5) taking into account $R_{ill}$.

$$C_{\text{unit}} \leq C_{\text{m}} \frac{\sqrt{3} r^2}{\sqrt{\sigma_{\text{diff}}} R_m^2 \theta_r R_{ill}} \tag{5.8}$$

$$C_{\text{unit}} \leq C_{\text{m}} \frac{4\sqrt{3} r^2}{7\sqrt{\sigma_{\text{diff}}} R_m^2 \theta_r R_{ill}} \tag{5.9}$$

If a MIMO sensor is cheaper than the upper limits in equation (5.8) for bistatic operation or equation (5.9) for monostatic operation than the MIMO radar structure is more cost efficient compared to a monostatic radar in terms of coverage area per unit time. As an example, SIMRAD 4G radar has a beamwidth of $5.2^o$ and $1.25$ seconds

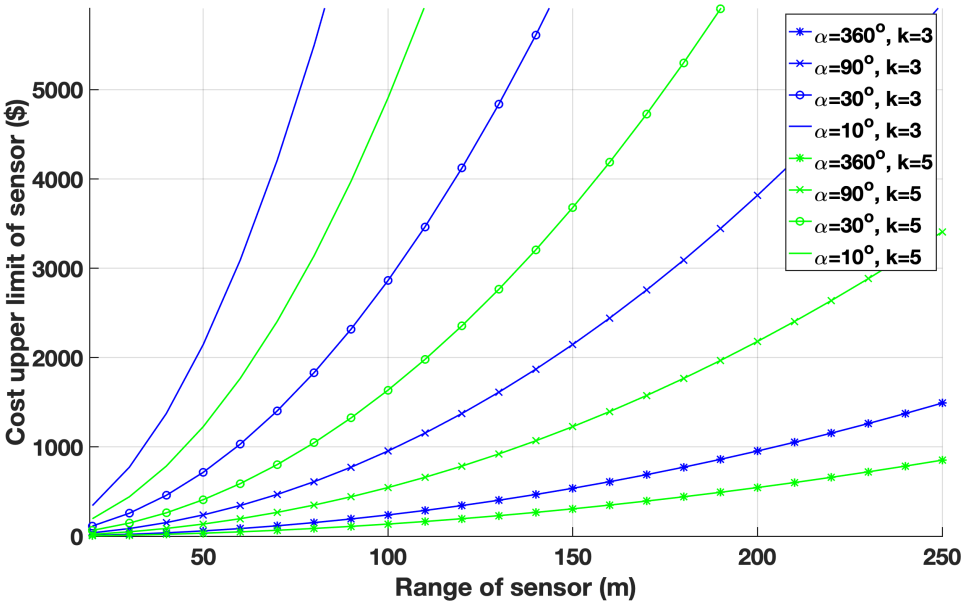


Figure 5.6: Cost upper limit for sensor considering ToT

ASP. So the $R_{ill}$ value of SIMRAD 4G is $0.014$. Comparing Figure 5.5 and Figure 5.6, the strong effect of ToT on cost upper limit is readily seen.

The results in Figure 5.6 can be considered to be the extreme case. The ToT that is required by radars to detect and localize targets, especially in urban areas, is an interesting research topic. The coverage area limitations in urban areas must be considered in ToT calculation of monostatic radars. Higher ToT values are probably needed in limited coverage areas.

# CHAPTER 6

# SIMULATION AND EXPERIMENTAL RESULTS

In this chapter, both the simulation and experimental results for the MCSD method are presented. CSD analysis, $f_r$ estimation with the deinterleaving algorithm, Doppler frequency estimation is shown with both simulation and experiment, while localization is shown through only simulations.

## 6.1 Simulation Results

In this section the simulation results of the MCSD method are presented. The simulations include single propeller, multi-propeller, propeller and drone body, and propeller and moving object cases. Detailed information about simulations are given in related subsections.

### 6.1.1 Single Propeller

For the simulation results in this part, the radar placement in Figure 4.1 is used. There is no specific location of the drone in Figure 4.1. The scenario presented in Figure 6.1 is used for the simulation results.

The propeller in this scenario has one blade for simplicity. It rotates at a rate of 100 Hz. The radar frequency is assumed to be 5 GHz. To present the CSD, CFAR and deinterleaving results, the signals received by Radar-1 are shown in Figures 6.2-6.5. The signal is simulated for an SNR value of 20 dB and for a 250 ms duration. In Figure 6.2 the CSD of the simulated signal is presented, and the results coincide with the theory presented in Chapter 2. There is periodicity in both the cyclic frequency

and spectral frequency domains. There are peaks at integer multiples of $f_r$ in the cyclic frequency domain and peaks at integer multiples of $f_r$ in the spectral frequency domain.

The shift along the spectral frequency axis is obvious. This is caused by the Doppler shift, which is expected to be -31.6 Hz. 2-Dimensional CFAR is performed on these CSD data for $10^{-6}$ probability of false alarm. The result is presented in Figure 6.3. In this figure, the detections at the cyclic frequencies and related spectral frequencies can be seen. Also, at some points, there are false alarms. In order to estimate the cyclic frequency, Histogram based deinterleaving algorithm is used. The histograms of the number of detections for cyclic frequencies are shown in Figure 6.4. The maximum order of the histogram is 3. There is only one peak, 100 Hz, which is over the threshold in the first order histogram. Then the estimation algorithm checks whether there are integer multiples of this value in the higher order histograms. The second and third order histograms include peaks integer multiples of 100 Hz. Since there is a cyclic frequency value whose harmonics are also present in the higher order histograms, it can be concluded that there is a micro-Doppler signal and the cyclic

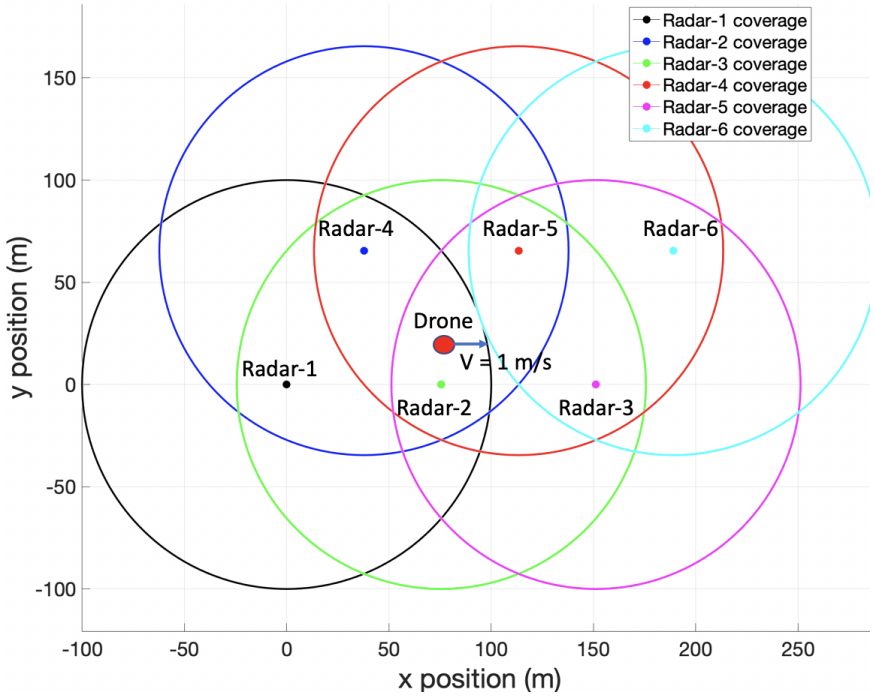


Figure 6.1: Scenario for the simulation results

frequency of the micro-Doppler signal is the frequency detected in the histograms. For this simulation, the cyclic frequency of the micro-Doppler signal is estimated to be 100 Hz. The other deinterleaving algorithm studied in this thesis is the PRI transform, and the result of the PRI transform on the Radar-1 signal is shown in 6.5.

The CSD, CFAR, and PRI transform results for Radar-2, Radar-3, Radar-4, and Radar-5 are presented in Figures 6.6-6.17.

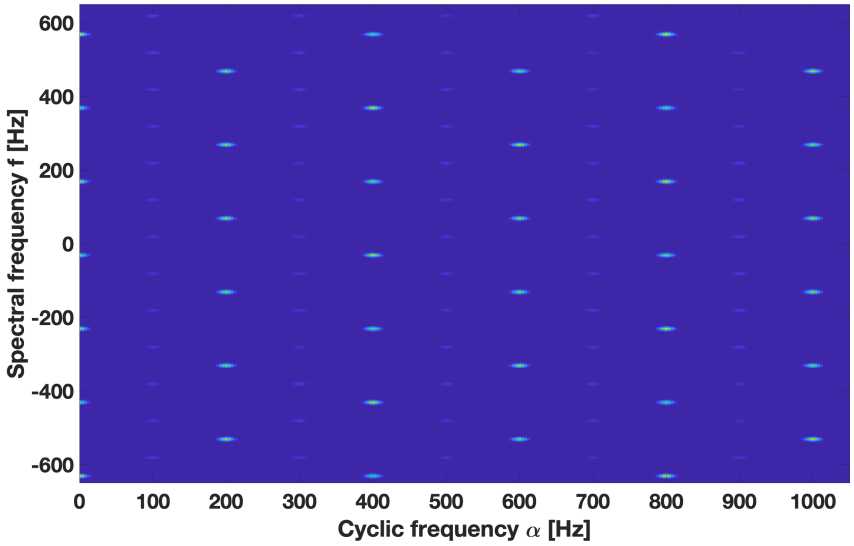


Figure 6.2: CSD of the Radar-1 signal

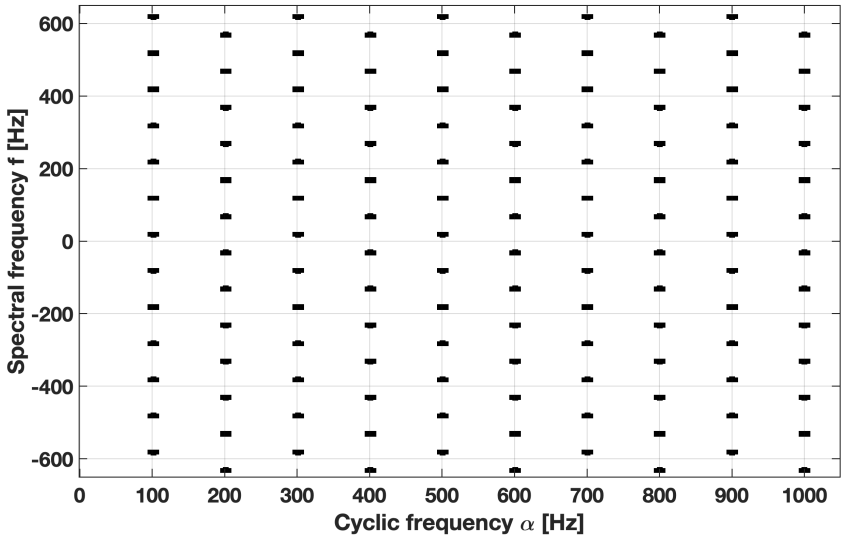


Figure 6.3: CFAR detections in the CSD for the Radar-1 signal

The estimated cyclic frequency is used to calculate the Doppler shift of the signal. For

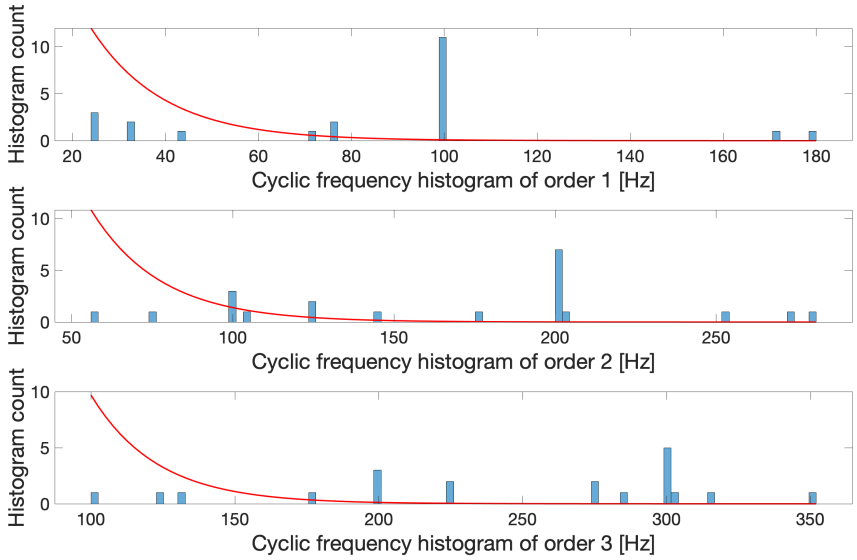


Figure 6.4: Histogram based deinterleaving results for the Radar-1 signal

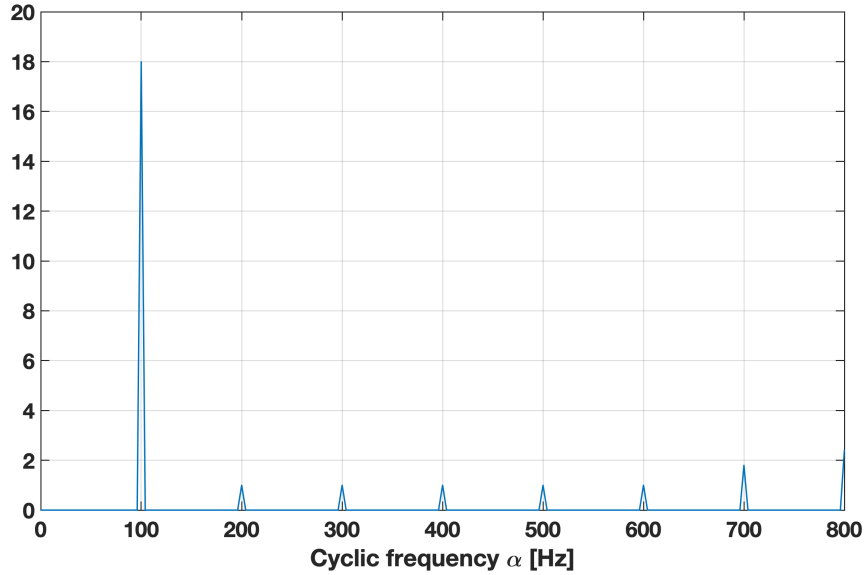


Figure 6.5: PRI transform results for the Radar-1 signal

the simulation scenario presented in Figure 6.1 there are five estimated Doppler frequencies. Doppler frequency estimation is performed using the method presented in Section 3.5. The true and estimated Doppler frequency shift values are shown in Table 6.1. These values are used as presented in Section 3.6 to locate the micro-Doppler echo source. In Figure 6.18, the grid search result for localization is presented. The minimum is placed at (75, 25) m which is the location of the drone in the scenario.

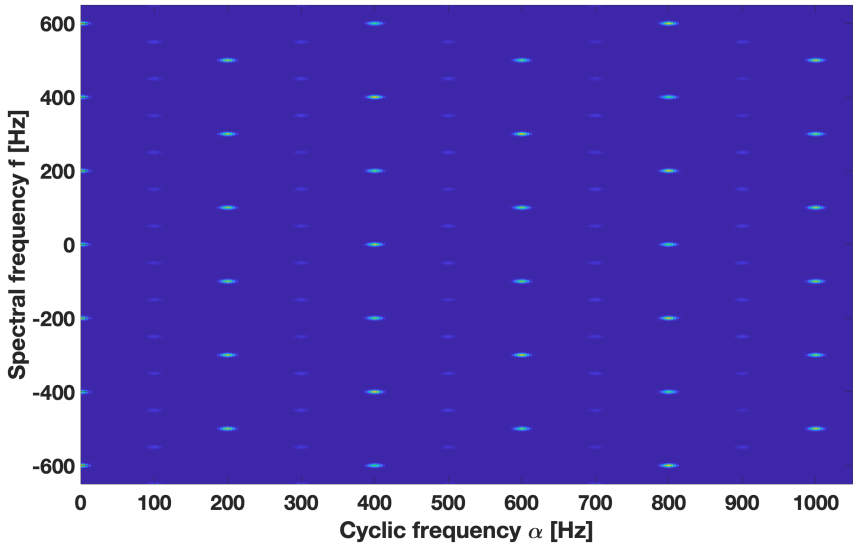


Figure 6.6: CSD of the Radar-2 signal

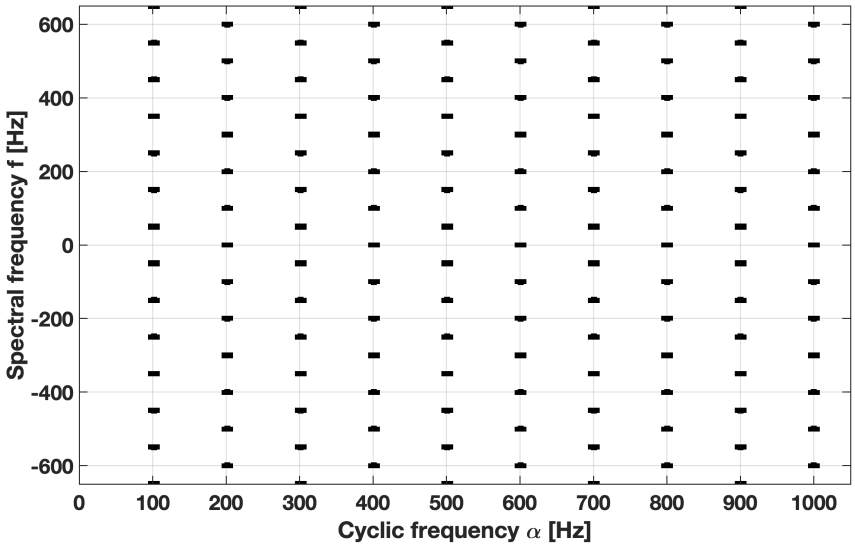


Figure 6.7: CFAR detections in the CSD for the Radar-2 signal

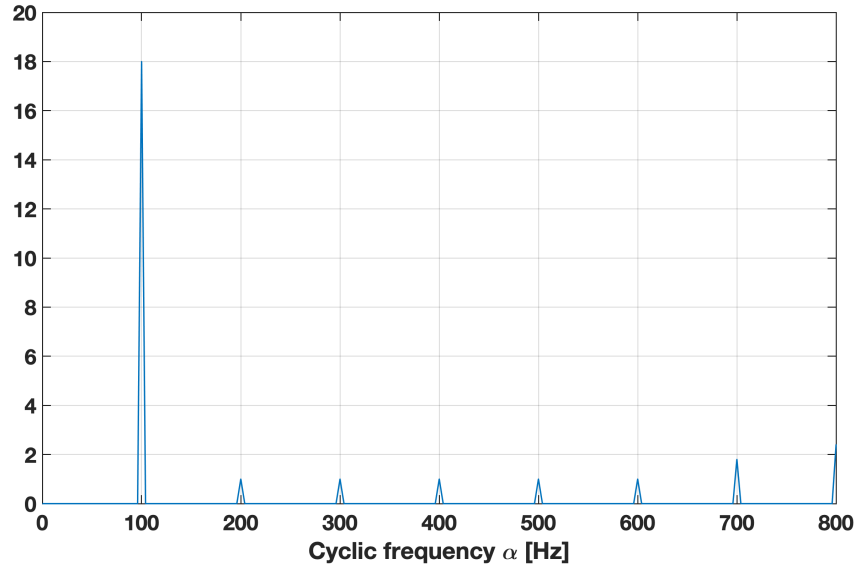


Figure 6.8: PRI transform results for the Radar-2 signal

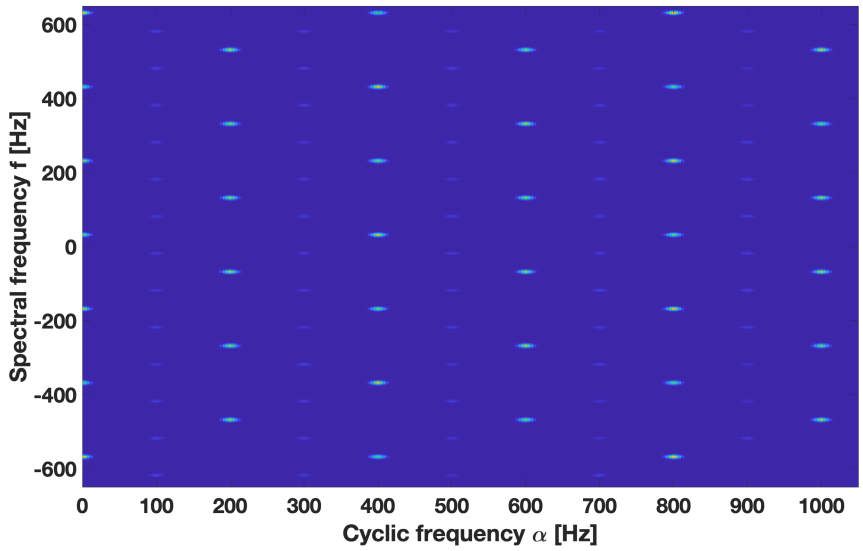


Figure 6.9: CSD of the Radar-3 signal

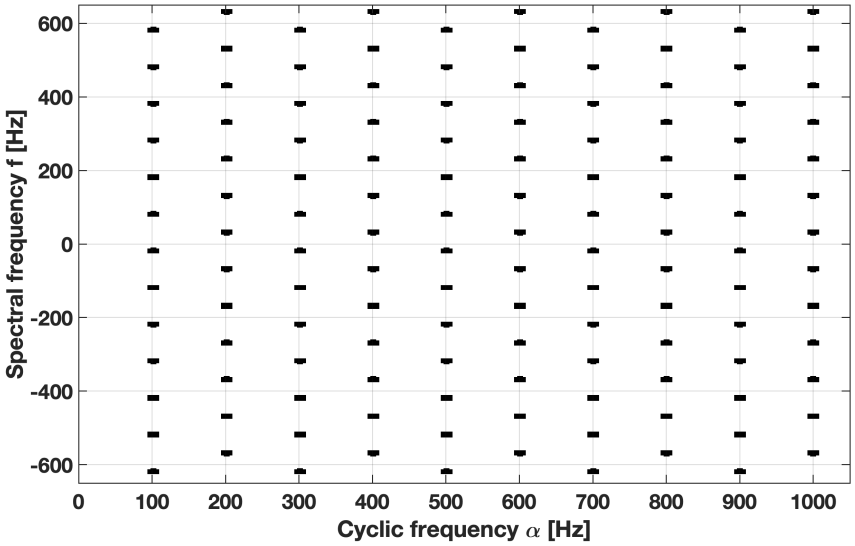


Figure 6.10: CFAR detections in the CSD for the Radar-3 signal

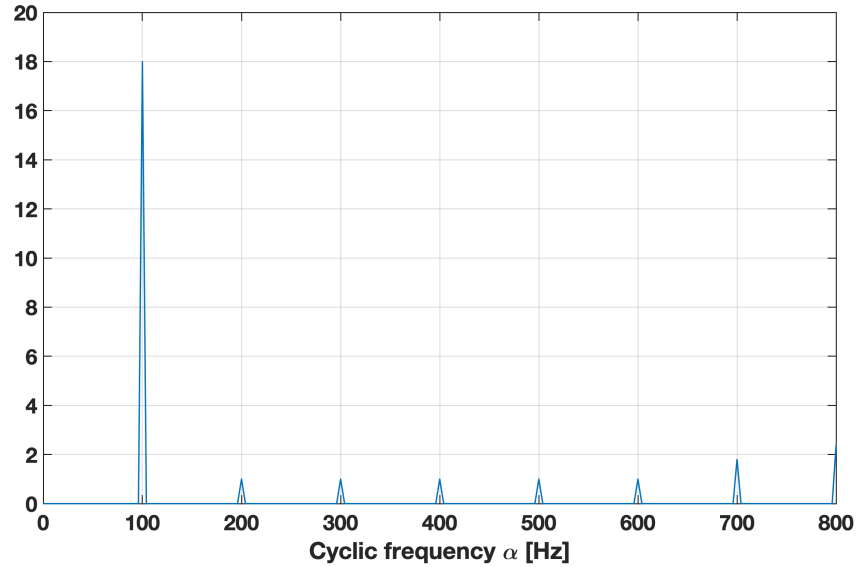


Figure 6.11: PRI transform results for the Radar-3 signal

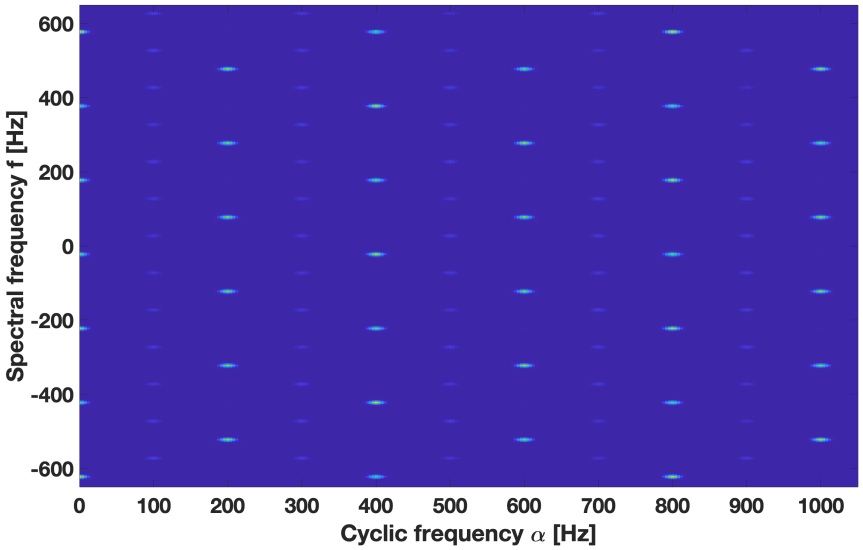


Figure 6.12: CSD of the Radar-4 signal

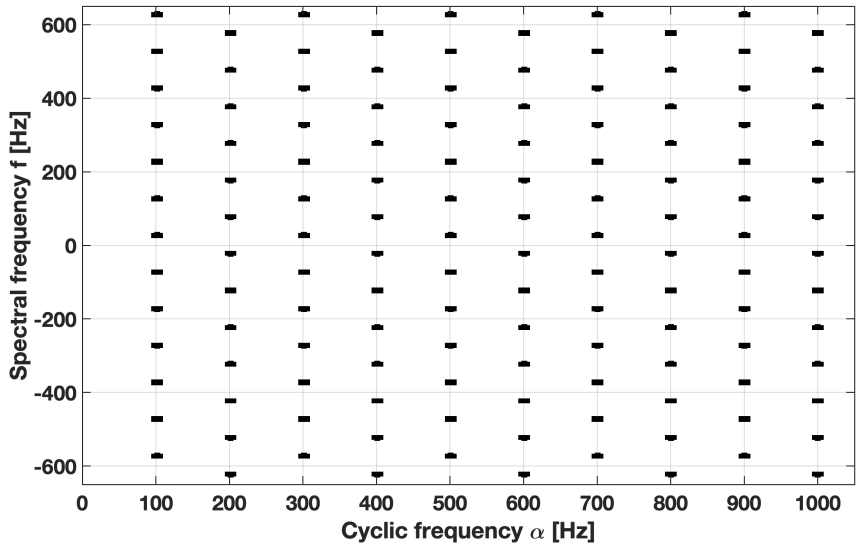


Figure 6.13: CFAR detections in the CSD for the Radar-4 signal

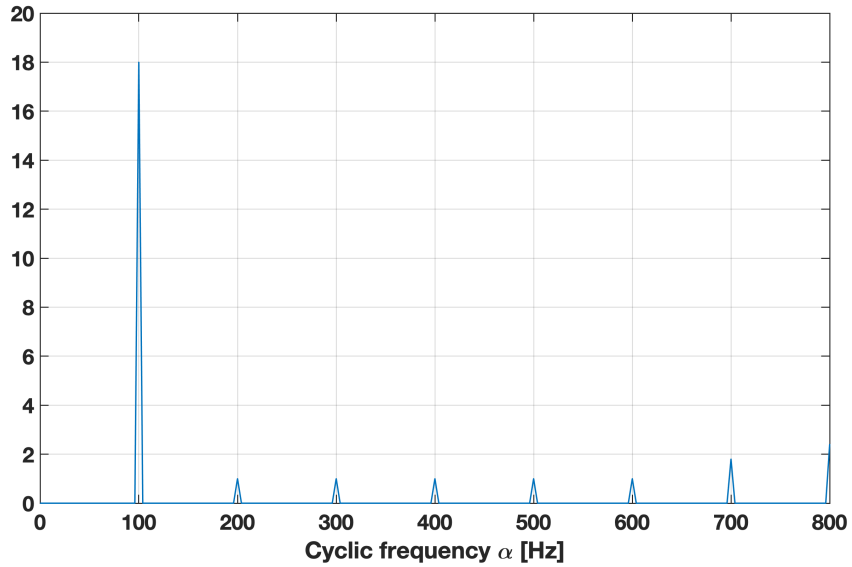


Figure 6.14: PRI transform results for the Radar-4 signal

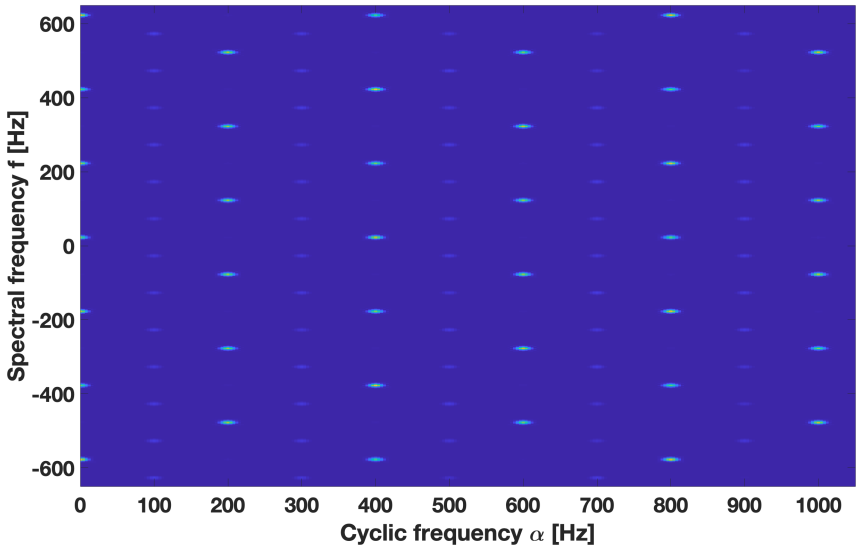


Figure 6.15: CSD of the Radar-5 signal

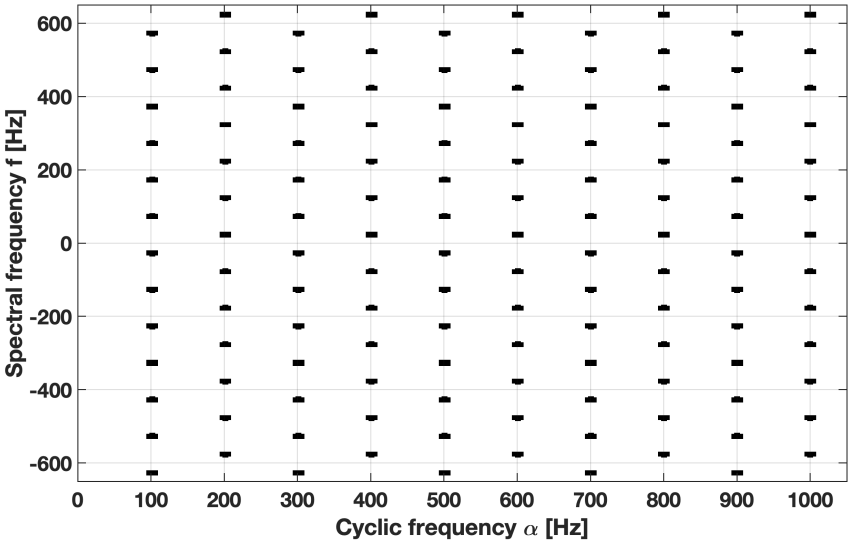


Figure 6.16: CFAR detections in the CSD for the Radar-5 signal

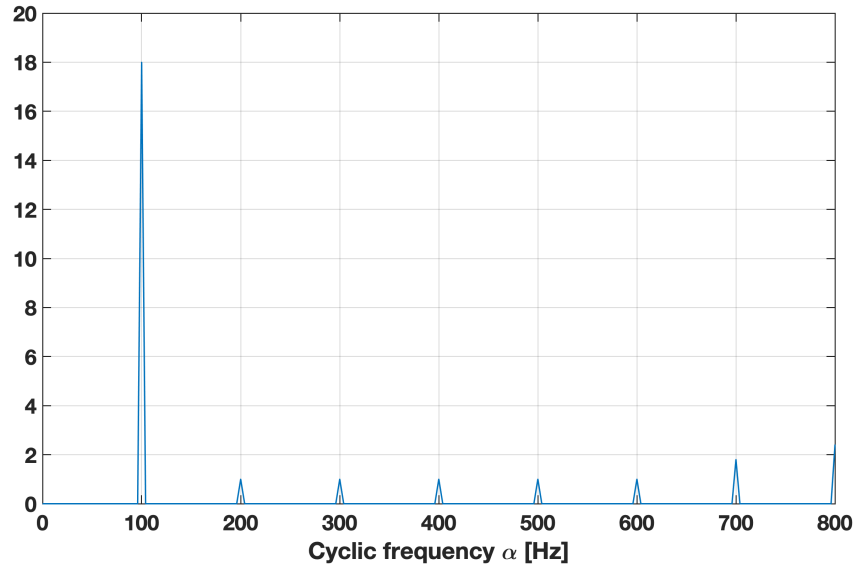


Figure 6.17: PRI transform results for the Radar-5 signal

Table 6.1: True and estimated Doppler frequencies

| True Doppler (Hz) | Estimated Doppler (Hz) |
|---|---|
| $-31.6$ | $-31.6$ |
| $0$ | $0.28$ |
| $31$ | $29.63$ |
| $-22.56$ | $-23$ |
| $-22.94$ | $-22.9$ |

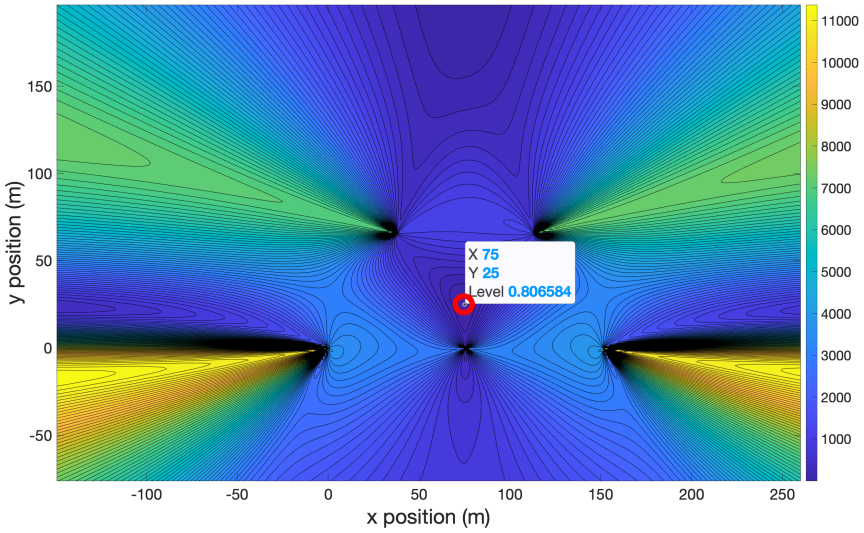


Figure 6.18: Localization results for the simulated scenario

### 6.1.2 Single Propeller With Image Peak Detection

In the previous section, at the peak detection step, CFAR algorithm is used. In order to show the applicability of the image peak detection algorithm, in this section, the same scenario as in the previous section with no noise is studied with MATLAB's image peak detection algorithm. The 'imhmax' and 'imregionalmax' functions of MATLAB are used. Imhmax algorithm is used to keep only CSD components that are above 20 dB compared to the mean value of the CSD data. Imregionalmax algorithm performs peak detection.

The CSD data on which these functions run are shown in Figure 6.19. Using 'imhmax' and 'imregionalmax' functions the detections shown in Figure 6.20 are obtained. In Figure 6.21 the results of the PRI transform for the peaks are shown. With these results, the applicability of image peak detection algorithms to the problem is shown. Image peak detection algorithms can also be used in the problem instead of CFAR.

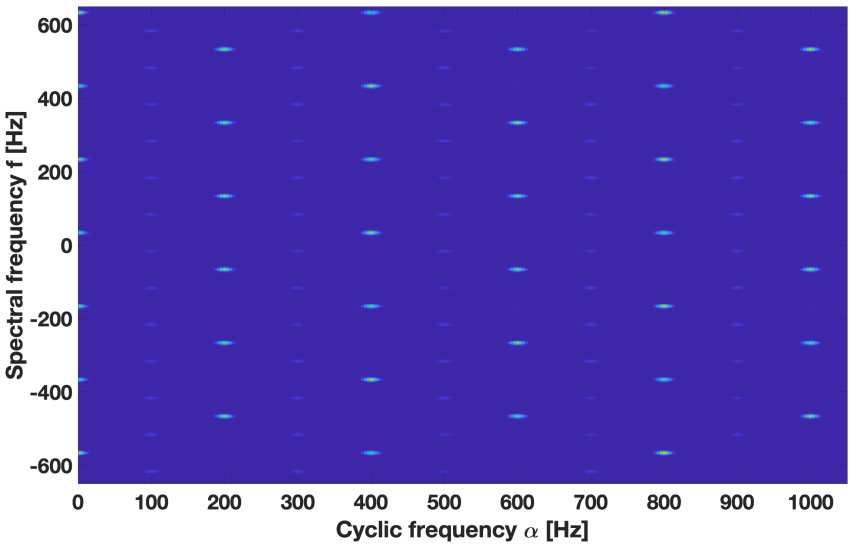


Figure 6.19: CSD for the image peak detection

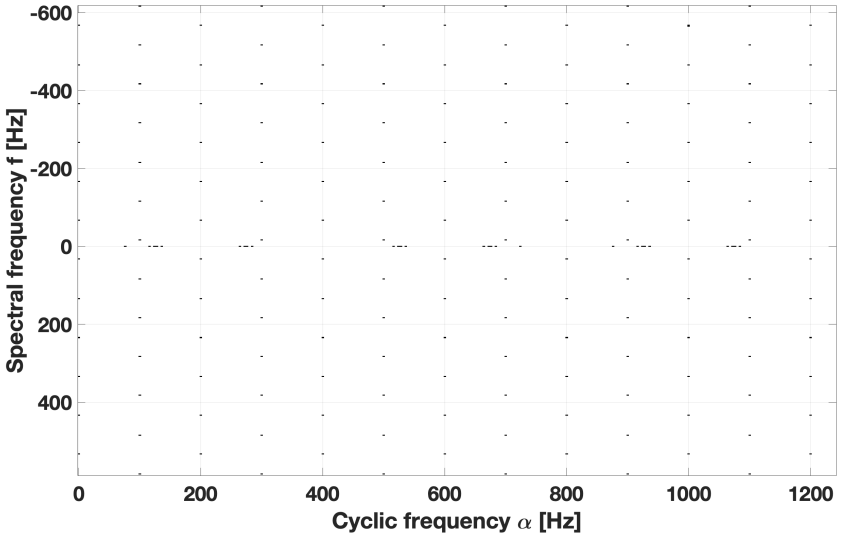


Figure 6.20: Detected peaks with 'imhmax' and 'imregionalmax' functions

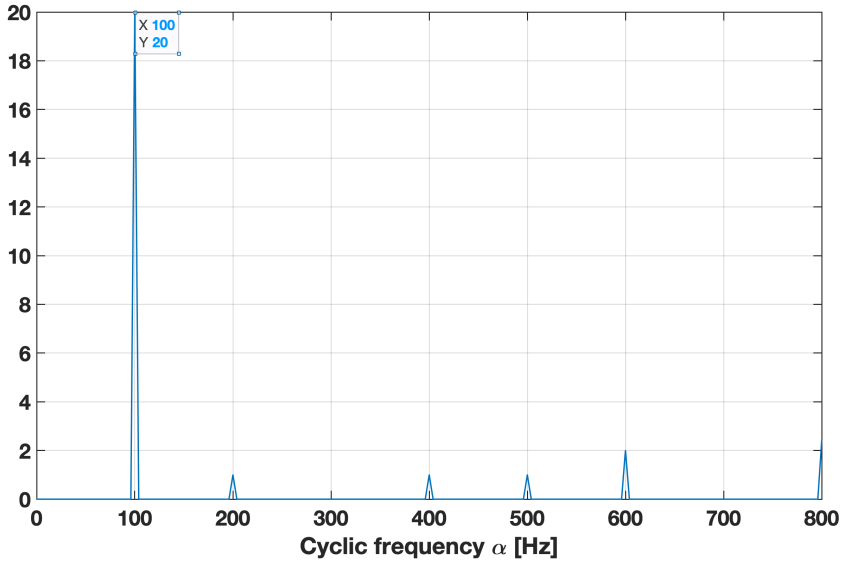


Figure 6.21: PRI transform output for the detected peaks

### 6.1.3 Propeller and Drone Body

In the previous section, simulation results for a propeller radar echo is presented. In this section, the drone body echo signal is also added to the propeller echo signal. The propeller has one blade as in the previous section and it rotates at a rate of 100 Hz. The radar frequency is assumed to be 5 GHz. The drone is assumed to be moving away from the radar at 2 m/s speed. The RCS difference between the propeller and the drone body is assumed to be 20 dBsm.

The CSD of the combined signal is shown in Figure 6.22. The components created by the propeller signal are present. The body signal intersects with the drone signal at bright spots along slant lines. In Figure 6.23 the CFAR results are shown. At 100 Hz the detections are apparent different from the Figure 6.22. Some components of CSD are low in amplitude such that they cannot be seen in the CSD figure. In Figure 6.24 PRI transform result is presented with a peak at 100 Hz. The calculated Doppler frequency is 33 Hz.

According to these results, no adverse effect of drone body is observed on the algorithm.

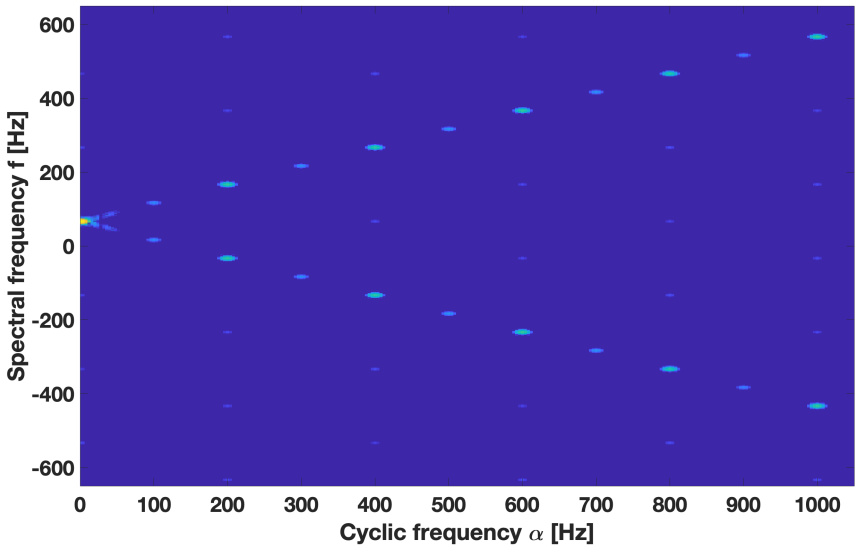


Figure 6.22: CSD of the combined propeller and drone body signal

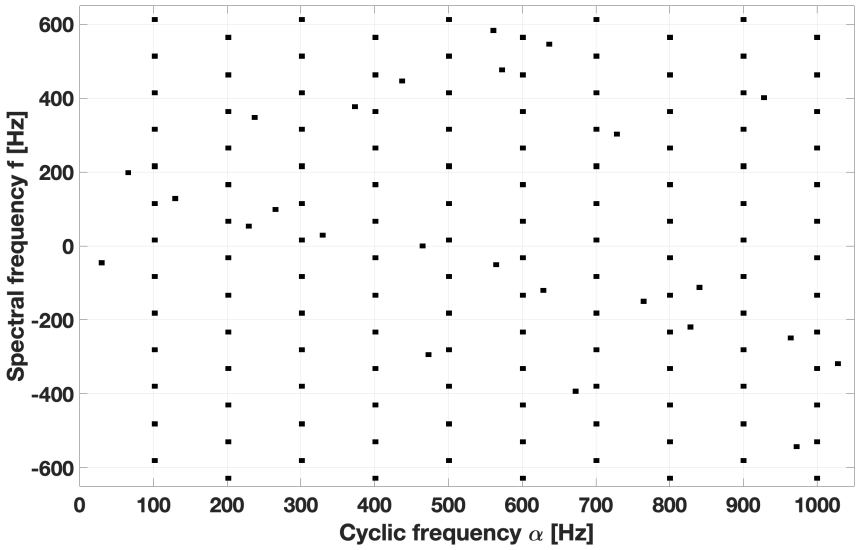


Figure 6.23: CFAR of combined propeller and drone body signal

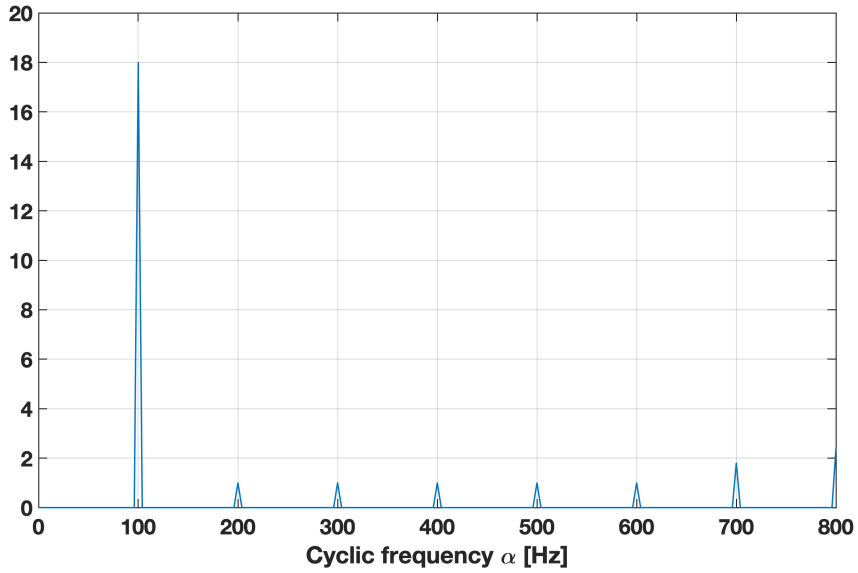


Figure 6.24: PRI transform results of combined propeller and drone body signal

### 6.1.4 Propeller, Drone Body and Moving Targets

Moving objects with the drone may be in the field of view of the sensors of the MIMO system. The effect of moving targets on the MCBD method is presented in this section. The parameters of the radar and drone in the previous are also valid here. In the simulation, three vehicles are assumed to be in the coverage area of the MIMO system. RCS of the vehicles are assumed to be the same as that of the drone body. Two of the vehicles are assumed to be going towards the sensor at speeds 10 and 15 m/s, the third vehicle moves away from the sensor at 17 m/s. In Figure 6.25 the CSD of the signal is shown. Along the spectral frequency axis the main Doppler frequencies of the targets are present and marked with red circles. The drone body on the spectral axis is shown with a green circle. The presence of other moving targets also generated false peaks. The peaks are generated with the cross terms between the propeller and the other moving targets. The cyclic frequency of these cross terms is affected by the Doppler frequency of the propeller and the target. The Doppler shift frequencies of the propeller and the moving target affected amount of cyclic frequency shift from the propeller rotation frequency. Also, the cross terms peak's spectral frequency is also affected by the Doppler shift frequencies of the propeller and the moving target.

The periodicity on the cyclic frequency is also apparent in the CFAR results (Figure 6.26). In the output of the PRI transform, there is a clear peak that leads to the drone detection decision (Figure 6.27).

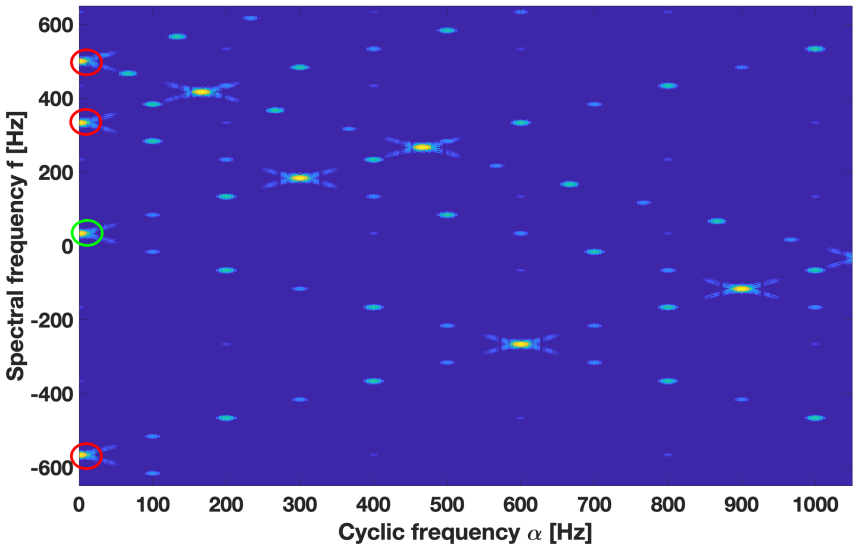


Figure 6.25: CSD of combined propeller, drone body, and targets signal

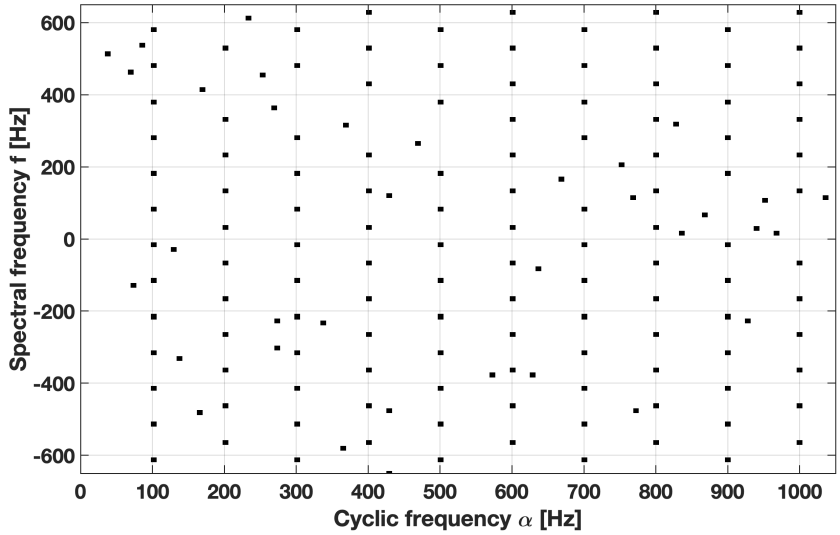


Figure 6.26: CFAR of combined propeller, drone body, and targets signal

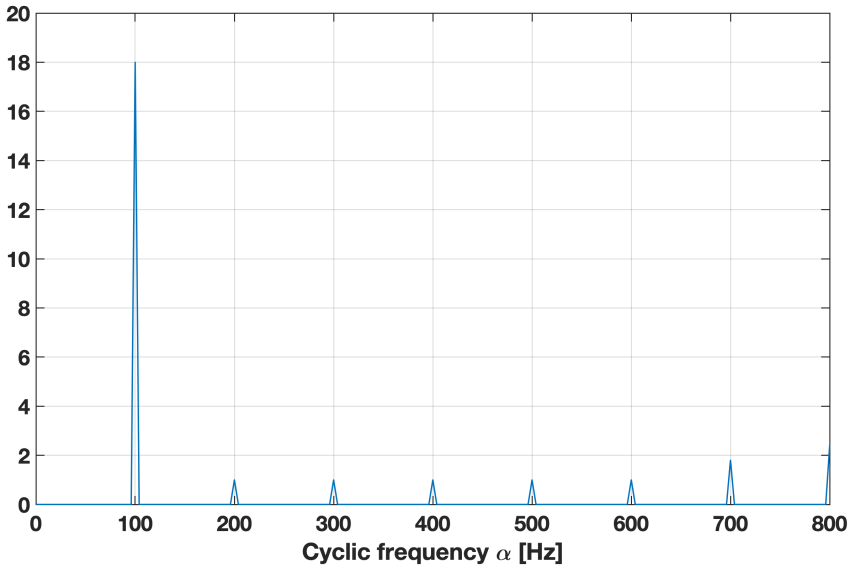


Figure 6.27: PRI transform results of combined propeller, drone body, and targets signal

### 6.1.5 Multiple Propellers

The CSD is a non-linear transformation. The sum of multiple propeller signals can cause cross terms on the CSD plane due to non-linearity. In this section, the behavior of the MCSD method under multiple propeller signals is examined. For this simulation purpose, three propeller signals are considered. The first propeller has a rotation frequency of 100 Hz and a radial velocity of 1 m/s with respect to the sensor. The second propeller has a rotation frequency of 120 Hz and a radial velocity of 0.5 m/s with respect to the sensor. The rotation frequency of the third propeller is 140 Hz and the radial velocity is 1.5 m/s. Since sensor's operating frequency is 5 GHz, the true Doppler shift values are 33.3 Hz and 16.6 Hz for the first and the second targets, respectively.

In the first simulation the first and the second propellers are included. In Figure 6.28 the CSD of the sum signal from the first and the second propeller is shown. The yellow rectangles show some of the CSD peaks resulting from the propellers. The red circles show the cross spectral peaks generated due to non-linear transform. The CFAR results and the PRI transform results are shown in Figure 6.29 and Figure 6.30, respectively. The PRI transform shows the peaks at true rotation frequencies. The estimated Doppler frequency values are 32 Hz and 16 Hz for the first and second drones, respectively. Both the cyclic frequencies and the Doppler frequencies coincide with the true values.

The second simulation includes the third propeller in addition to the first and second propeller. The third propeller has a rotation frequency of 140 Hz and a radial velocity of 1.5 m/s, which causes a 50 Hz Doppler shift. The CSD for three propellers is shown in Figure 6.31. Similarly to the first simulation, the true components are shown in a yellow rectangle and the cross components are shown in a red circle. The CFAR and the PRI transform results shown in Figure 6.32 and Figure 6.33, respectively. The rotation frequencies of the drones are clearly apparent in the PRI transform. The estimated Doppler shift values are 30, 12, and 45 Hz for the first, second, and the third drone, respectively. Although rotation frequencies are determined correctly, Doppler frequency accuracy values decreased compared to the two drones case.

Figures 6.28 and 6.31 includes cross CSD terms. Although these terms are not placed in straight lines, their occurrence challenges the proposed approach. The cross terms also generate peaks in the PRI transform at low cyclic frequencies. These peaks can be eliminated since the frequencies are low enough to be eliminate when the typical drone's propeller rotation rates are considered. At common multiples of rotation frequencies false spectral frequency values can be estimated. So, after estimating the cyclic frequencies, the common multiples of these frequencies must be avoided in the Doppler calculation step.

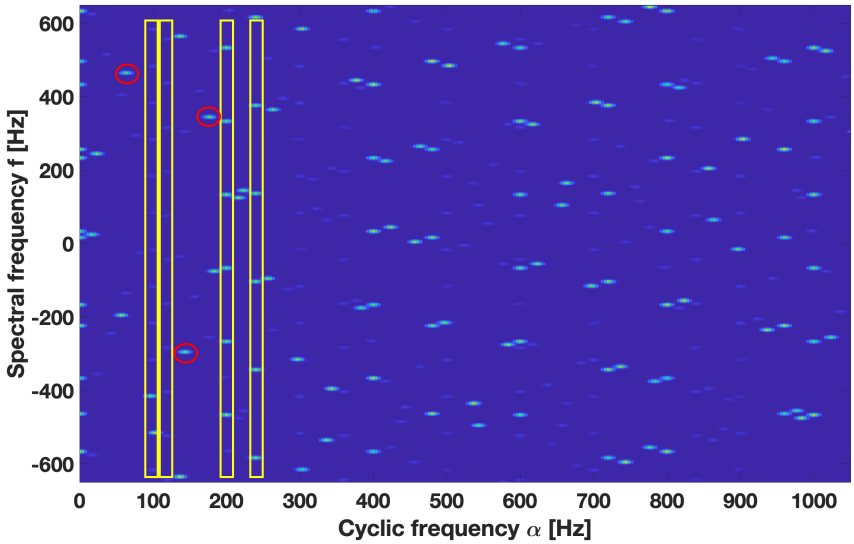


Figure 6.28: CSD of two propeller signals

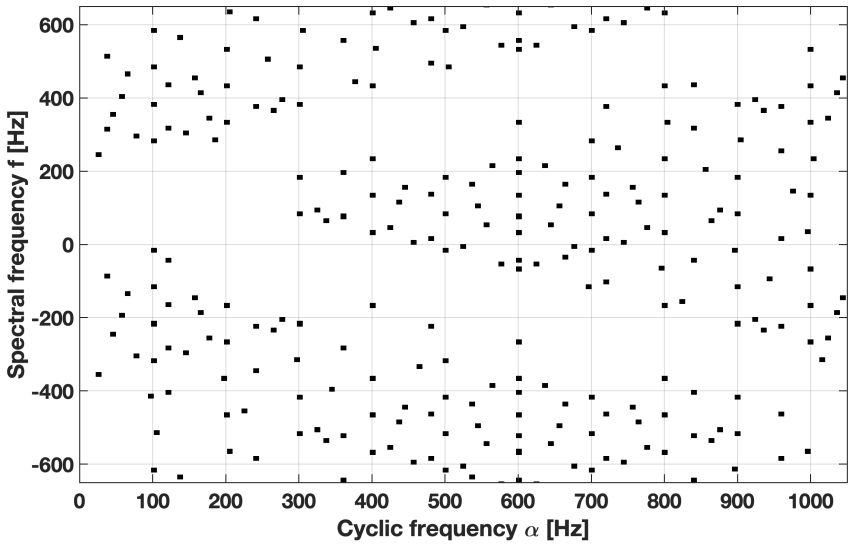


Figure 6.29: CFAR of two propellers

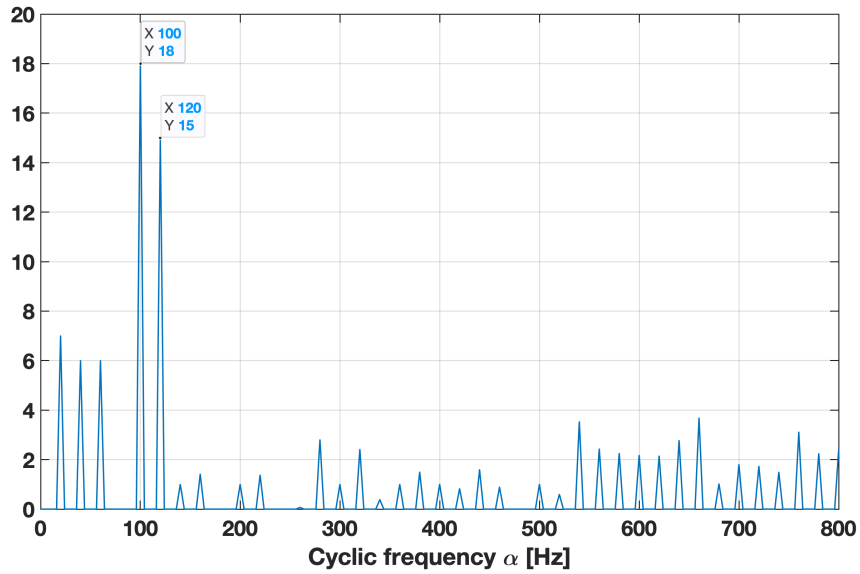


Figure 6.30: PRI transform results of two propellers

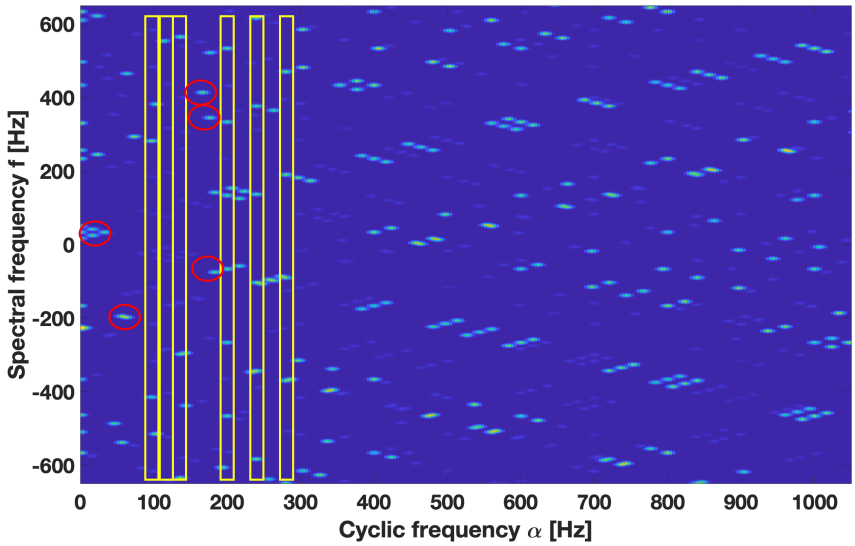


Figure 6.31: CSD of three propeller signals

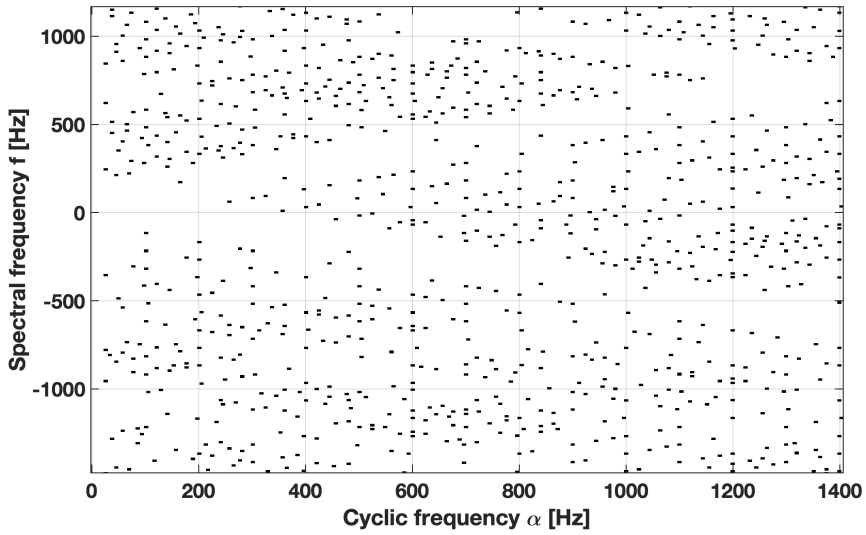


Figure 6.32: CFAR of three propellers

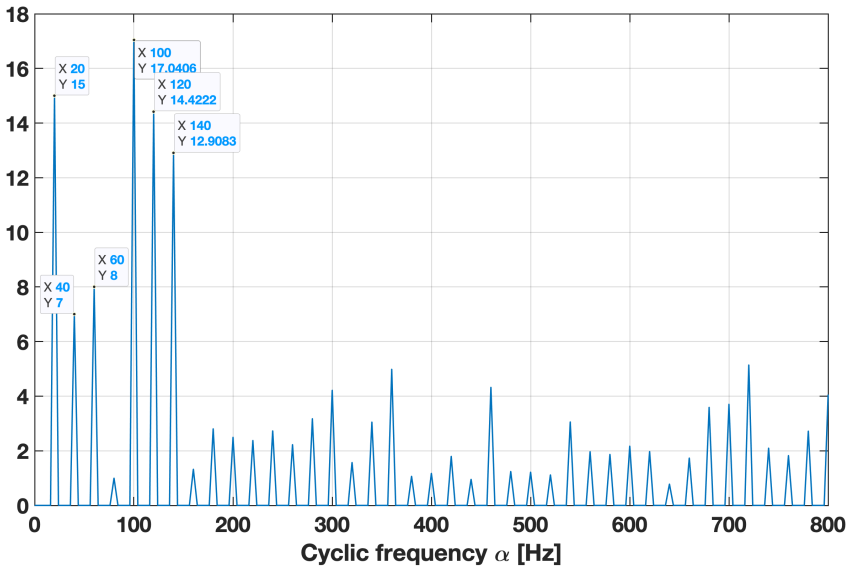


Figure 6.33: PRI transform results of three propellers

## 6.2 Experimental Results

In this section the experimental results of the MCSD method are presented. In the first subsection the results for a propeller are shown. In the second subsection results for a drone are analyzed.

### 6.2.1 Experimental Results with Propeller

In order to prove the concept presented here, measurements are performed with a CW radar and a propeller. Since Doppler only localization is a well studied method in the literature, it is sufficient to show that the Doppler frequency can be calculated with the MCSD method using a single CW radar. For this purpose, the CFK024-5A RF module is used as the radar transmitter and receiver in the measurements. The module properties are as follows:

- Frequency: 24 GHz
- Waveform: CW
- ERP: 16 dBm
- Azimuth beam width: 80 degrees
- Elevation beam width: 32 degrees
- Frequency modulation: 250 MHz frequency tuning range

The module and pins are presented in Figure 6.34. This RF module is used with an Arduino Uno for required interfaces. The module can produce in-phase and quadrature outputs at baseband. These outputs are sampled with computer audio input. The structure of the experimental setup is shown in 6.35. As the target, a propeller is used rotating at an rpm of 1700-1750 rpm. The propeller has two blades, so both cyclic and spectral frequency peak periods in the CSD will be compatible 3400-3500 rpm. The rpm value of the propeller is measured with a laser tachometer. The signal observation time is 250 ms.

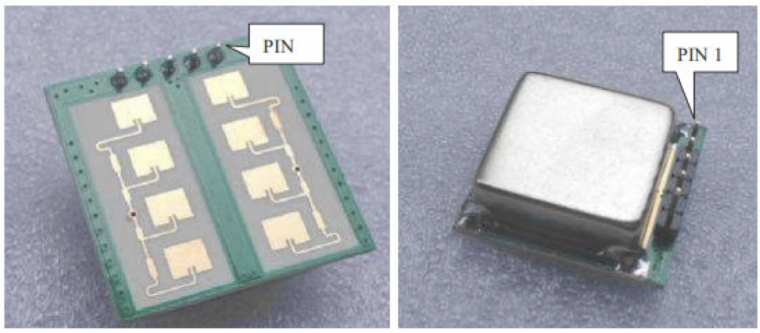


| | | |
|---|---|---|
| **PIN 1** | VT | VCO frequency tuning input (0-2V) |
| **PIN 2** | GND | 0V supply |
| **PIN 3** | IF_I | In phase down converter IF output |
| **PIN 4** | VCC | Supply voltage 5V |
| **PIN 5** | IF_Q | Quadrature phase down converter IF output |

Figure 6.34: RF module in the measurements

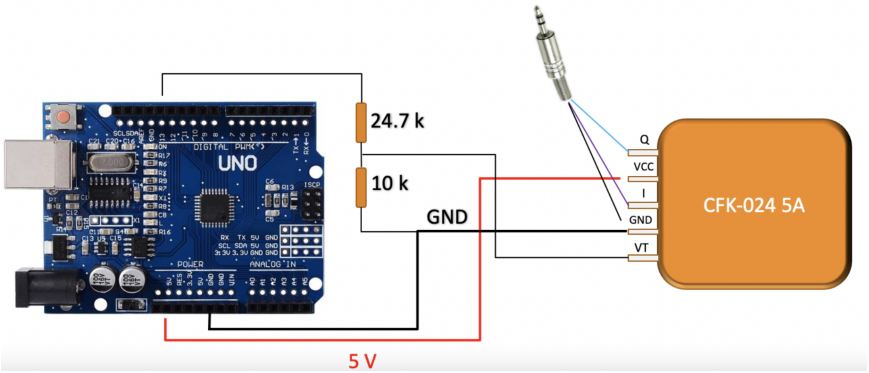


Figure 6.35: Experimental setup

In the experiment, the propeller is placed 1 meter away from the CFK024-5A RF module. Then the propeller is moved away from the RF module at an approximately 10 cm/s speed. This scenario is presented in Figure 6.36.

In Figure 6.37, CSD of the measurement is presented. Unlike the simulation results, the micro-Doppler components in the CSD plane are low in magnitude. The fundamental cyclic frequency is found to be 57 Hz for the two-blade propeller. The CFAR result is presented in Figure 6.38. The output of the CFAR includes micro-Doppler signals and noise. In order to extract the micro-Doppler frequency, histogram based deinterleaving algorithm is used, and the related histogram results are presented in

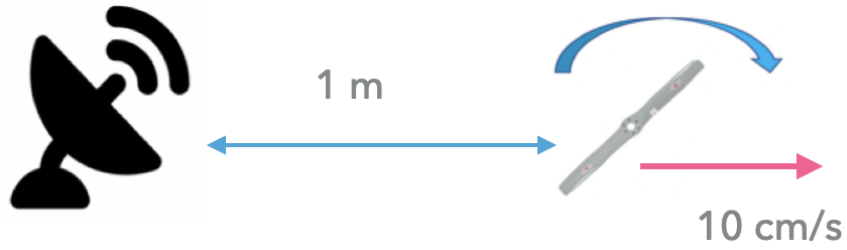


Figure 6.36: Experiment scenario

Figure 6.39. Within these results, it is readily seen that 57.28-61.44 Hz is the histogram bin, which has integer multiples in higher order difference histograms. In Figure 6.40 the PRI transform of the measured signal is presented. The peak appearing in the PRI transform is at 57.32 Hz. Besides this peak, there are also some small local peaks in the result. These small local peaks are evaluated to be caused by the noise components.

Using the estimated cyclic frequency value, the Doppler shift is estimated to be -13.73 Hz. This Doppler frequency corresponds to a radial velocity of 8.6 cm/s. This result coincides with the experimental motion, which is nearly 10 cm/s. This result shows that the MCSD algorithm can measure the Doppler frequency directly from the micro-Doppler signals. Using this Doppler calculation method, it is straight forward to locate the source using the approach presented in Section 3.6 .

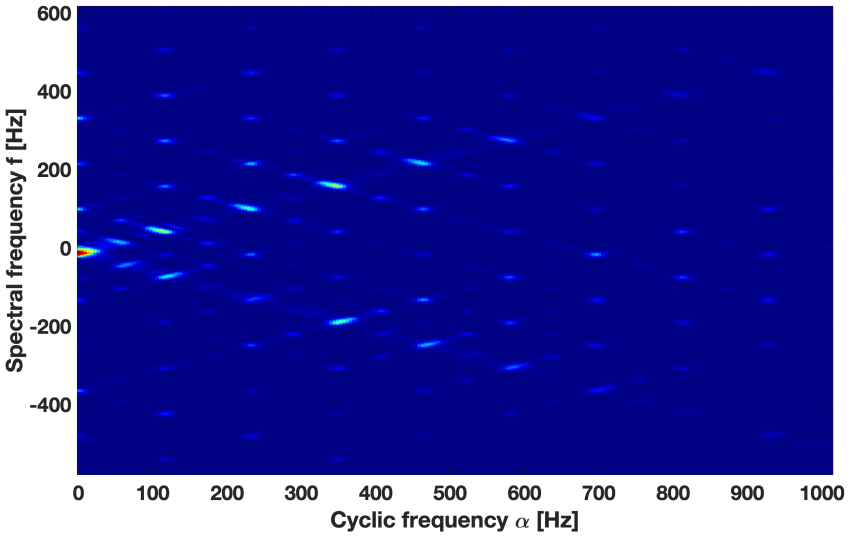


Figure 6.37: CSD of the measured propeller echo signal

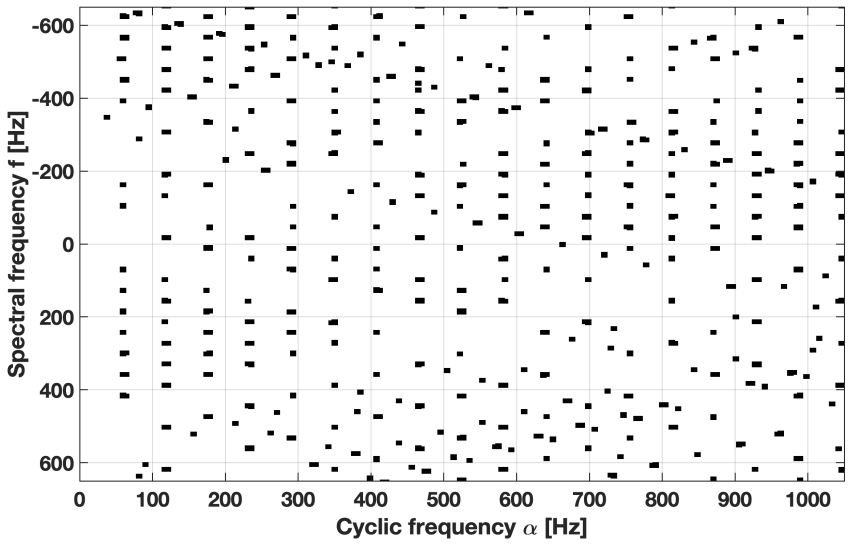


Figure 6.38: CFAR detections in the CSD of the measured propeller echo signal

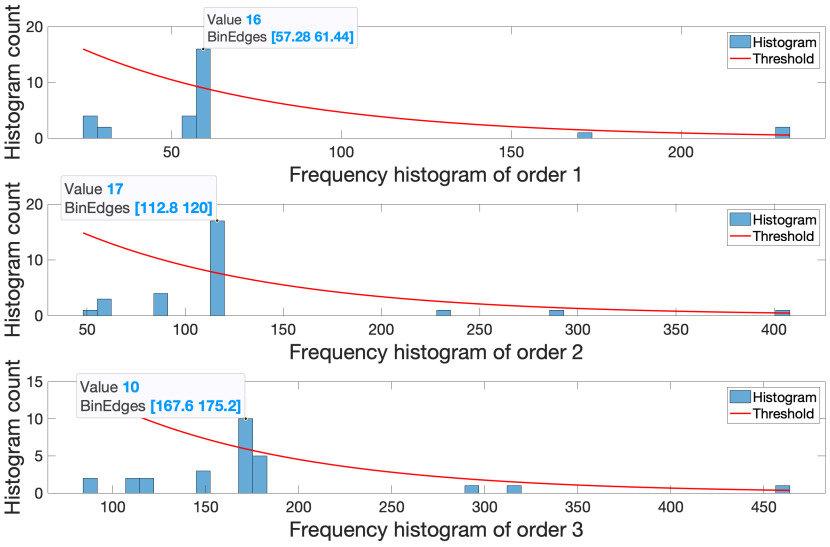


Figure 6.39: Histogram based deinterleaving results for measured signal

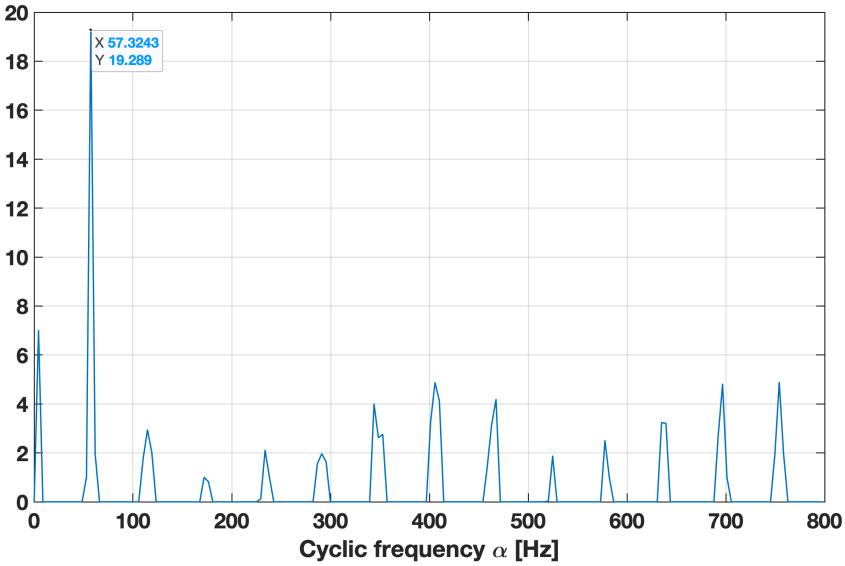


Figure 6.40: PRI transform results for measured signal

### 6.2.2 Experimental Results with Drone

In the previous section a single propeller is used as the target to prove the concept presented here. In this section experimental result performed with a drone is presented. The same sensor is used as in the experiments with the propeller. The drone in the experiment is Silverlit Gripper which is shown in Figure 6.41. In this experiment the drone is stationary so that the theoretical Doppler frequency is $0$ Hz.

In Figure 6.42 the CSD of the return signal from the radar is shown. The noise components and the periodicity caused by the propellers is apparent. The CFAR results of the CSD is shown in Figure 6.38. The false detections caused by the noise is also present at some points in the CFAR output. In Figure 6.44 the output of the PRI transform is shown. At $99.9$ Hz the peak is present. This value coincides with the periodicity seen in Figure 6.42. So the estimated rotation frequency $f_r$ is $99.9$ Hz. The output of the Doppler frequency estimation is $2$ Hz, which can be an acceptable result considering the frequency resolution.

Figure 6.41: Silverlit Gripper drone used in the experiment

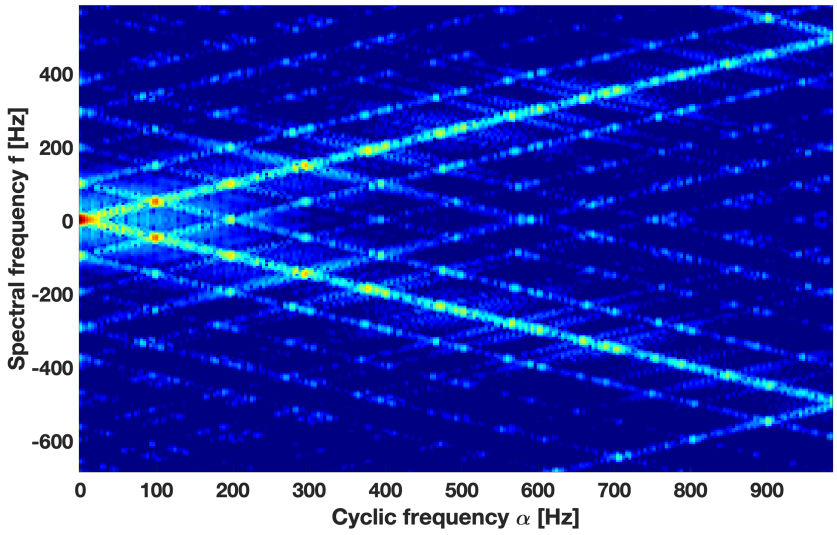


Figure 6.42: CSD of the measured drone echo signal

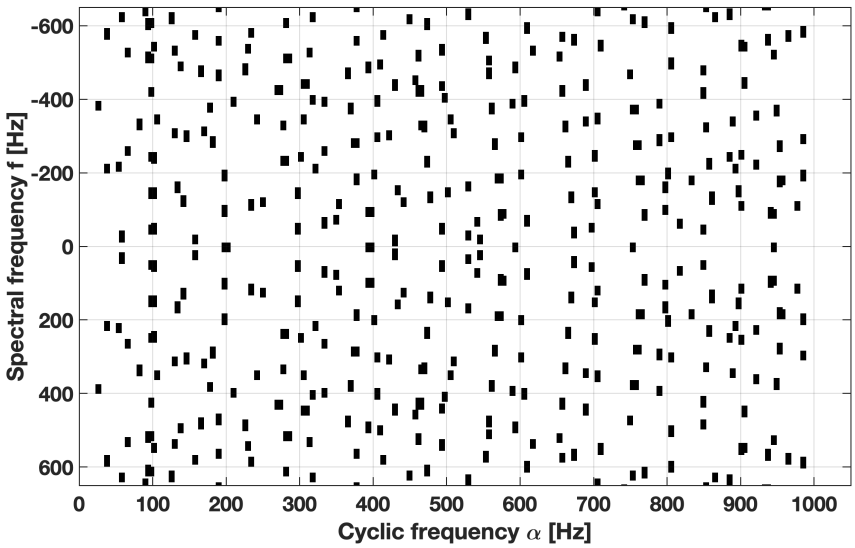


Figure 6.43: CFAR detections in the CSD of the measured drone echo signal

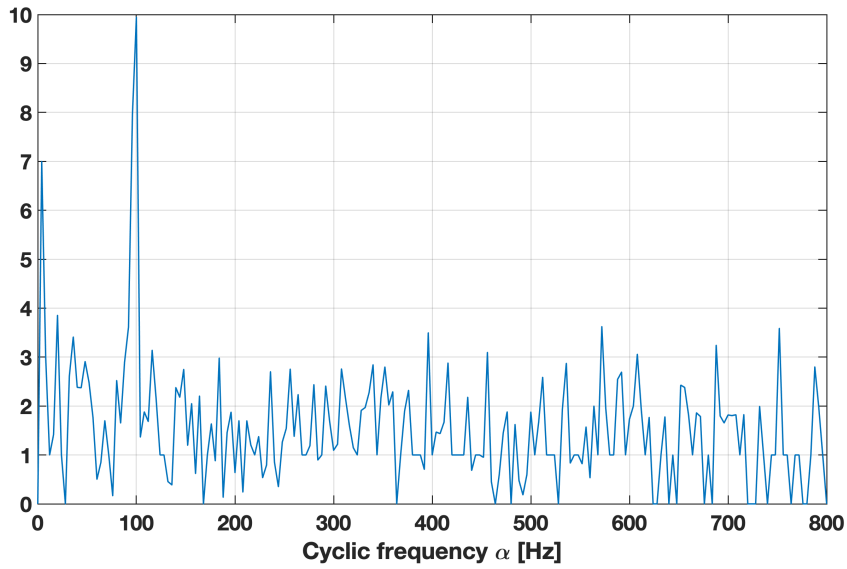


Figure 6.44: PRI transform results for drone signal

# CHAPTER 7

# CONCLUSIONS

In this study, a new technique, namely the MCSD method, is presented to detect drones. The main motivation of the study is to create a system solution that is affordable, scalable, and suitable for use in urban areas. The MCSD method basically relies on cyclostationarity analysis. Using cyclostationarity analysis, separation of the drone signal from other interfering signals is aimed.

The MCSD method determines the fundamental cyclic frequency of the micro-Doppler signal, the Doppler shift caused by the motion of the drone in the CSD plane. The detection and classification steps are performed jointly in the CSD plane. The deinterleaving algorithm, which is mainly an ESM algorithm, is used in the detection and estimation steps. Using the estimated cyclic frequency, the Doppler shift caused by the radial motion of the target with respect to the radar is shown. Using this information for multiple radars, localization of target can be performed. The theory of cyclostationarity and studies with the drone signals in the literature prove the applicability of the CSD to the drone signals. In this thesis, both simulations and the measurement results with the propeller signal are covered. In addition to the single propeller, the results with the drone return signals are also used in the verification of the proposed method. Although CSD analysis is said to be a promising method to detect and classify cyclostationary signals in the presence of stationary signals, most studies in the literature are performed with only the cyclostationary signal. The problem of interest in this thesis also includes moving targets with stationary return signals and multiple drones. Both of these cases are studied with simulations, and the performance of the proposed approach is presented.

The results show that in the presence of a target with stationary return signals, the

MCSD algorithm performs as expected and has not experienced any difficulty in the detection and parameter estimation of the drone. For the multiple drone scenario, two and three drone cases are studied. In the two drones case the MCSD method successfully estimated the parameters of both drones. In the case of three drones, although the MCSD method determined the propeller rotation frequencies of the drones, the accuracy in the Doppler shift calculation is decreased. The cross cyclic terms on CSD in the presence of multiple targets created unwanted peaks in the CSD plane. But it is also observed that the main pattern created by the propellers are also preserved in the CSD plane. So, with proper algorithm and parameter tunings, multiple drones case can also be handled with the MCSD method.

Since the aim of the study is to develop a low cost drone detection and localization system, the cost analysis of the MCSD method is also presented. The system solution is evaluated to be useful, especially in coverage limited and Doppler crowded environments, for drone detection purposes. The monostatic radar and the MCSD method MIMO radar are very different in architecture, so it is hard to make a fair comparison. The MCSD method MIMO radar has full time observation in the area of coverage. On the other hand, in a general sense, typical monostatic radars are scanning the area of coverage with a narrow beam antenna. Therefore, monostatic radars have limited time to observe targets. This observation time, ToT, may not be a problem in typical radar operating environments, such as open ares. But in urban areas, higher ToTs can be required since a drone can pass through buildings, obstacles, etc. in a very short time duration. For both monostatic radars and MIMO radars, the ToT requirement in urban environments can be an interesting research topic.

As a performance metric, the localization CRLB analysis of the MCSD method is presented and compared to the monostatic radar. The results show that, because of the narrow bandwidth required, the MCSD method outperforms the monostatic radar. The range estimation performance of monostatic radar directly related to its bandwidth. To obtain a good range estimation performance, monostatic radars use wideband signals. As a result of wideband waveforms, the noise level in monostatic radars is high compared to CW MIMO radar systems. For CW MIMO radars, a bandwidth that is on the order of estimated maximum Doppler shift frequency is enough.

The proposed approach in this thesis can be further extended with the following future works:

- In this thesis, only Doppler shift information generated by the sensors is used. With frequency switching in CW sensors range information can also be obtained. This approach will be a promising future work without affecting the general architecture proposed in this thesis.
- Different drones with different propellers can generate cross cyclic spectral behavior in the CSD plane. The nature of cross cyclic spectral components can be investigated.
- Different estimation techniques can be studied to estimate the cyclic frequency.
- The deinterleaving algorithm used in this thesis does not work on directly CSD plane. A 2D deinterleaving algorithm can be proposed to work directly in the CSD plane.
- Fusion of legacy system outputs with the MCSD method generated output can be studied to serve for different operational conditions. If the information to be fused has different types, heterogeneous fusion concepts can be studied for drone detection.
- The application of the MCSD method in acoustic systems can also be evaluated.

# REFERENCES


[1] A. Schumann, L. Sommer, J. Klatte, T. Schuchert, and J. Beyerer, "Deep cross-domain flying object classification for robust uav detection," in *2017 14th IEEE International Conference on Advanced Video and Signal Based Surveillance (AVSS)*, pp. 1–6, 2017.

[2] P. Nguyen, H. Truong, M. Ravindranathan, A. Nguyen, R. Han, and T. Vu, "Matthan: Drone presence detection by identifying physical signatures in the drone's rf communication," pp. 211–224, 06 2017.

[3] S. Harman, "A comparison of staring radars with scanning radars for uav detection: Introducing the alarm™ staring radar," in *2015 European Radar Conference (EuRAD)*, pp. 185–188, 2015.

[4] F. Hoffmann, M. Ritchie, F. Fioranelli, A. Charlish, and H. Griffiths, "Micro-doppler based detection and tracking of uavs with multistatic radar," in *2016 IEEE Radar Conference (RadarConf)*, pp. 1–6, 2016.

[5] A. Aldowesh, M. Shoaib, K. Jamil, S. Alhumaidi, and M. Alam, "A passive bistatic radar experiment for very low radar cross-section target detection," in *2015 IEEE Radar Conference*, pp. 406–410, 2015.

[6] Y. Liu, X. Wan, H. Tang, J. Yi, Y. Cheng, and X. Zhang, "Digital television based passive bistatic radar system for drone detection," in *2017 IEEE Radar Conference (RadarConf)*, pp. 1493–1497, 2017.

[7] Y. Zhao and Y. Su, "Cyclostationary phase analysis on micro-doppler parameters for radar-based small uavs detection," *IEEE Transactions on Instrumentation and Measurement*, vol. 67, no. 9, pp. 2048–2057, 2018.

[8] J. Farlik, M. Kratky, J. Casar, and V. Stary, "Radar cross section and detection of small unmanned aerial vehicles," in *2016 17th International Conference on Mechatronics - Mechatronika (ME)*, pp. 1–7, 2016.

[9] J. Li and P. Stoica, "Mimo radar with colocated antennas," *IEEE Signal Processing Magazine*, vol. 24, no. 5, pp. 106–114, 2007.

[10] M. William L. and S. James A., *Principles of Modern Radar : Radar Applications, Volume 3.* No. Vol. III, Radar applications in Principles of Modern Radar, SciTech Publishing, 2014.

[11] C. Alabaster, *Pulse Doppler Radar: Principles, Technology, Applications*. Electromagnetics and Radar, Institution of Engineering and Technology, 2012.

[12] R. Mark A., S. James A., and H. William A., *Principles of Modern Radar : Basic Principles, Volume 1.* No. Volume I, Basic principles in Principles of Modern Radar, SciTech Publishing, 2010.

[13] K. Sakai, M.-T. Sun, W.-S. Ku, T. H. Lai, and A. V. Vasilakos, "A framework for the optimal k-coverage deployment patterns of wireless sensors," *IEEE Sensors Journal*, vol. 15, no. 12, pp. 7273–7283, 2015.

[14] C. Aker and S. Kalkan, "Using deep networks for drone detection," in *2017 14th IEEE International Conference on Advanced Video and Signal Based Surveillance (AVSS)*, pp. 1–6, 2017.

[15] L. Sommer, A. Schumann, T. Müller, T. Schuchert, and J. Beyerer, "Flying object detection for automatic uav recognition," in *2017 14th IEEE International Conference on Advanced Video and Signal Based Surveillance (AVSS)*, pp. 1–6, 2017.

[16] E. E. Case, A. M. Zelnio, and B. D. Rigling, "Low-cost acoustic array for small uav detection and tracking," in *2008 IEEE National Aerospace and Electronics Conference*, pp. 110–113, 2008.

[17] B. Knoedler, R. Zemmari, and W. Koch, "On the detection of small uav using a gsm passive coherent location system," in *2016 17th International Radar Symposium (IRS)*, pp. 1–4, 2016.

[18] C. Schüpbach, C. Patry, F. Maasdorp, U. Böniger, and P. Wellig, "Micro-uav detection using dab-based passive radar," in *2017 IEEE Radar Conference (RadarConf)*, pp. 1037–1040, 2017.

[19] K. Li, Y. Liu, K. Huo, W. Jiang, X. Li, and Z. Zhuang, "Estimation of micro-motion parameters based on cyclostationary analysis," *IET Signal Processing*, vol. 4, no. 3, pp. 218–223, 2010.

[20] V. C. Chen, F. Li, S. . Ho, and H. Wechsler, "Micro-doppler effect in radar: phenomenon, model, and simulation study," *IEEE Transactions on Aerospace and Electronic Systems*, vol. 42, no. 1, pp. 2–21, 2006.

[21] C. Clemente and J. J. Soraghan, "Gnss-based passive bistatic radar for micro-doppler analysis of helicopter rotor blades," *IEEE Transactions on Aerospace and Electronic Systems*, vol. 50, no. 1, pp. 491–500, 2014.

[22] Z. Yu, D. Zhao, and Z. Zhang, "Doppler radar vital signs detection method based on higher order cyclostationary," *Sensors*, vol. 18, p. 47, 12 2017.

[23] X. Guo, C. S. Ng, E. de Jong, and A. B. Smits, "Concept of distributed radar system for mini-uav detection in dense urban environment," in *2019 International Radar Conference (RADAR)*, pp. 1–4, 2019.

[24] Z. Cao, Y. Yuan, W. Yi, and L. Chen, "An adaptive power allocation scheme for mini-uav tracking with distributed radar in dense urban environment," in *2021 International Conference on Control, Automation and Information Sciences (ICCAIS)*, pp. 866–871, 2021.

[25] X. Guo, C. S. Ng, E. de Jong, and A. B. Smits, "Micro-doppler based mini-uav detection with low-cost distributed radar in dense urban environment," in *2019 16th European Radar Conference (EuRAD)*, pp. 189–192, 2019.

[26] J. Martin and B. Mulgrew, "Analysis of the theoretical radar return signal form aircraft propeller blades," in *IEEE International Conference on Radar*, pp. 569–572, 1990.

[27] M. K. Baczyk, P. Samczyński, K. Kulpa, and J. Misiurewicz, "Micro-doppler signatures of helicopters in multistatic passive radars," *IET Radar, Sonar Navigation*, vol. 9, no. 9, pp. 1276–1283, 2015.

[28] J. Niu, K. Li, W. Jiang, X. Li, G. Kuang, and H. Zhu, "A new method of micro-motion parameters estimation based on cyclic autocorrelation function," *Science China Information Sciences*, vol. 56, 2012.

[29] M. A. Govoni, "Micro-doppler signal decomposition of small commercial drones," in *2017 IEEE Radar Conference (RadarConf)*, pp. 0425–0429, 2017.

[30] J. Martin, *Analysis of the Radar Return Signal From Rotating Aircraft Blades*. PhD thesis, University of Edinburgh, 1992.

[31] M. H. Hayes, *Statistical Digital Signal Processing and Modeling*. USA: John Wiley and Sons, Inc., 1st ed., 1996.

[32] P. Peebles, *Probability, Random Variables, and Random Signal Principles*. McGraw-Hill series in electrical and computer engineering, McGraw-Hill, 2001.

[33] Y. Zhou, J. Chen, G. M. Dong, W. B. Xiao, and Z. Y. Wang, "Wigner–ville distribution based on cyclic spectral density and the application in rolling element bearings diagnosis," *Proceedings of the Institution of Mechanical Engineers, Part C: Journal of Mechanical Engineering Science*, vol. 225, no. 12, pp. 2831–2847, 2011.

[34] A. V. Oppenheim, A. S. Willsky, and S. H. Nawab, *Signals and Systems (2nd Ed.)*. USA: Prentice-Hall, Inc., 1996.

[35] W. Gardner, "Exploitation of spectral redundancy in cyclostationary signals," *IEEE Signal Processing Magazine*, vol. 8, no. 2, pp. 14–36, 1991.

[36] J. Antoni, "Cyclic spectral analysis in practice," *Mechanical Systems and Signal Processing*, vol. 21, no. 2, pp. 597–630, 2007.

[37] J. Antoni, G. Xin, and N. Hamzaoui, "Fast computation of the spectral correlation," *Mechanical Systems and Signal Processing*, vol. 92, pp. 248–277, 2017.

[38] A. Schroder, M. Renker, U. Aulenbacher, A. Murk, U. Boniger, R. Oechslin, and P. Wellig, "Numerical and experimental radar cross section analysis of the quadrocopter dji phantom 2," in *2015 IEEE Radar Conference*, pp. 463–468, 2015.

[39] B. K. Kim, H. Kang, and S. Park, "Experimental analysis of small drone polarimetry based on micro-doppler signature," *IEEE Geoscience and Remote Sensing Letters*, vol. 14, no. 10, pp. 1670–1674, 2017.

[40] J. S. Patel, F. Fioranelli, and D. Anderson, "Review of radar classification and rcs characterisation techniques for small uavs or drones," *IET Radar, Sonar & Navigation*, vol. 12, no. 9, pp. 911–919, 2018.

[41] G. Curry, *Radar Essentials: A concise handbook for radar design and performance analysis*. 01 2012.

[42] A. M. Haimovich, R. S. Blum, and L. J. Cimini, "Mimo radar with widely separated antennas," *IEEE Signal Processing Magazine*, vol. 25, no. 1, pp. 116–129, 2008.

[43] J. Ochodnický, Z. Matousek, M. Babjak, and J. Kurty, "Drone detection by ku-band battlefield radar," in *2017 International Conference on Military Technologies (ICMT)*, pp. 613–616, 2017.

[44] Y. Liu and Q. Zhang, "Improved method for deinterleaving radar signals and estimating pri values," *IET Radar, Sonar Navigation*, vol. 12, no. 5, pp. 506–514, 2018.

[45] K. Nishiguchi and M. Kobayashi, "Improved algorithm for estimating pulse repetition intervals," *IEEE Transactions on Aerospace and Electronic Systems*, vol. 36, no. 2, pp. 407–421, 2000.

[46] I. Shames, A. N. Bishop, M. Smith, and B. D. O. Anderson, "Doppler shift target localization," *IEEE Transactions on Aerospace and Electronic Systems*, vol. 49, no. 1, pp. 266–276, 2013.

[47] M. M. Ahmed, K. C. Ho, and G. Wang, "3-d target localization and motion analysis based on doppler shifted frequencies," *IEEE Transactions on Aerospace and Electronic Systems*, vol. 58, no. 2, pp. 815–833, 2022.

[48] Y. Kalkan and B. Baykal, "Multiple target localization and data association for frequency-only widely separated mimo radar," *Digital Signal Processing*, vol. 25, pp. 51–61, 2014.

[49] R. Takahashi, K. Hirata, T. Hara, and A. Okamura, "Derivation of monopulse angle accuracy for phased array radar to achieve cramer-rao lower bound," in *2012 IEEE International Conference on Acoustics, Speech and Signal Processing (ICASSP)*, pp. 2569–2572, 2012.

[50] M. T. Ho, H. A. Krichene, G. F. Ricciardi, and W. J. Geckle, "A computationally-efficient, crlb-achieving range estimation algorithm," in *2015 IEEE Radar Conference (RadarCon)*, pp. 0005–0010, 2015.

[51] A. J. Haug, *Bayesian Estimation and Tracking*. New Jersey: John Wiley and Sons, 2012.

[52] M. A. Khan, H. Menouar, A. Eldeeb, A. Abu-Dayya, and F. D. Salim, "On the detection of unauthorized drones—techniques and future perspectives: A review," *IEEE Sensors Journal*, vol. 22, no. 12, pp. 11439–11455, 2022.

[53] P. A. Birjandi, L. Kulik, and E. Tanin, "K-coverage in regular deterministic sensor deployments," in *2013 IEEE Eighth International Conference on Intelligent Sensors, Sensor Networks and Information Processing*, pp. 521–526, 2013.

[54] A. Laučys, S. Rudys, M. Kinka, P. Ragulis, J. Aleksandravicius, D. Jablonskas, D. Bručas, E. Daugėla, and L. Maciulis, "Investigation of detection possibility of uavs using low cost marine radar," *Aviation*, vol. 23, pp. 48–53, 05 2019.

[55] S. Peleg and B. Porat, "The cramer-rao lower bound for signals with constant amplitude and polynomial phase," *IEEE Transactions on Signal Processing*, vol. 39, no. 3, pp. 749–752, 1991.

# APPENDIX A

## FOURIER SERIES COEFFICIENTS DERIVATION

In this appendix derivation of the Fourier series coefficients for the propeller echo signal is presented. This derivation is published in [30].

The derivation starts with the time domain signal model. The radar return signal A propeller can be written as the sum of the signals coming from point scatterers on the propeller. This can be mathematically written in integral form as in equation (A.1).

$$s(t) = \sum_{n=0}^{N-1} \int_0^L A_r^{'} \exp\left(-j\frac{4\pi}{\lambda} r\cos(\theta)\sin(2\pi f_r t + \frac{2\pi n}{N})\right) dr \qquad \text{(A.1)}$$

where $A_r^{'} = A_r \exp(j2\pi(f_c - f_d)t - j4\pi/\lambda R)$, $r$ represents the point scatterer distance from the rotation center and

- $L$: Length of the blade (meters).
- $N$: Number of blades.
- $R$: Range from center of the rotation to the radar (meters).
- $t$: Time (seconds).
- $v$: Radial velocity of the center of rotation with respect to the radar (meters/seconds).
- $\lambda$ : Wavelength of the transmitted signal (meters).
- $\theta$ : Angle between the plane of rotation and the line of sight from the radar to the center of rotation (radians).

- $f_c$: Frequency of the transmitted signal (Hz).
- $f_d$: Doppler shift frequency (Hz).
- $f_r$: Frequency of rotation (Hz).
- $A_r$: Amplitude of the return signal.

Using equation (A.3) equation (A.1) can be written as a Bessel series as in equation (A.2).

$$s(t) = \sum_{k=-\infty}^{\infty} \sum_{n=0}^{N-1} \int_0^L A_r^{'} J_k(-\frac{4\pi}{\lambda} r\cos(\theta)) \exp(-jk(2\pi f_r t + \frac{2\pi n}{N}))dr \tag{A.2}$$

where $J_k(x) = \sum_{l=0}^{\infty} \frac{(-1)^l (\frac{x}{2})^{k+2l}}{(k+l)!l!}$, which is Bessel function of the first kind and $k^{th}$ order.

$$\exp(jx\sin(\alpha)) = \sum_{k=-\infty}^{\infty} J_k(x)\exp(jk\alpha) \tag{A.3}$$

Equation (A.2) can be expanded as in equation (A.4).

$$\begin{aligned} s(t) = \sum_{k=-\infty}^{\infty} \int_0^L A_r^{'} J_k(-\frac{4\pi}{\lambda} r\cos(\theta)) \exp(-jk(2\pi f_r t)) \\ (\exp(j\frac{2\pi 0k}{N}) + \exp(j\frac{2\pi 1k}{N}) + \exp(j\frac{2\pi 2k}{N}) \cdots \exp(j\frac{2\pi(N-1)k}{N}))dr \end{aligned} \tag{A.4}$$

Equation (A.4) can be rewritten as equation (A.6) using equation (A.5).

$$\begin{aligned} \exp(j\frac{2\pi 0k}{N}) + \exp(j\frac{2\pi 1k}{N}) + \exp(j\frac{2\pi 2k}{N}) \cdots \exp(j\frac{2\pi(N-1)k}{N}) \\ = N\frac{\mathrm{sinc}(\pi k)}{\mathrm{sinc}(\frac{\pi k}{N})} \exp(j\frac{\pi(N-1)k}{N}) \end{aligned} \tag{A.5}$$

$$s(t) = \sum_{k=-\infty}^{\infty} \int_0^L A_r^{'} J_k(-\frac{4\pi}{\lambda} r\cos(\theta)) \exp(-jk(2\pi f_r t)) \\ N\frac{\text{sinc}(\pi k)}{\text{sinc}(\frac{\pi k}{N})} \exp(j\frac{\pi(N-1)k}{N}) dr \tag{A.6}$$

Equation (A.6) can be further simplified as equation (A.7) with the help of equation (A.8).

$$s(t) = \sum_{k=-\infty}^{\infty} \int_0^L A_r^{'} N J_k(-\frac{4\pi}{\lambda} r\cos(\theta)) \exp(-jNk(2\pi f_r t)) dr \tag{A.7}$$

$$N\frac{\text{sinc}(\pi k)}{\text{sinc}(\frac{\pi k}{N})} \exp(j\frac{\pi(N-1)k}{N}) = \begin{cases} 0, & \text{if } k \neq 0, \pm N, \pm 2N, \cdots. \\ N, & \text{if } k = 0, \pm N, \pm 2N, \cdots. \end{cases} \tag{A.8}$$

Using equations (A.10) and (A.11), (A.7) can be rewritten as equation (A.9).

$$s(t) = \sum_{k=-\infty}^{\infty} \sum_{l=0}^{\infty} \frac{2(-1)^{Nk} ArN}{\frac{4\pi}{\lambda}\cos(\theta)} \left( J_{N|k|+2l+1} \left( \frac{4\pi}{\lambda} L\cos(\theta) \right) \right) \exp(j2\pi Nk f_r t) \tag{A.9}$$

$$\int_0^x J_k(x)dx = 2\sum_{l=0}^{\infty} J_{k+2l+1}(x) \tag{A.10}$$

$$J_k(-x) = J_{-k}(x) = (-1)^k J_k(x) \tag{A.11}$$

Then the propeller signal can be defined as sum of complex exponentials as in equation (A.12) where Fourier series coefficients are given in equation (2.11).

$$s(t) = \sum_{k=-\infty}^{\infty} d_k \exp(j2\pi(f_c + f_d + kNf_r)t) \tag{A.12}$$

$$d_k = \sum_{l=0}^{\infty} \frac{2(-1)^{Nk} ArN}{\frac{4\pi}{\lambda}\cos(\theta)} \left( J_{N|k|+2l+1} \left( \frac{4\pi}{\lambda} L\cos(\theta) \right) \right) exp\left( -j\frac{4\pi}{\lambda} R \right) \tag{A.13}$$

# APPENDIX B

## CRLB DERIVATION

Let's write the received signal at an individual CW radar in the MCA based MIMO radar as

$$z(t) = s(t) + n(t) \tag{B.1}$$

where $s(t)$ is given as in (B.2) where $D = A_r(L_2+L_1)$, $A = \frac{4\pi}{\lambda}\frac{L_2+L_1}{2}\cos(\theta)\sin(2\pi f_r t + \frac{2\pi n}{N})$, $B = 2\pi f_c t - \frac{4\pi}{\lambda}(R+vt)$ and $N$ is the number of blades of the propeller.

$$\begin{aligned} s(t) = s_R(t) + js_I(t) &= \sum_{n=0}^{N-1}(D\cos(B+A)\,\mathrm{sinc}(A) + jD\sin(B+A)\,\mathrm{sinc}(A)) \\ &= D\sum_{n=0}^{N-1}\cos(B+A)\,\mathrm{sinc}(A) + jD\sum_{n=0}^{N-1}\sin(B+A)\,\mathrm{sinc}(A) \end{aligned} \tag{B.2}$$

In (B.2), $s_R(t) = D\sum_{n=0}^{N-1}\cos(B+A)\,\mathrm{sinc}(A)$ and $s_I(t) = D\sum_{n=0}^{N-1}\sin(B+A)\,\mathrm{sinc}(A)$.

The noise signal in (B.1) can be written in complex form as in (B.3).

$$n(t) = \mu(t) + j\nu(t) \tag{B.3}$$

The noise signal $n(t)$ is assumed to be zero mean, independent, Gaussian distributed. So the logarithm of the joint probability density function of $z(t)$ for $p^{th}$ transmit-receive pair can be written as in (B.4), where $M$ is the number of time samples, $T$

is the sampling period, $m$ is the time index, $\sigma$ is the standard deviation of noise. The vector parameter to be estimated is $\gamma = [x, y, f_r]$. Assume that there are $P$ transmit-receive pairs in the MCA based MIMO system. Then the logarithm of the joint probability density function of the whole MIMO radar system can be written as (B.5).

$$\log f(z_p, \gamma) = -M\log(\pi\sigma^2) - \frac{1}{\sigma^2}\sum_{m=1}^{M-1}[(s_R(mT) - \mu(mT))^2 + (s_I(mT) - \nu(mT))^2] \tag{B.4}$$

$$\begin{aligned}\log f(z, \gamma) = &-MP\log(\pi\sigma^2) - \\ &\frac{1}{\sigma^2}\sum_{p=1}^{P-1}\sum_{m=1}^{M-1}[(s_R^p(mT) - \mu^p(mT))^2 + (s_I^p(mT) - \nu^p(mT))^2]\end{aligned} \tag{B.5}$$

Considering (B.4), the $k^{th}$ row and $l_{th}$ column of the Fisher information matrix for the $p^{th}$ transmit-receive pair can be written as in (B.6) [55].

$$J_{k,l}^p(x, y) = \frac{2}{\sigma_p^2}\sum_{m=0}^{M-1}\left[\frac{\partial s_R^p(mT)}{\partial\gamma_k}\frac{\partial s_R^p(mT)}{\partial\gamma_l} + \frac{\partial s_I^p(mT)}{\partial\gamma_k}\frac{\partial s_I^p(mT)}{\partial\gamma_l}\right] \tag{B.6}$$

The $k^{th}$ row and $l_{th}$ column of the Fisher information matrix of the whole MIMO radar can be written as in (B.7).

$$J_{k,l}(x, y) = \sum_{p=0}^{P-1} J_{k,l}^p \tag{B.7}$$

Writing (B.6) and (B.7), the overall Fisher information matrix can be written explicitly as in (B.8).

$$J = \frac{2}{\sigma^2}\sum_{p=0}^{P-1}\sum_{m=0}^{M-1}\begin{bmatrix} J_{11} & J_{12} & J_{13} \\ J_{21} & J_{22} & J_{23} \\ J_{31} & J_{32} & J_{33}\end{bmatrix} \tag{B.8}$$

The matrix elements are defined as follows:

$$J_{11} = \left(\frac{\partial s_R^p(mT)}{\partial v}\frac{dv}{dx}\right)^2 + \left(\frac{\partial s_I^p(mT)}{\partial v}\frac{dv}{dx}\right)^2 \tag{B.9}$$

$$J_{12} = \frac{\partial s_R^p(mT)}{\partial v}\frac{dv}{dx}\frac{\partial s_R^p(mT)}{\partial v}\frac{dv}{dy} + \frac{\partial s_I^p(mT)}{\partial v}\frac{dv}{dx}\frac{\partial s_I^p(mT)}{\partial v}\frac{dv}{dy} \tag{B.10}$$

$$J_{13} = \frac{\partial s_R^p(mT)}{\partial v}\frac{dv}{dx}\frac{\partial s_R^p(mT)}{\partial f_r} + \frac{\partial s_I^p(mT)}{\partial v}\frac{dv}{dx}\frac{\partial s_I^p(mT)}{\partial f_r} \tag{B.11}$$

$$J_{21} = \frac{\partial s_R^p(mT)}{\partial v}\frac{dv}{dy}\frac{\partial s_R^p(mT)}{\partial v}\frac{dv}{dx} + \frac{\partial s_I^p(mT)}{\partial v}\frac{dv}{dy}\frac{\partial s_I^p(mT)}{\partial v}\frac{dv}{dx} \tag{B.12}$$

$$J_{22} = \left(\frac{\partial s_R^p(mT)}{\partial v}\frac{dv}{dy}\right)^2 + \left(\frac{\partial s_I^p(mT)}{\partial v}\frac{dv}{dy}\right)^2 \tag{B.13}$$

$$J_{23} = \frac{\partial s_R^p(mT)}{\partial v}\frac{dv}{dy}\frac{\partial s_R^p(mT)}{\partial f_r} + \frac{\partial s_I^p(mT)}{\partial v}\frac{dv}{dy}\frac{\partial s_I^p(mT)}{\partial f_r} \tag{B.14}$$

$$J_{31} = \frac{\partial s_R^p(mT)}{\partial f_r}\frac{\partial s_R^p(mT)}{\partial v}\frac{dv}{dx} + \frac{\partial s_I^p(mT)}{\partial f_r}\frac{\partial s_I^p(mT)}{\partial v}\frac{dv}{dx} \tag{B.15}$$

$$J_{32} = \frac{\partial s_R^p(mT)}{\partial f_r}\frac{\partial s_R^p(mT)}{\partial v}\frac{dv}{dy} + \frac{\partial s_I^p(mT)}{\partial f_r}\frac{\partial s_I^p(mT)}{\partial v}\frac{dv}{dy} \tag{B.16}$$

$$J_{33} = \left(\frac{\partial s_R^p(mT)}{\partial f_r}\right)^2 + \left(\frac{\partial s_I^p(mT)}{\partial f_r}\right)^2 \tag{B.17}$$

The terms in (B.8) are formulated in (B.18) - (B.19).

$$\frac{\partial s_R(t)}{\partial v} = \frac{2}{\lambda}\frac{\partial s_R(t)}{\partial f_d} = -D\sum_{n=0}^{N-1}\sin(B+A)\frac{dB}{dv}\,\mathrm{sinc}(A) \tag{B.18}$$

$$\frac{\partial s_I(t)}{\partial v} = \frac{2}{\lambda}\frac{\partial s_I(t)}{\partial f_d} = D\sum_{n=0}^{N-1}\cos(B+A)\frac{dB}{dv}\,\mathrm{sinc}(A) \tag{B.19}$$

where

$$\frac{dB}{dv} = -\frac{4\pi}{\lambda}t \tag{B.20}$$

In order to obtain the CRLB for localization, $v$ in $\gamma$ shall be expressed in terms of $x$ and $y$. So the derivative terms shall be written in $x$ and $y$. Through equations (B.21) - (B.26) required formulations are shown in order to express the Fisher information matrix in terms of $x$ and $y$, where $\dot{x}$ and $\dot{y}$ represents the $x$ and $y$ components of velocity vector $v$.

$$v = \dot{x}\frac{x - x_i}{cr_i} + \dot{y}\frac{y - y_i}{cr_i} \tag{B.21}$$

$$r_i = \left[(x - x_i)^2 + (y - y_i)^2\right]^{1/2} \tag{B.22}$$

$$\frac{dv}{dx} = \frac{1}{c(r_i)^2}\left(\dot{x}\left(r_i - (x - x_i)\frac{dr_i}{dx}\right) - \dot{y}\left((y - y_i)\frac{dr_i}{dx}\right)\right) \tag{B.23}$$

$$\frac{dv}{dy} = \frac{1}{c(r_i)^2}\left(\dot{y}\left(r_i - (y - y_i)\frac{dr_i}{dy}\right) - \dot{x}\left((x - x_i)\frac{dr_i}{dy}\right)\right) \tag{B.24}$$

$$\frac{dr_i}{dx} = \left[(x - x_i)^2 + (y - y_i)^2\right]^{-1/2}(x - x_i) \tag{B.25}$$

$$\frac{dr_i}{dy} = \left[(x - x_i)^2 + (y - y_i)^2\right]^{-1/2}(y - y_i) \tag{B.26}$$

The terms related with the $f_r$ are given in equations (B.27) and (B.28).

$$\frac{\partial s_R(t)}{\partial f_r} = D\sum_{n=0}^{N-1}\left(-\sin(B + A)\frac{dA}{df_r}\operatorname{sinc}(A) + \cos(B + A)\frac{\cos(A) - \operatorname{sinc}(A)}{A}\frac{dA}{df_r}\right) \tag{B.27}$$

$$\frac{\partial s_I(t)}{\partial f_r} = \\ D\sum_{n=0}^{N-1}\left(\cos(B+A)\frac{dA}{df_r}\,\mathrm{sinc}(A) + \sin(B+A)\frac{\cos(A)-\mathrm{sinc}(A)}{A}\frac{dA}{df_r}\right) \tag{B.28}$$

where

$$\frac{dA}{\partial f_r} = \frac{4\pi}{\lambda}\frac{L_2+L_1}{2}\cos(\theta)\cos(2\pi f_r t + \frac{2\pi n}{N})(2\pi t) \tag{B.29}$$

After obtaining the Fisher information matrix, the CRLB on the variance of the parameters $x$, $y$, $f_r$, and $f_d$ for MIMO radar solution presented in this work can be obtained as in (B.30) - (B.32). In these equations $var(\cdot)$ represents variance and $[\cdot]_{mn}$ represents $m^{th}$ row and $n^{th}$ column of the matrix inside the brackets.

$$\text{var}(x) \geq [J^{-1}]_{11} \tag{B.30}$$

$$\text{var}(y) \geq [J^{-1}]_{22} \tag{B.31}$$

$$\text{var}(f_r) \geq [J^{-1}]_{33} \tag{B.32}$$

# APPENDIX C

# MATLAB CODES

The simulations and analysis in this thesis are implemented in MATLAB 2021a environment. The MATLAB codes used in the thissis are presented in the following sections.

## C.1 RunScenario Function

This is the main function which runs the scenario.

```
clear all;
close all;
clc;

readFiles;

N = 1;  number of propellers
Lblade = 0.1;  blade length
fc = 5e9;  radar carrier frequency
fr = 100;  proller rotation frequency
theta = deg2rad(0);
c = 3e8;
lambda = c/fc;

snr = 100;
```

```
Fs = 44100;
signalDuration = 0.25;
signalVectorLength = floor(Fs signalDuration);
t = (0:(signalVectorLength 1))/Fs;

radarLocations = [151.186, 0];

[numberOfRadars, numDummy] = size(radarLocations);
droneLocation = [75, 0];75, 25
droneVelocity = [1, 0];

droneRadarVector = radarLocations   droneLocation;

droneRadarVectorNorm = normr(droneRadarVector);
   droneRadarVector ./ norm(droneRadarVector);

radialSpeed =  droneRadarVectorNorm   droneVelocity;

radarSignals = [];
meanFreq = zeros(1, numberOfRadars);
dopplerVector = zeros(numberOfRadars, 1);
for k = 1 : numberOfRadars
    singleSignal = generatePropellerSignal(N, Lblade, fc,
       radialSpeed(k), fr, theta, norm(droneRadarVector(k, :)
       ), t);
    singleSignal = singleSignal + generatePropellerSignal(N,
       Lblade, fc, radialSpeed(k)0.5, fr1.2, theta, norm(
       droneRadarVector(k, :)), t);
    singleSignal = singleSignal + generatePropellerSignal(N,
       Lblade, fc, radialSpeed(k)1.5, fr1.4, theta, norm(
       droneRadarVector(k, :)), t);

    radarSignals k  = singleSignal; awgn(singleSignal,snr,
       measured);
```

```
    yCrop = radarSignals k ;
    [alpha, f, C] = testCyclicFunction(yCrop, Fs);
    [alphaList, freqList, detimg] = tryCfarFunction(f, alpha,
        C);
    dopplerVector(k) = calcDopplerShift(100, alpha, alphaList
       , freqList, detimg);  first parameter is the estimated
        alpha
end

priTransform;
```

## C.2 TestCylic Function

This function calls the CSD function with appropriate parameters.

```
L = length(x);         signal length
Nw = 2048 2; 4;
Nv = fix(7/8Nw);      block overlap   fix(2/3Nw)
nfft = 2 Nw;
da = 1/L;              cyclic frequency resolution
a1 = 0;               first cyclic freq. bin to scan (i.e.
   cyclic freq. a1 da)
a2 = 1500;60;              last cyclic freq. bin to scan (i.e
   . cyclic freq. a2 da)
  Loop over cyclic frequencies
C = zeros(nfft,a2 a1+1);
S = zeros(nfft,a2 a1+1);
Q =  strcmp(which( chi2inv ) , )==1;   check if function
   chi2inv  is available
for k = a1:a2;
    if Q == 1
         CPS = CPSW(exp(j.phase(x)), exp(j.phase(x)),k/L,
           nfft,Nv,Nw, sym,.01);
```

```
        CPS = CPSW(x, x,k/L,nfft,Nv,Nw, sym ,.01);
    else
         Coh = SCohW(x,x,k/L,nfft,Nv,Nw, sym );
         CPS = CPSW(x,x,k/L,nfft,Nv,Nw, sym );
    end
    C(:,k a1+1) = CPS.S;
     S(:,k a1+1) = CPs.Syx;
    waitbar((k a1+1)/(a2 a1+1))
end
  Plot results
 Fs = 1;              sampling frequency in Hz
alpha = Fs (a1:a2) da;
 f = Fs CPS.f(1:nfft/2) 2;
f = Fs CPS.f;

figure
f = linspace( Fs/2, Fs/2, nfft);
imagesc(alpha,f,fftshift(abs(C(1:nfft,:))./(abs(max(max(C(1:
   nfft,:))))), 1));
colormap(jet),colorbar,axis xy,title( Cyclic Spectral Density
    ),
xlabel( cyclic frequency  alpha [Hz] ),ylabel( spectral
   frequency f [Hz] )
```

### C.3 TryCfarFunction Function

This function performs 2D CFAR.

```
function [alphaList, freqList, detimg, cCrop] =
   tryCfarFunction(f, alpha, C)

p = 1e 4;

middlePoint = floor(length(f)/2);
```

```
vecStart = 1; middlePoint 1 0 0 5 0;
vecEnd = length(f); middlePoint+10050;

cShifted = fftshift(C, 1);
cCrop = cShifted(vecStart:vecEnd, :);
freqList = f(vecStart:vecEnd);
alphaList = alpha(:);
[Msize, Nsize] = size(cCrop);


detector = phased.CFARDetector2D( TrainingBandSize,[3,3],
   ...
     ThresholdFactor , Auto , GuardBandSize,[0,0], ...
     ProbabilityFalseAlarm ,p, Method , CA ,
       ThresholdOutputPort ,true);

Ngc = detector.GuardBandSize(2);
Ngr = detector.GuardBandSize(1);
Ntc = detector.TrainingBandSize(2);
Ntr = detector.TrainingBandSize(1);
cutidx = [];
colstart = Ntc + Ngc + 1;
colend = Nsize   ( Ntc + Ngc);
rowstart = Ntr + Ngr + 1;
rowend = Msize   ( Ntr + Ngr);
for m = colstart:colend
    for n = rowstart:rowend
        cutidx = [cutidx,[n;m]];
    end
end
ncutcells = size(cutidx,2);


cutimage = zeros(Msize,Nsize);
```

```
for k = 1:ncutcells
    cutimage(cutidx(1,k),cutidx(2,k)) = 1;
end
 [dets,th] = detector(abs(cCrop).^2,cutidx);

detimg = zeros(length(freqList), length(alphaList));
cimg = zeros(length(freqList), length(alphaList));

for k = 1:ncutcells
    detimg(cutidx(1,k),cutidx(2,k)) = dets(k);
    cimg(cutidx(1,k),cutidx(2,k)) = cCrop(cutidx(1,k),cutidx
       (2,k));
end

figure;
imagesc(alphaList, freqList, (conv2(detimg, ones(5,2))/0.01))
colormap(flipud(gray));

axis tight; axis xy;

set(gcf, color , w );
set(gca, FontSize,24);
xlabel( Cyclic frequency  alpha [Hz] );
ylabel( Spectral frequency f [Hz] );
grid on;

xlim([0 1050]);
ylim([ 650 650]);
```

### C.4 CostRun Function

This function calculates the maximum allowable cost for a sensor.

```
clear all;
```

```
close all;
clc;

 costCommercial = 100000;    dollars blighter
costCommercial = 2000;    dollars simrad
rill = 5.2/360;
 rangeCommercialNoRcsEffect = 4600;  meters blighter
rangeCommercialNoRcsEffect = 400;  meters simrad
rcsDifference = 20;  dB difference between drone fusalage and
    propellers
rcsDiffFactor = (10(rcsDifference/10)).25;
rangeCommercial = rangeCommercialNoRcsEffect rcsDiffFactor;

r = 20:10:250;  meters

thetaValues = [deg2rad(360) deg2rad(90) deg2rad(30) deg2rad
   (10)];
lengththetaValues = length(thetaValues);
thetaSign =         x    o     ;

kValues = [3 5];
lengthkValues = length(kValues);
kColor = [ b   g ];

figure;
hold on;

for m = 1 : lengthkValues
    k = kValues(m);
    for n = 1 : lengththetaValues
        theta = thetaValues(n);

        if k == 5
             cUnit =
```

```
            cUnit = costCommercial sqrt(3) . 2 r . r/(7 (
               rangeCommercial rangeCommercial) (theta/2)
               rill);
        elseif k == 3
            cUnit = costCommercial sqrt(3) . r . r/(2 (
               rangeCommercial rangeCommercial) (theta/2)
               rill);
        end

        plot(r, cUnit, thetaSign n ,  color , kColor(m),
           linewidth , 2);

    end
end


legend ( alpha=360o, k=3 ,  alpha=90o, k=3 ,  alpha=30o,
    k=3 ,  alpha=10o, k=3 , ...
      alpha=360o, k=5 ,  alpha=90o, k=5 ,  alpha=30o, k
       =5 ,  alpha=10o, k=5 );
xlabel ( Range of sensor (m) );
ylabel ( Cost upper limit of sensor ( ) );
grid on;
```

### C.5 FindTargetLocation Function

This function finds target location using doppler-only localization algorithm.

```
function [costMatrix, xVector, yVector] = findTargetLocation(
   dopplerVector, radarLocations, ...
                                          minx, maxx, miny,
                                              maxy, stepx,
                                             stepy)
```

```
xVector = minx:stepx:maxx;
yVector = miny:stepy:maxy;

c = 3e8;
eps = 0.001;

costMatrix = zeros(length(yVector), length(xVector));

radarsXCoordinates = radarLocations(:, 1);
radarsYCoordinates = radarLocations(:, 2);

for yIndex = 1 : length(yVector)
    yPos = yVector(yIndex);
    for xIndex = 1 : length(xVector)
        xPos = xVector(xIndex);
        r = ((xPos   radarsXCoordinates).2 + (yPos
           radarsYCoordinates).2).0.5 + eps;
        ki = (xPos   radarsXCoordinates)./r/c;
        mi = (yPos   radarsYCoordinates)./r/c;

        aMatrix = [ki mi ones(length(ki), 1)];
        g = inv(transpose(aMatrix) aMatrix) transpose(aMatrix
           ) dopplerVector;
        jTerm = (norm(aMatrix g dopplerVector)) 2;
        costMatrix(yIndex, xIndex) = jTerm;
    end
end
```

### C.6 GeneratePropellerSignal Function

This function generates propeller signal.

```
function s = generatePropellerSignal(N, L, fc, v, fr, theta,
   R, t)
```

```
c = 3e8;

Ar = 1;
lambda = c/fc;

s = zeros(1, length(t));

for k = 0 : N  1
    expTerm =    4 . pi./lambda . (R + v . t + ...
                L./2 . cos(theta) . sin(2 . pi . fr . t + 2 . pi . k
                   ./N));
    ampMultTerm = sinc(4 . pi./lambda  .  L./2  .  cos(theta)  .
        sin(2 . pi . fr . t + 2 . pi . k./N));
    sumTerm = exp(j . expTerm) . ampMultTerm;
    s = s + sumTerm;
end
```

### C.7 CalcMonostaticCRLB Function

This function calculates monostatic radar CRLB.

```
clear all;
 close all;
clc;
load intersectionPositions;

c = 3e8;
f = 10e9;
lambda = c/f;

M = 5; 64;
T = 16;
B = 5e6;
```

```
numSamples = B20.030;128;

d = lambda/2;
dm = ([0:M1] (M1)).d;
D = M d;
bw = 0.886lambda/D;
 dm = [0:M1].lambda/2;
sumdm = d d/12M (M M1);

snrdB = 20:2:40;
 snrdB = snrdB   31.76;
snr = 10.(snrdB/10);

snrLength = length(snr);
 crlbMonoAngle = zeros(1, snrLength);
 crlbMonoRange = zeros(1, snrLength);

crlbMonoX = zeros(1, snrLength);
crlbMonoY = zeros(1, snrLength);

  xmin = 0;
  xmax = 600;
  ymin = 0;
  ymax = 600;

  xPoints = linspace(xmin, xmax, 30);
  yPoints = linspace(ymin, ymax, 1000);
xPoints = intersectionPositions(:, 1);
yPoints = intersectionPositions(:, 2);

  radarLocX = 300;
  radarLocY = 300;

sensorx = [0; 75.5929; 151.186; 37.7964; 113.389];
```

```
sensory = [0; 0; 0; 65.4654; 65.4654];

radarLocX = sensorx(5);
radarLocY = sensory(5);

crlbMatrixX = zeros(length(xPoints), length(yPoints),
   snrLength);
crlbMatrixY = zeros(length(xPoints), length(yPoints),
   snrLength);

for xCount = 1 : length(xPoints)
    xLoc = xPoints(xCount);
    for yCount = 1 : length(yPoints)
        yLoc = yPoints(yCount);
        [th, r] = cart2pol(xLoc   radarLocX, yLoc   radarLocY
           );
         G = [sin(th) (r+eps) cos(th); cos(th)  (r+eps) sin(
           th)];
        G = [cos(th)  (r+eps) sin(th); sin(th) (r+eps) cos(th
           )];
        for k = 1 : snrLength
            crlbMonoAngle = bw/1.61/sqrt(2.snr(k).M.
               numSamples);
            crlbMonoRange = sqrt(3c c/8/pi/pi/B/B/(snr(k).M
               .numSamples));

            Crth = [crlbMonoRange2  0; 0 crlbMonoAngle2];

            Cxy = G Crth transpose(G);

              crlbMonoX(k) = Cxy(1, 1) + crlbMonoX(k);
              crlbMonoY(k) = Cxy(2, 2) + crlbMonoY(k);

            crlbMatrixX(xCount, yCount, k) = Cxy(1, 1);
```

```
            crlbMatrixY(xCount, yCount, k) = Cxy(2, 2);
        end
    end
end

  crlbMonoX(k) = crlbMonoX(k)./(length(xPoints) length(
   yPoints));
  crlbMonoY(k) = crlbMonoY(k)./(length(xPoints) length(
   yPoints));

for k = 1 : snrLength
    crlbMonoX(k) = sum(sum(crlbMatrixX(:,:,k)))/(length(
       xPoints) length(yPoints));
    crlbMonoY(k) = sum(sum(crlbMatrixY(:,:,k)))/(length(
       xPoints) length(yPoints));
end


 figure;
 hold on;
 semilogy(snrdB, crlbMonoAngle);
 semilogy(snrdB+51.76, crlbMonoX + crlbMonoY,  color ,  c );
semilogy(snrdB, crlbMonoX + crlbMonoY,  color ,  c );
```

## C.8 PRITransform Function

This function calculates PRI transform.

```
resAlpha = alpha(2)   alpha(1);
projectionData = sum(detimg, 1);
pkslocs = find(projectionData5000);


tauMin = 0;  min cyclic frequency
```

```
tauMax = 800;  max cyclic frequency

[val,idxMin]=min(abs(alphaList tauMin));
[val,idxMax]=min(abs(alphaList tauMax));

numberOfKs = idxMax   idxMin + 1;

D = zeros(1, numberOfKs);

alphaPeaks = resAlpha . pkslocs;

 for k = 1 : numberOfKs

    for n = 2 : length(alphaPeaks)
        for m = n   1 :  1 : 1
            tau = alphaPeaks(n)   alphaPeaks(m);
            if (tau   tauMin)
                ; continue;
            elseif (tau   tauMax)
                ; continue;
            else
                [val,idx]=min(abs(alphaList tau));
                D(idx) = D(idx) + exp(j 2 pi alphaPeaks(n)/
                   tau);
            end
        end
    end
 end

figure;
plot(resAlpha . [0 : length(D) 1], abs(D),  linewidth , 2);
grid on;

set(gcf, color , w ) ;
```

```
set(gca, FontSize,24);
xlabel( Cyclic frequency  alpha [Hz] );
```

### C.9 HistogramDetector Function

This function calculates histogram deinterleaving.

```
histData = sum(detimg, 1);
k = 26;
harmonicRegion = detimg(:, 267);

freqRes = Fs/nfft;
alphaSelected = Fs k da;
freqIndexSelected = floor(alphaSelected/freqRes);


[pks, locs] = findpeaks(harmonicRegion,freqList);
peakInterval = diff(locs);
hist(peakInterval, 1024)
grid on
```

### C.10 TestCyclicFunction Function

This function runs CSD analysis.

```
function [alpha, f, C] = testCyclicFunction(yCrop, Fs)

x = yCrop;

L = length(x);         signal length
 Nw = 20482/4;             window length  20482
Nw = 20484; 4;
Nv = fix(1/4Nw);      block overlap   fix(2/3Nw)
 nfft = 2 Nw 4 8;          FFT length 2 Nw
```

```
nfft =  2 Nw;
da = 1/L;              cyclic frequency resolution
a1 = 0;               first cyclic freq. bin to scan (i.e.
   cyclic freq. a1 da)
a2 = 500;6008;60;              last cyclic freq. bin to
   scan (i.e. cyclic freq. a2 da)
  Loop over cyclic frequencies
C = zeros(nfft,a2 a1+1);
S = zeros(nfft,a2 a1+1);
Q =  strcmp(which( chi2inv ) ,  ) ==1;   check if function
   chi2inv  is available
for k = a1:a2;
    if Q == 1
         CPS = CPSW(exp(j. phase(x)), exp(j. phase(x)),k/L,
           nfft,Nv,Nw, sym ,.01);
        CPS = CPS W(x, x,k/L,nfft,Nv,Nw, sym ,.01);
    else
         Coh = SCohW(x,x,k/L,nfft,Nv,Nw, sym );
         CPS = CPSW(x,x,k/L,nfft,Nv,Nw, sym );
    end
    C(:,k a1+1) = CPS.S;
     S(:,k a1+1) = CPs.Syx;
    waitbar((k a1+1)/(a2 a1+1))
end
  Plot results
 Fs = 1;               sampling frequency in Hz
alpha = Fs (a1:a2) da;
 f = Fs CPS.f(1:nfft/2) 2;
 f = Fs CPS.f;

 f = linspace( Fs/2, Fs/2, nfft);
df = Fs/nfft;
if rem(nfft, 2)
    halfres = df/2;
```

```
    f =  Fs/2+half res:df:Fs/2 half res;
else
    f =  Fs/2:df:Fs/2 df;
end

figure
imagesc(alpha,f,fftshift(abs(C(1:nfft,:))./(abs(max(max(C(1:
   nfft,:))))), 1));
set(gca,  YDir , normal )
set(gcf, color , w );
set(gca, FontSize,24);
xlabel( Cyclic frequency  alpha [Hz] );
ylabel( Spectral frequency f [Hz] );

xlim([0 1050]);
ylim([ 650  650]);
```

### C.11 CalcDopplerShift Function

This function calculates doppler shift from CSD.

```
function dopplerShift = calcDopplerShift(alphaVal, alpha,
   alphaList, freqList, detimg)

alphaIndeces = [];

for k = 1 : floor(max(alpha)/alphaVal)
    [val, alphaIndeces(k)]=(min(abs(alphaList k alphaVal)));
end

freqOffsets =  ;
freqSum = 0;
freqCount = 0;
```

```
for k = 1 : length(alphaIndeces)
    freqValues = freqList(find(detimg(:, alphaIndeces(k))));
    isAlphaEven =  rem(round(alphaList(alphaIndeces(k))/
       alphaVal), 2);

    if isAlphaEven
        freqOffsets k  = freqValues   round(freqValues./(
           alphaVal)) alphaVal;
    else
        freqOffsets k  = freqValues   round odd(freqValues./(
           alphaVal/2)) alphaVal/2;
    end

    freqSum = freqSum + sum(freqOffsets k );
    freqCount = freqCount + length(freqOffsets k );
end

dopplerShift = freqSum/freqCount;
```

### C.12 CPSW Function

Welch's estimate of the (Cross) Cyclic Power Spectrum. The function is implemented by J. Antoni.

```
function  Spec = CPS  W(y,x,alpha,nfft,Noverlap,Window,opt,P)

if length(Window) == 1
    Window = hanning(Window);
end
Window = Window(:);
n = length(x);            Number of data points
nwind = length(Window);   length of window
  check inputs
 if (alpha 1  alpha 0),error( alpha must be in [0,1] !!),end
```

```
if nwind  = Noverlap,error( Window length must be   Noverlap
    );end
if nfft   nwind,error( Window length must be  = nfft );end
if nargin   7    (P =1    P =0),error( P must be in ]0,1[
   !! ),end
y = y(:);
x = x(:);
K = fix((n Noverlap)/(nwind Noverlap));   Number of windows
  compute CPS
index = 1:nwind;
f = (0:nfft 1)/nfft;

t = (0:n 1) ;
CPS = 0;
if strcmp(opt, sym )  == 1
    y = y . exp( 1i pi alpha t);
    x = x . exp(1i pi alpha t);
else
    x = x . exp(2i pi alpha t);
end
for i=1:K
     xw = Window . x(index); xw = xw   mean(xw);
     yw = Window . y(index); yw = yw   mean(yw);
    xw = Window . x(index);
    yw = Window . y(index);
    Yw1 = fft(yw,nfft);       Yw(f+a/2) or Yw(f)
    Xw2 = fft(xw,nfft);       Xw(f a/2) or Xw(f a)
    CPS = Yw1 . conj(Xw2) + CPS;
    index = index + (nwind   Noverlap);
end
  normalize
KMU = K norm(Window) 2;   Normalizing scale factor ==
   asymptotically unbiased
CPS = CPS/KMU;
```

```
  variance reduction factor
Window = Window(:)/norm(Window);
Delta = nwind   Noverlap;
R2w = xcorr(Window);
k = nwind+Delta:Delta:min(2 nwind 1,nwind+Delta (K 1));
if length(k)  1
    Var Reduc = R2w(nwind) 2/K + 2/K (1 (1:length(k))/K) (R2w
       (k) . 2);
else
    Var Reduc = R2w(nwind) 2/K;
end
  confiance interval
if nargin   7
    v = 2/Var Reduc;
    alpha = 1   P;
    if alpha == 0         Sa   Chi2
        temp = 1./chi2inv([1 alpha/2 alpha/2],round(v));
        CI = v CPS temp;
    else                       Sa   Normal
        Sy = CPS W(y,y,0,nfft,Noverlap,Window,opt);
        Sx = CPS W(x,x,0,nfft,Noverlap,Window,opt);
        Var Sa = Sy.S . Sx.S/v;
        temp = sqrt(2) erfinv(2 P 1);
        CI = CPS[1  1] + temp sqrt(Var Sa(:)) [1  1];
    end
end
  set up output parameters
if nargout == 0
    figure,newplot;
    plot(f,10 log10(abs(CPS))),grid on
    xlabel( [Hz] ),title( Spectral Correlation Density (dB) )
else
    Spec.S = CPS;
    Spec.f = f;
```

```
    Spec.K = K;
    Spec.Var Reduc = Var Reduc;
    if nargin   7
        Spec.CI = CI;
    end
end
```

### C.13 MIMOCRLB Function

This function calculates MIMO CRLB.

```
clear all;

clc;
load intersectionPositions;

c = 3e8;
f = 10e9;
lambda = c/f;

 drone parameters
 position parameters
x = 75;
y = 25;
xdot = 10;
ydot = 0;
 other drone parameters
L2 = 0.1;
L1 = 0;
fr = 100;
K2 =  4 pi/lambda (L2 L1)/2;
N = 5;  number of radars
R = 50;
P = 2;  number of blades
```

```
 sensor positions
sensorx = [0; 75.5929; 151.186; 37.7964; 113.389];
sensory = [0; 0; 0; 65.4654; 65.4654];

 distance between each sensor and drone
r = sqrt((sensorx x).2 + (sensory y).2);

 signal parameters
Fs = 44100;
Ts = 1/Fs;
signalDuration = 0.030;
signalVectorLength = floor(Fs signalDuration);
t = (0:(signalVectorLength 1))/Fs;
  t = 0:0.001:0.1;
timeLength = length(t);

singleSignal = generatePropellerSignal(N, L2, f, 0, fr, 0, R,
    t);

 signalPower = sum(abs(singleSignal).2)/Fs;
signalPower = sum((abs(singleSignal).2) . Ts)/signalDuration;

snrValues = 40:2:20;
 snrValues = snrValues   7.78;
crlbValues = zeros(1, length(snrValues));
crlbValuesTotal = zeros(1, length(snrValues));

crlbValuesfr = zeros(1, length(snrValues));
crlbValuesfd = zeros(1, length(snrValues));
crlbValuesTotalfr = zeros(1, length(snrValues));
crlbValuesTotalfd = zeros(1, length(snrValues));

[numPositions, tempVar] = size(intersectionPositions);
```

```
for dronePosCount = 1 : numPositions
    x = intersectionPositions(dronePosCount, 1);
    y = intersectionPositions(dronePosCount, 2);
    for snrCount = 1 : length(snrValues)
    snrValue = snrValues(snrCount);
    sigma = sqrt(signalPower/(10(snrValue/10)));
     J = zeros(4, 4);
    J = zeros(3, 3);
    for n = 1 : N  number of radars
        velocityVector = [xdot ydot];
        relativePositionVector = [sensorx(n) x; sensory(n) y
           ];
        radialVelocity = (velocityVector
           relativePositionVector)/norm(
           relativePositionVector);

        srfr = zeros(1, timeLength);
        srfr2 = zeros(1, timeLength);
        srfrv = zeros(1, timeLength);
        srv = zeros(1, timeLength);
        srv2 = zeros(1, timeLength);
        sifr = zeros(1, timeLength);
        sifr2 = zeros(1, timeLength);
        sifrv = zeros(1, timeLength);
        siv = zeros(1, timeLength);
        siv2 = zeros(1, timeLength);

        for p = 0 : P   1
            A = K2 sin(2 pi fr . t+2 pi p/P);
            ADot = K2 cos(2 pi fr . t+2 pi p/P) 2 pi . t;

            U = (cos(A) sinc(A))./(A+eps) . ADot;
```

```
    B =  2 pi  f . t    4 pi/lambda ( norm(
       relativePositionVector)+radialVelocity . t);
    BDot =   4 pi/lambda . t;

     calc srDotFr
    srDotfrTerm =   sin(B+A) . ADot . sinc(A)  + cos(B+A)
       . U;
    srfr = srfr + srDotfrTerm;


     calc srDotv
    srDotvTerm =   sin(B+A) . BDot . sinc(A);
    srv = srv + srDotvTerm;

    srfd = srv 2 / lambda;


     calc siDotfr
    siDotfrTerm = cos(B+A) . ADot . sinc(A)  + sin(B+A)
       . U;
    sifr = sifr +  ( siDotfrTerm);


    siDotvTerm = cos(B+A) . BDot . sinc(A);
    siv = siv +  ( siDotvTerm);

    sifd = siv 2 / lambda;
end

ri = norm(relativePositionVector);
xi = sensorx(n);
yi = sensory(n);

rix = ((x xi) 2  + (y yi) 2 ) ( 1 / 2 )    (x xi);
```

```
riy = ((x xi) 2 + (y yi) 2) ( 1/2)    (y yi);

vx = f (xdot   xdot (x xi) c rix)/(c ri) 2    f (ydot
    (y yi) c rix)/(c ri) 2;
vy = f (ydot   ydot (y yi) c riy)/(c ri) 2    f (xdot
    (x xi) c riy)/(c ri) 2;
vxdot = f (x   xi)/c/ri;
vydot = f (y   yi)/c/ri;

vx2 = 0;
vy2 = 0;
vxdot2 = 0;
vydot2 = 0;

sx = srv   vx + j   siv   vx;
sy = srv   vy + j   siv   vy;
sxdot = srv   vxdot + j   siv   vxdot;
sydot = srv   vydot + j   siv   vydot;

sfr = srfr + j   sifr;

sv = srv + j   siv;
sfd = srfd + j   sifd;

j11 = sum(real(sx) . real(sx) + imag(sx) . imag(sx));
j12 = sum(real(sx) . real(sy) + imag(sx) . imag(sy));
j13 = sum(real(sx) . real(sfr) + imag(sx) . imag(sfr));
j14 = sum(real(sx) . real(sfd) + imag(sx) . imag(sfd));

j21 = sum(real(sx) . real(sy) + imag(sx) . imag(sy));
j22 = sum(real(sy) . real(sy) + imag(sy) . imag(sy));
j23 = sum(real(sy) . real(sfr) + imag(sy) . imag(sfr));
j24 = sum(real(sy) . real(sfd) + imag(sy) . imag(sfd));
```

```
        j31 = sum(real(sx) . real(sfr) + imag(sx) . imag(sfr));
        j32 = sum(real(sy) . real(sfr) + imag(sy) . imag(sfr));
        j33 = sum(real(sfr) . real(sfr) + imag(sfr) . imag(sfr)
           );
        j34 = sum(real(sfr) . real(sfd) + imag(sfr) . imag(sfd)
           );

        j41 = sum(real(sx) . real(sfd) + imag(sx) . imag(sfd));
        j42 = sum(real(sy) . real(sfd) + imag(sy) . imag(sfd));
        j43 = sum(real(sfr) . real(sfd) + imag(sfr) . imag(sfd)
           );
        j44 = sum(real(sfd) . real(sfd) + imag(sfd) . imag(sfd)
           );



             J = J + [j11 j12 j13;
                      j21 j22 j23;
                      j31 j32 j33];



        end
        J = (2/sigma 2 )  J;

        crb = inv(J);

        crlbValues(snrCount) = (crb(1, 1)) + (crb(2, 2));
           only location
    end
    crlbValuesTotal = crlbValuesTotal + crlbValues;
end

semilogy(snrValues+20, crlbValuesTotal/numPositions,  b   );
   hold on;
```

## CURRICULUM VITAE

Surname, Name: Yazıcı, Ayhan

### EDUCATION

| Degree | Institution | Year of Graduation |
|---|---|---|
| M.Sc. | METU Electrical and Electronics Engineering | 2005 |
| B.Sc. | Hacettepe Uni. Electrical and Electronics Engineering | 2002 |
| High School | Anıttepe Lisesi | 1998 |

### WORK EXPERIENCE

| Year | Company | Title |
|---|---|---|
| 2011-Present | ASELSAN | Senior Lead Engineer |
| 2002-2010 | TÜBİTAK | Expert Research Scientist |

**FOREIGN LANGUAGES** English

### PUBLICATIONS

1. A. Yazıcı and B. Baykal, "Detection and Localization of Drones in MIMO CW Radar," Submitted to IEEE Transactions on Aerospace and Electronic Systems.

2. A. Yazıcı, A. Ç. Hamurcu and B. Baykal, "The detection performance of Neyman-Pearson detector for MIMO radar in K-distributed sea clutter," 2010 IEEE 18th Signal Processing and Communications Applications Conference, 2010, pp.

165-168, doi: 10.1109/SIU.2010.5649973.

3. A. Yazıcı and B. Baykal, "Effect of quantization on MIMO radar performance," 2010 IEEE 18th Signal Processing and Communications Applications Conference, 2010, pp. 546-549, doi: 10.1109/SIU.2010.5650205.

4. A. Yazıcı, A. Ç. Hamurcu and B. Baykal, "A practical point of view: Performance of Neyman-Pearson detector for MIMO radar in K-distributed clutter," 2009 IEEE/SP 15th Workshop on Statistical Signal Processing, 2009, pp. 273-276, doi: 10.1109/SSP.2009.5278585.

5. A. Yazıcı and B. Baykal, "Block Transmissions on Orthogonal Carriers," IEEE Vehicular Technology Conference, 2006, pp. 1-5, doi: 10.1109/VTCF.2006.183.

**PATENTS**

1. "Distributed Doppler Shift Based Drone Detection." Patent Application (2021).